DISSERTATION

INVESTIGATION OF THE DYNAMICS OF TROPICAL CYCLONE PRECIPITATION STRUCTURE USING RADAR OBSERVATIONS AND NUMERICAL MODELING

Submitted by
Ting-Yu Cha
Department of Atmospheric Science

In partial fulfillment of the requirements
For the Degree of Doctor of Philosophy
Colorado State University
Fort Collins, Colorado
Spring 2023

Doctoral Committee:

Advisor: Michael M. Bell

Kristen L. Rasmussen
Russ S. Schumacher
Wen-Chau Lee
Steven C. Reising

ABSTRACT

INVESTIGATION OF THE DYNAMICS OF TROPICAL CYCLONE PRECIPITATION STRUCTURE USING RADAR OBSERVATIONS AND NUMERICAL MODELING

Precipitation from tropical cyclones (TCs) produces significant damage and causes fatalities worldwide. Forecast skill of the structure of precipitation in a TC remains challenging, due in part to limited fundamental understanding of the underlying complex dynamics and limitations in our observational capability. This dissertation seeks to improve our understanding of the underlying dynamics of TC precipitation structure by using and improving radar retrieval techniques and numerical modeling.

In Part 1, the vortex dynamics of TC polygonal eyewall structure during rapid intensification (RI) of Hurricane Michael (2018) are examined from ground-based single-Doppler radar analysis. Although the organization of polygonal precipitation asymmetries has been theorized to be related to vortex Rossby wave (VRW) dynamics, prior studies have had observational limitations that prevent a detailed description of the phenomena. Here, we present the first observational evidence of the evolving wind field of a polygonal eyewall during RI to Category 5 intensity by deducing the axisymmetric and asymmetric winds at 5-min intervals. Novel single Doppler radar retrievals show that both tangential wind and reflectivity asymmetries rotate at speeds that are consistent with linear VRW theory. Dual-Doppler winds from airborne radar provide further evidence of the vortex structure that supports growth of asymmetries during RI.

In Part 2, the relationship between VRWs and the polygonal precipitation structure is further explored through a simple modeling framework. A two-layer model consisting of a shallow water fluid on top of a slab boundary layer is used to understand the dynamical relationship. The model maintains an approximate gradient wind balance in the free atmospheric layer and parameterizes the diabatic heating produced by convection from the vertical motion out of the boundary layer. The two-layer model provides insight into the essential dynamics of Hurricane Michael's intensification and precipitation structure observed by radar in Part 1. The results show that the convective maxima located at the vertices of an elliptical vortex are due to boundary layer processes and not the free atmospheric convergence. The simulations further show that continuous intensification of the vortex can happen in the presence of elliptical asymmetries and even after the potential vorticity ring breakdown when the diabatic heating is continuously maintained by boundary layer processes.

When TCs approach land they can produce voluminous rainfall totals, especially when interacting with complex terrain. Doppler radar can provide the capability to monitor extreme rainfall events over land, but our understanding of airflow modulated by orographic interactions remains limited. In Part 3, a new Doppler radar technique is developed to retrieve three-dimensional wind fields in precipitation over complex terrain. New boundary conditions are implemented in a variational multi-Doppler radar technique to represent the topographic forcing and surface impermeability. A series of observing simulation sensitivity experiments using a full-physics model and radar emulator simulating rainfall from Typhoon Chanthu (2021) over Taiwan are conducted to evaluate the retrieval accuracy and parameter settings. Analysis from real radar observations from Chanthu demonstrates that the improved retrieval technique can advance scientific analyses for the underlying dynamics of orographic precipitation using radar observations.

ACKNOWLEDGEMENTS

I deeply thank my advisor, Dr. Michael M. Bell for the mentorship over the past 6 years, the encouragement when I felt defeated, and full support for providing me with multiple great opportunities to attend conferences, collaborate with NCAR scientists, teach and mentor students, learn multiple different skills, and even take a leadership role in the PRECIP field campaign in the graduate journey. I would not have been possible to grow as much without all the different opportunities and guidance from him, and close observations of his devotion to science, his kindness to people, and his extraordinary leadership and mentorship to a big group of scientists and students.

I sincerely appreciate Dr. Wen-Chau Lee for kick-starting my adventure to the radar world. I would have never embarked on this amazing journey without participating the 2015 PECAN field campaign, which is the most eye-opening experience and the turning point of my life. I am truly grateful for the guidance, support, and encouragement received from him as a mentor and as a family. I thank him for also serving on my Ph.D. committee.

I am very thankful for Dr. Kristen L. Rasmussen and Dr. Russ S. Schumacher for serving on my Ph.D. committee, providing feedback and support on research, and introducing different opportunities. I would like to thank my outside committee member, Dr. Steven C. Reising, for being my committee member over the past 6 years.

I am greatly thankful for the Bell Research Group, the past and present members including Jon, Ellie, Naufal, Ben, Chelsea, Jhordanne, Dandan, Jen, Ya-Chien, Phil, Alex, Rung, Ali, Brenda, Tyler, and Angelie. I would have never asked for a better group to work with, and I am truly grateful for the friendship and support in life, research, and English. I would also like to thank Bruno Melli for helping me debug coding issues and shaping my coding skills early on. I also thank all the faculty, staff, and students in the department for all the efforts to provide a wonderful environment to engage in science and build community.

I would also like to thank Mike Dixon, Brenda Javorik, Wen-Chau Lee for collaborating and working on the LROSE project together. I have learned not only from their creative thinking and scientific thoughts, but also tremendously from their work ethics.

I would not have been here without the unconditional love and full support from my parents. They have not only provided all the support that allows me to dream and to fly carefree, but also served as a safety nest when I feel broken and fall apart. The daily phone call across thousands of miles supported me crawling over my darkest days. I also thank my sister for all the support. They always have deep faith in me even when my soul was shattered.

I am very grateful for having amazing groups of friends in Fort Collins throughout the years, and love and spiritual support from friends in Taiwan and across the world. I especially thank Kai-Chih and Ting-Chang all the encouragement and support throughout the years. I thank Heidi for taking very good care of me during my last sprint of wrapping up PhD. I would never have had the courage to step outside of my comfort zone to chase the dream, and to be who I am today without all of the above.

This research is supported by the National Science Foundation (NSF) AGS-1701225, AGS-1854559 and OAC-1661663, Office of Naval Research awards N000141613033 and N000142012069, and Taiwan Ministry of Education graduate fellowship.

TABLE OF CONTENTS

LIST OF FIGURES

Chapter 1

Introduction

1.1 Motivation

The tropical cyclone (TC) is one of the most high impact weather to produce extreme rainfall that continues to threaten coastal areas with expanding communities and growing development. The IPCC 6th assessment report indicates that TCs are projected to attain higher intensities and precipitation rates, produce greater amounts of rainfall, and contribute to enhanced storm-surge inundation under global warming (IPCC 2021). Typhoon Morakot (2009) produced up to 2,965 mm of precipitation in a 4 days over Taiwan, causing one of the worst flooding disasters to this date (Wu 2013). While TC rainfall accumulation is determined by the track and motion to first order, multi-scale interactions, the underlying mesoscale processes, and interactions with terrain can affect the intensity and duration of TC-associated precipitation events. Forecast skill of the structure of precipitation in a TC remains challenging, due in part to limited fundamental understanding of the underlying complex dynamics and limitations in our observational capability. A continuous effort for accurate quantitative precipitation forecasts (QPF) is needed to improve this worldwide societal problem.

While great progress has been made towards improving TC track forecasts, the marginal TC intensity forecast improvement is partly due to complex inner core processes that are less predictable and more difficult to observe in detail (Hendricks et al. 2010). An improved fundamental understanding of the mechanisms and complex interaction between physical processes that impact TC intensity change and precipitation structure is required. However, most observations are unable to capture inner-core processes because (1) TCs are often distant from continuous observational platforms, (2) airborne reconnaissance and research missions are rare events in most of the countries, and (3) the spatial and temporal aliasing of observations make it difficult to assess the interactions between different physical mechanisms (Cha and Bell 2021).

When TCs approach land they can produce voluminous rainfall totals, especially when interacting with complex terrain. Accurate QPF becomes even more challenging when interactions with terrain that can change the TC track, precipitation duration and intensity, the mesoscale processes, and more (Bell 2017). While Doppler radar and in-situ instruments can provide the real-time capability to monitor rainfall events over land, our understanding of airflow modulated by orographic interactions remains limited. Most of the multi-Doppler radar retrieval techniques are unable to reconstruct the three-dimensional flow close to the vicinity of the terrain because the orographic forcing and the surface impermeability are not incorporated to the techniques for the lower boundary conditions. An improved Doppler radar technique is required to retrieve three-dimensional wind fields in precipitation over complex terrain and is a critical scientific tool in order to advance our understanding of terrain interactions and orographic dynamics.

This dissertation seeks to improve our understanding of the underlying dynamics of TC precipitation structure by using and improving radar retrieval techniques and numerical modeling. Section 1.2 will discuss TC polygonal eyewall precipitation asymmetries and dynamics, section 1.3 will review TC orographic rainfall and radar retrieval techniques, and section 1.4 will provide the research objectives and outline.

1.2 Polygonal eyewall precipitation asymmetries to kinematic asymmetries

Lewis and Hawkins (1982) was one of the first studies to document rotating polygonal asymmetries in hurricanes by weather surveillance radar (WSR-57) reflectivity observations. They observed the asymmetries through reflectivity, and noted “In accumulating such data from land-based radar film, one of us (Lewis) observed that frequently the hurricane eyes were neither circular nor elliptical, but appeared to be hexagonal, square, or triangular.” They further hypothesized that polygonal precipitation asymmetries are organized by the underlying dynamics through horizontally propagating internal gravity waves.

Although their hypothesis for precipitation asymmetries was deficient, their close examination of radar films has shed light on many of the following research to study the dynamical relationship to the observed convective elements (Fig. 1.1).

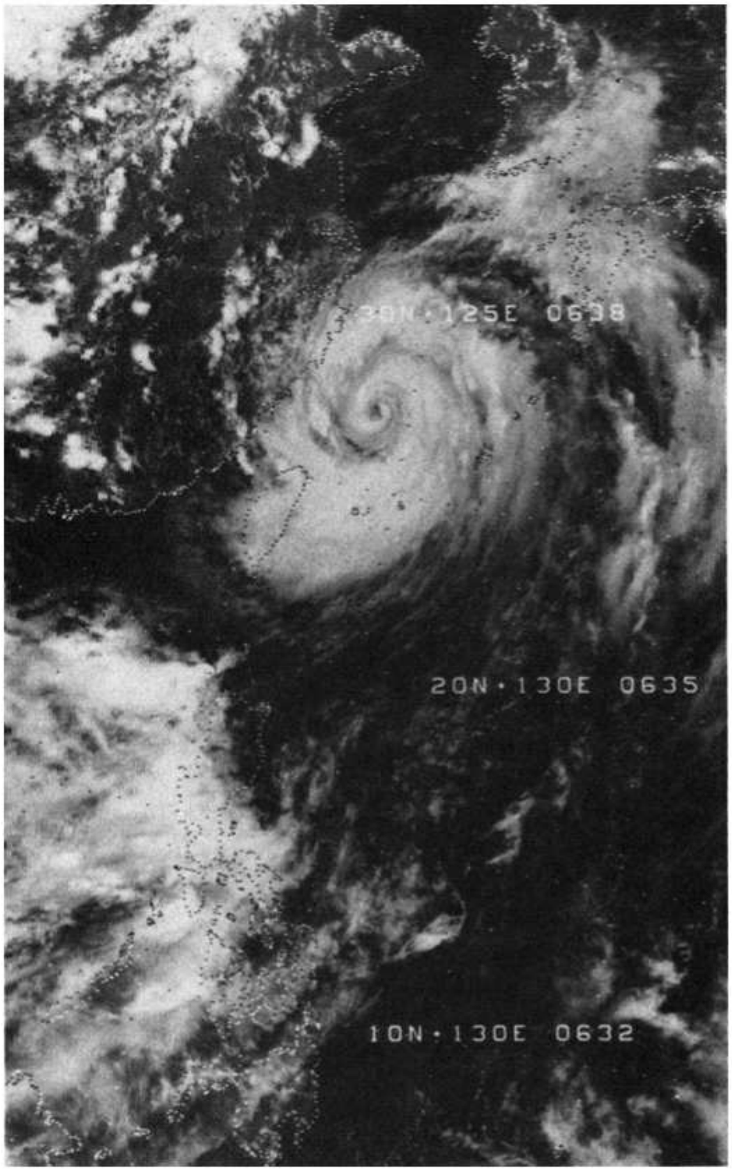

Figure 1.1: Satellite image of Typhoon Irving on 15 August 1979 derived from Fig. 7 in Lewis and Hawkins (1982).

Numerous intensifying TCs with polygonal eyewall structures were captured by radar and satellite imagery and the underlying dynamics were further examined through numerical modeling and observations (Kossin and Schubert 2004; Hendricks et al. 2012; Guimond et al. 2016; Cha et al. 2020). By testing out different hypotheses and carrying out tremendous experiments through simple model approaches and numerical simulations (Guinn and Schubert 1993; Montgomery and Shapiro 1995; Montgomery and Kallenbach 1997; Kuo et al. 1999; Rozoff et al. 2009; Schubert et al. 1999; Hendricks et al. 2014; Kuo et al. 2016), the scientific community is likely to reach to a consensus that the elliptical and polygonal eyewall asymmetries are the result of asymmetric vorticity dynamics that manifests TC structure and intensity through counter-propagating vortex Rossby waves (VRWs) (Hendricks et al. 2012; Kuo et al. 1999; Schubert et al. 2016). A sign reversal of the mean radial vorticity gradient supports VRWs to satisfy the Rayleigh condition for barotropic/barotropic-baroclinic instability (Montgomery and Shapiro 1995), which can further lead to a breakdown of the potential vorticity (PV) ring and redistribution of eyewall PV and angular momentum (Bell and Montgomery 2008).

Although prodigious strides have been made towards improved fundamental understanding of the observed precipitation asymmetries organized by the underlying dynamics, observations have been limited in their ability to validate the theory of VRWs and polygonal eyewalls dynamics suggested by numerical modeling. Precipitation asymmetries of polygonal structures can be captured by radar and satellite observations, but how the diabatic heating released from the convection feeds back to the dynamics, and further impacts on intensity change are difficult to examine through observations due to limited high-temporal and spatial observations of full fields throughout the atmosphere. Using observations to understand the real-atmosphere structure and numerical models to test the hypothesis of physical mechanisms are both critical to gain further insights towards improving the forecast.

1.3 Orographic dynamics and rainfall

Hills and mountains can have a profound effect on precipitation mechanisms through a combination of microphysics, dynamics and thermodynamics (Houze 2012). The growth and fallout of precipitation over a barrier are impacted by impinging wind flow, vertical velocity, boundary layer thermodynamics, shape of terrain, microphysical growth processes, and the nonlinear nature of the atmosphere (Houze 2012). Particularly, the orographically-induced air flow can modulate the vertical motion and physical processes of weather systems by altering the interaction between clouds and topography. Interactions with terrain can lead to extreme rainfall and intense convective storms (Chien and Kuo 2011; Wu 2013; Zipser et al. 2006)

To study rainfall produced by interactions with terrain, Lin et al. (2001) modified the ingredients-based methodology equation for producing rainfall R to include the topography effect:

$$R = (\vec{V}_h \cdot \nabla h + w_{env})(L/C)qE \tag{1.1}$$

where $\vec{V}_h \cdot \nabla h$ is the vertical wind induced by impinging horizontal flow to terrain, w_{env} is the vertical forcing due to the environment, L is the system length scale, C is the system speed in the direction of the length scale, q is the water vapor mixing ratio, and E is the precipitation efficiency. The orographically-forced vertical motion can act to modify and focus the ingredients locked to the terrain height associated with extreme rainfall. Separating the orographically-forced vertical motion term in the ingredient-based approach enables studies to investigate the airflow interaction with terrain.

TC interactions with complex terrain can greatly enhance the potential for an extreme precipitation event by direct lifting, precipitation efficiency, and cross-barrier flow (Houze 2012; Bell 2017). The complex terrain over Taiwan with a N-S oriented Central Mountain Range (CMR) and peaks close to 4 km can result in enhanced precipitation on the mountain slopes, such as Typhoon Herb (1996) with more than 1900 mm in 2 days (Wu and Kuo 1999), Typhoon Morakot (2009) with nearly 3000 mm in 4 days (Wu 2013), and Typhoon Fanapi (2010) with 600 mm in 7 hours (Liou et al. 2016). Orographic modification processes in TCs are variant in time, space, and scale. To the first order, terrain interactions with TC circulation can lead to the track deflection and the changes in intensity which makes intensity, track, and QPF forecasts even more challenging (Chien et al. 2008; Wu and Kuo 1999; Wu 2013). Modifications in mesoscale structure can produce variations in pressure and wind that can further lead to a potential vortex formation on the lee side of the CMR (Wu and Kuo 1999). On smaller scales, enhancement of precipitation is affected by the location of ascent that is forced to flow over the terrain. An improved understanding of the dynamics of TC and their multi-scale interaction with terrain is critically important to improving the forecasting problems through observations, numerical modeling, and synthesis between the two.

Doppler radar observations provide an avenue to understand precipitation structure associated with orographic interactions and the key ingredients impacting the intensity and duration of severe weather. High quality research radar observations can provide detailed precipitation structures and wind structures inferred by Doppler radial wind along radar beams, but two or more radars are required in order to retrieve a three-dimensional wind field (Xu et al. 2012; DeHart and Houze 2017). Although Doppler radar retrieval techniques enable scientific analyses to understand the underlying dynamics in precipitation systems, observational studies on airflow modulated by complex terrain and orographic interactions are limited due in part to limited appropriate retrieval techniques to recover airflow. Most of the retrieval techniques are designed for analyzing weather systems over flat area, but the boundary conditions of topographic forcing and surface impermeability are critical to be implemented in the techniques as airflow cannot penetrate terrain. Recovering the three-dimensional wind over complex terrain from observations is salient to advance our understanding of orographic dynamics.

1.4 Research objectives

The overarching scientific objective of this dissertation is to improve our understanding of the underlying dynamics of TC precipitation structure by using and improving radar retrieval techniques and numerical modeling. Three projects were formulated to address the following three research questions to obtain the scientific objective:

1. Can the underlying dynamics of TC polygonal precipitation asymmetries be retrieved from Doppler radar data?

2. What is the cause of the coupling between wind and reflectivity in a polygonal eyewall, and how does the coupling relate to TC intensification?

3. Can the airflow of precipitation systems over complex terrain be accurately retrieved by a multi-Doppler radar technique?

Chapter 2 investigates polygonal eyewall asymmetries of Hurricane Michael (2018) during rapid intensification (RI) by using ground-based single Doppler radar to provide high temporal resolution data and NOAA P-3 Hurricane Hunter airborne radar to provide detailed three-dimensional vortex structure.

Chapter 3 builds upon the Hurricane Michael's results by using a simple two-layer modeling framework to investigate the coupling between wind and convection through boundary layer dynamics. We use a shallow water model on top of a slab boundary layer model (SBL) to simulate a frictional boundary layer underneath the free atmosphere.

Chapter 4 implements the impermeability condition and topographic forcing at the terrain height and tests the sensitivity of imposed strength of boundary constraints, assumptions of mass continuity, Neumann and Dirichlet boundary conditions, terrain map smoothness, and settings for grid spacing and Gaussian recursive filtering by observing simulation sensitivity experiments (OSSEs) through using a full-physics model and radar emulator to quantify the uncertainties. An example of dual-Doppler radar analysis is presented when Typhoon Chanthu (2021) was over Taiwan.

Chapter 5 presents a synthesis of the principal findings in the dissertation, and discusses implications and future work.

Chapter 2

Polygonal eyewall asymmetries during the rapid intensification of Hurricane Michael (2018) [1]

2.1 Introduction

Tropical cyclone (TC) internal dynamics are a primary factor impacting the storm evolution in an environment that is favorable for rapid intensification (RI) (Hendricks et al. 2010). Inner-core processes are intrinsically less predictable and more difficult to observe in detail than the larger-scale environment, which makes forecasts of intensity change particularly challenging. The U.S. coastal Next Generation Weather Radar (NEXRAD) system network provides continuous surveillance capability of TCs with high temporal and spatial resolution, and can collect valuable data on TC evolution. The axisymmetric and asymmetric tangential winds are able to be retrieved using the Generalized Velocity Track Display (GVTD) technique with single ground-based Doppler radar data (Jou et al. 2008; Cha and Bell 2021), providing insights on the TC dynamics and evolution (Lee & Bell, 2007; Shimada et al. 2018; Cha, 2018) . Hurricane Michael (2018) was the first Category 5 hurricane to make landfall in the United States since Hurricane Andrew (1992) and caused extensive damage in Florida and Georgia (Beven et al. 2019). Satellite and radar imagery showed evidence of an evolving polygonal eyewall as Michael underwent RI during its approach to Florida. In this study, single Doppler radar winds from a coastal radar are analyzed to provide the first observational evidence of the kinematic structure of a polygonal eyewall during RI to Category 5 intensity.

---

[1] The results outlined in Chapter 2 have been published in the *Geophysical Research Letters*: Cha, T.-Y., M. M. Bell, W.-C. Lee, and A. J. DesRosiers, 2020: Polygonal eyewall asymmetries during the rapid intensification of hurricane michael (2018). *Geophysical Research Letters*, **47 (15)**, e2020GL087 919, doi: https://doi.org/10.1029/2020GL087919, URL https://agupubs.onlinelibrary.wiley.com/doi/abs/10.1029/2020GL087919, e2020GL087919 10.1029/2020GL087919, https://agupubs.onlinelibrary.wiley.com/doi/pdf/10.1029/2020GL087919. **©American Geophysical Union. Used and adapted with permission.**

Polygonal eyewalls are hypothesized to be the result of asymmetric vorticity dynamics that can modulate TC structure and intensity through counter-propagating vortex Rossby waves (VRWs) (Muramatsu 1986; Schubert et al. 1999; Kuo et al. 1999; Hendricks et al. 2012; Kuo et al. 2016). A sign reversal of the mean radial vorticity gradient that acts as a waveguide for VRWs satisfies the Rayleigh condition for barotropic-baroclinic instability (Montgomery and Shapiro 1995), which can lead to a breakdown of the potential vorticity (PV) ring and redistribution of eyewall PV and angular momentum (Schubert et al. 1999; Bell and Montgomery 2008) which can accelerate the mean wind inside the radius of maximum wind (RMW), and promote the contraction of RMW. The presence of a "ring" of mean vorticity that satisfies the Rayleigh condition can exist in both intensifying and weakening storms depending on intensity (Martinez et al. 2017), suggesting that the vortex dynamics can be complex and VRWs may lead to intensification (Menelaou and Yau 2014), rapid weakening (Martinez et al. 2019) or steady-state periods (Kossin and Eastin 2001). Lee & Wu (2018) hypothesized that polygonal eyewalls acted as a possible RI mechanism in Typhoon Megi (2010) by enhancing the generation of convective bursts inside the RMW, which then affects the development of the warm-core in the upper tropopause and the vertical alignment of the eyewall. They concluded that maintaining a certain pattern of polygonal eyewall structures within the high inertial stability region for an extended period of time is beneficial to RI.

Previous theoretical studies have often used a simplified barotropic nondivergent model framework to investigate the dynamical processes of polygonal eyewalls (Schubert et al. 1999; Kuo et al. 1999; Rozoff et al. 2009; Kuo et al. 2016). While this framework can provide substantial insight, it has limitations in investigating eyewall dynamics as moist convective processes are very important to PV generation and the intensification process. Diabatic heating can be introduced as a proxy via a mass-sink in shallow-water models (Hendricks et al. 2012, 2014) or simulated directly in 3-D full physics models (Wu et al. 2016), but simulations may not represent the real-world physical mechanisms correctly. Utilizing observational datasets is critical to validate theory and numerical simulations and improve our understanding of polygonal eyewalls in TCs and the relation to the intensity change. Prior studies have been limited in their ability to examine the dynamics of VRWs and polygonal eyewalls. Multi-Doppler airborne radar analyses (Reasor et al. 2000) can retrieve the full wind field, but have temporal sampling and aliasing limitations (Cha and Bell 2021). Studies analyzing the shape of the eye in reflectivity (Itano and Hosoya 2013) or using reflectivity as a proxy for PV (Corbosiero et al. 2006) have limitations due to the fact that the reflectivity may not be fully coupled with the winds or PV (Moon and Nolan 2015).

Analyses of Hurricane Michael (2018) presented herein demonstrate the first observation of high-order VRW propagation using tangential wind asymmetries as a proxy for the PV signal. The results show that the propagation speeds of the waves are consistent with linear wave theory on a vortex and help to provide new insight into physical mechanisms contributing to TC rapid intensification. Section 4.3 describes the observing platform, quality control processes for the observations, and analysis methodology. Section 2.3 introduces Michael's evolution with reflectivity, axisymmetric and asymmetric tangential winds retrieved by the GVTD technique, the operational radar temporal sampling limitations with high-wavenumbers propagation, and discusses the physical mechanisms contributing to Michael's inner core variability. Conclusions and future work will be presented in section 2.4.

2.2 Data and Methods

Hurricane Michael was within range of ground-based radar surveillance during its approach to the Florida panhandle and brought in devastating winds and storm surge to the coastal area near Mexico beach and Tyndall Air Force Base (AFB). Figure 2.1 shows the track, intensity, environmental vertical wind shear (VWS) direction, and reflectivity evolution at 3 km. Michael intensified nearly continuously from genesis to landfall, and experienced two RI periods during its life cycle. The second RI started on 9 October and ended when the storm reached Category 5 intensity (140 kt) at the time of landfall around 1730 UTC 10 October. After the landfall, Michael underwent a rapid weakening and extratropical transition as the TC moved into North Carolina. The analysis period for this study is from 1000 to 1930 UTC 10 October when the hurricane was within the coastal radar detection range. The deep layer 200-850 hPa VWS magnitude was about 5 m s^{-1} and the VWS direction transitioned from the southeast to the north-northeast during the analysis period.

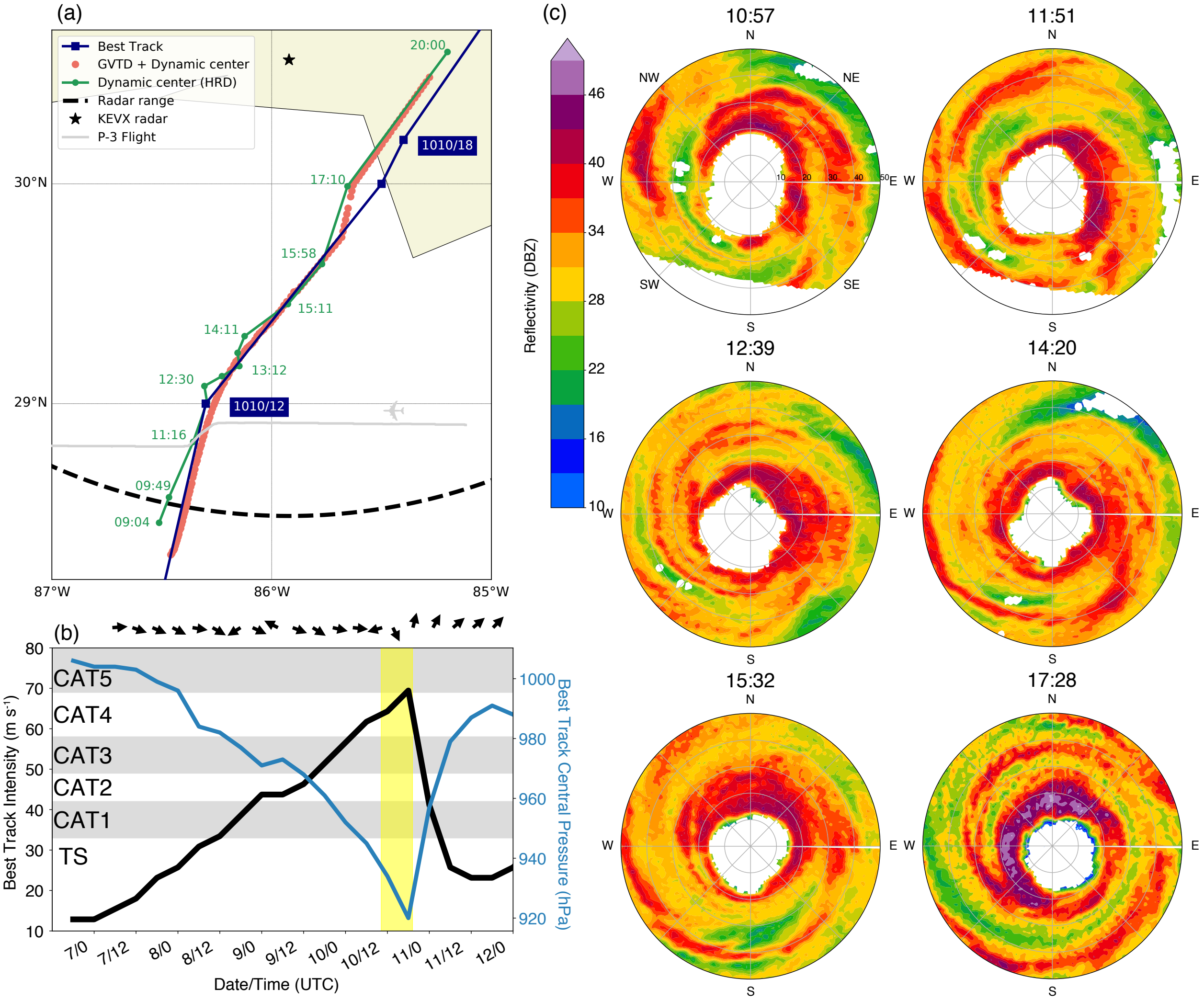

Figure 2.1: (a) Three tracks of Hurricane Michael on 10 October 2018 derived from best track from NHC (blue), GVTD-simplex objective centers (red), and aircraft dynamic centers (green) from NOAA HRD. The gray line is P-3 flight track from 11 to 1130 UTC 10 October. (b) NHC best track wind intensity (black) and minimum central pressure (purple). The black arrow on the top row is the vertical wind shear direction (black) from the Statistical Hurricane Intensity Prediction Scheme (SHIPS) database (DeMaria et al. 2005). Yellow bar indicates the analysis period. (c) KEVX radar reflecitivity scans at 1057, 1151, 1239, 1420, 1532, and 1728 UTC. The sequence of figures is from left to right and from top to bottom. The interval of concentric circles is 10 km.

Figure 2.1a shows the TC tracks derived from three different methods: best track, GVTD-simplex and dynamic aircraft location. The best track centers are surface-based estimates from the National Hurricane Center (NHC) that consider satellite, ground-based radars and in-situ measurements every 6 hours. The dynamic aircraft centers from the Hurricane Research Division (HRD) are derived from the NOAA P-3 (hereafter as P3) in-situ measurements of wind and geopotential height at 700 hPa (Willoughby and Chelmow 1982). The GVTD-simplex objective centers are obtained from the radar data at 3 km altitude using a simplex method to obtain a set of possible circulation centers (Lee et al., 1999; Lee & Marks, 2000) that are selected by an objective algorithm (Bell and Lee 2012) to smooth the track and reduce the center uncertainty. The tracks derived from the three different methods have similar trends in the earlier period, while the dynamic centers show a trochoidal motion between 1200 UTC through 1400 UTC. Two hours before landfall the three tracks started to diverge, likely due to the difference in height of the estimates and the impact of surface friction and VWS. In this study, we use the combination of GVTD objective centers from 1000 to 1530 UTC and dynamic centers from 1530 to 1930 UTC for the analysis because the GVTD-simplex algorithm cannot find the center accurately when the storm is too close to the radar.

Data from the operational Weather Surveillance Doppler (WSR-88D) radar in Eglin AFB, Florida (KEVX) were analyzed from 1000 to 1930 UTC 10 October. The radar sweep files were processed with Lidar Radar Open Software Environment (LROSE) software (Bell 2019), and the National Center for Atmospheric Research (NCAR) SoloII software (Bell et al. 2013) to correct Doppler velocity aliasing and remove the non-meteorological echoes. The edited sweep files were then gridded using interpolation of the fields from plan position indicators (elevation angle, Y, Z) to constant-altitude plan position indicators in Cartesian coordinate (X, Y, Z). The gridded data were further analyzed by the Vortex Objective Radar Tracking and Circulation (VORTRAC) software and the GVTD technique was used to retrieve the kinematic structure (Jou et al. 2008; Cha 2018). The GVTD algorithm can retrieve the axisymmetric and asymmetric components of tangential winds and axisymmetric radial wind. Since the GVTD algorithm has no approximation to the geometry, the GVTD-derived higher wavenumbers will not be distorted in phase as long as the amplitude of that wavenumber can be detected by a Doppler radar.

In addition to the ground-based radar data, the P3 aircraft flew a reconnaissance mission from 0800 UTC to 1400 UTC 10 October and collected high-resolution airborne Doppler radar data. The flight pass from 1100 to 1130 UTC 10 October is analyzed in detail for this study to examine the 3-D kinematic structure from dual-Doppler synthesis using the SAMURAI variational analysis technique (Bell et al. 2012a).

2.3 Results

Figure 2.1c shows a sequence of reflectivity images on October 10 that indicate intensification was accompanied by evolving reflectivity asymmetry. Hurricane Michael exhibited many noncircular eyewall shapes including ellipses, triangles, squares and hexagons, which transitioned from low to high to low wavenumbers and then axisymmetrized. Most of the high-order features were short-lived, with the exception of an elliptical eyewall that was traceable for an hour (1030 to 1130 UTC) with reflectivity maximized near the ends of the major ellipse axis at 1057 UTC. An hour later, the elliptical eyewall evolved into a triangle shape with reflectivity maximized on the eastern side. The asymmetries continued rotating cyclonically along the eyewall, and the eyewall became an irregular shape associated with spiral bands circulating around the eye at 1239 UTC. Michael's eyewall shape transitioned to a square at 1420 UTC, a quasi-triangular at 1532 UTC, and eventually axisymmetrized to a near round circle. After Michael made landfall at 1730 UTC, the reflectivity decreased in the southeast eyewall, while the northwestern quadrant had some of the highest reflectivity values seen during the analysis period exceeding 45 dBZ, suggesting an increasing impact of surface friction and shear.

Figure 2.2 shows a time-radius diagram of retrieved wind and derived dynamical quantities. The wavenumber-0 (axisymmetric) tangential wind (Fig. 2.2a) generally intensified until landfall with a broadening outer wind field out to 100 km radius. The mean tangential wind reached its maximum intensity (~ 65 m s^{-1}) around 1700 UTC then decayed due to land interaction and increasing shear throughout the rest of analysis period. Figures 2.2b and c show the evolution

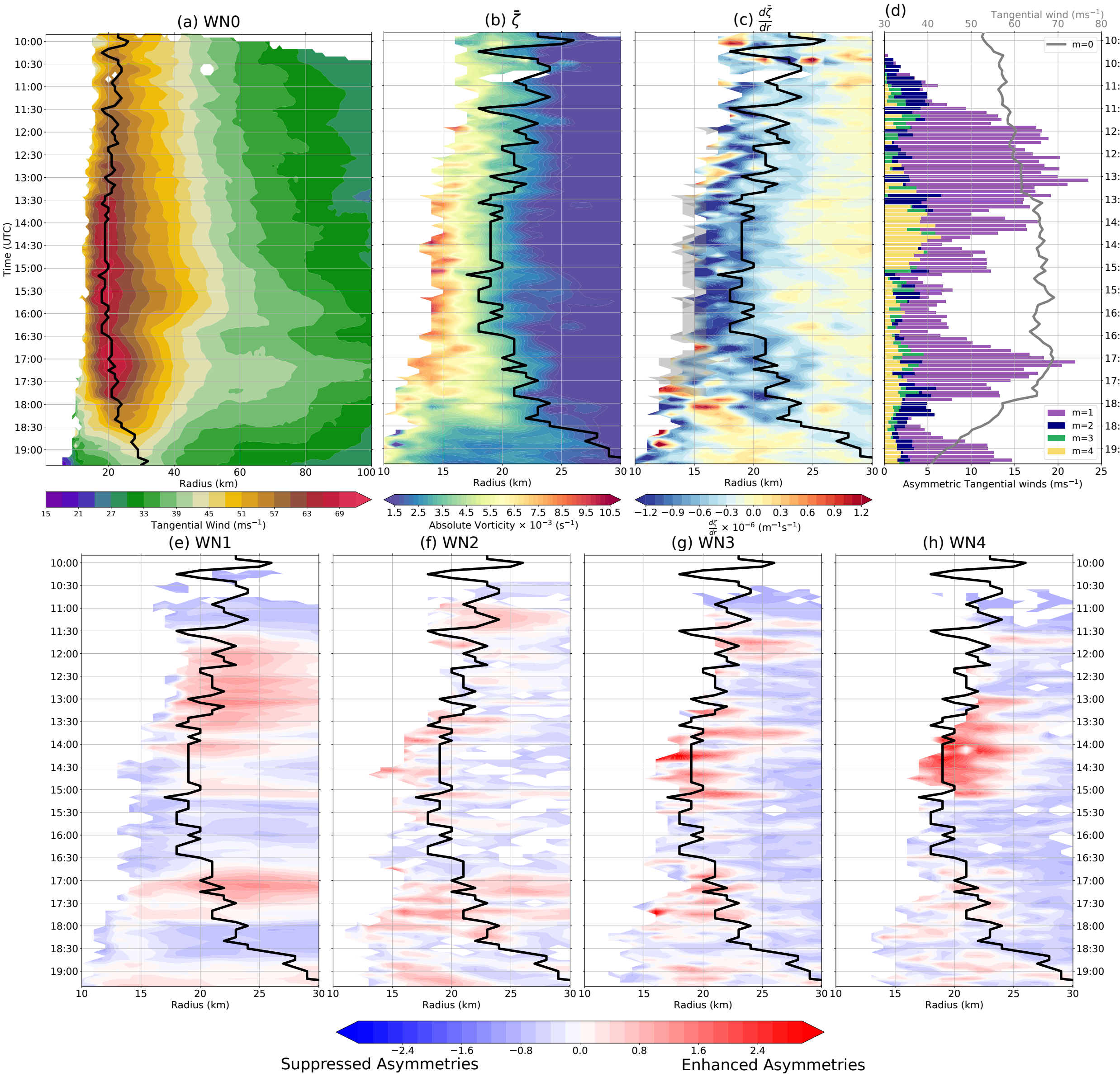

Figure 2.2: Single Doppler radar data collected in Hurricane Michael between 1000 and 1930 UTC 10 October 2018. Time-Radius diagram of the (a) wavenumber-0 tangential wind (b) mean vorticity (c) mean radial vorticity gradient at z = 3 km. (d) Time series of maximum amplitude of wavenumbers from m = 0 - 4. Time-radius diagram of the m = 1 - 4 normalized tangential wind at z = 3 km for (e) - (h). The black line in (a) - (c) and (e) - (h) indicates the radius of maximum wavenumber-0 tangential wind.

of eyewall axisymmetric vorticity and its radial gradient out to 30 km radius. The corresponding amplitude of the wavenumber 0 – 4 tangential wind components is shown in Fig. 2.2d, with the black line denoting the peak axisymmetric wind and bars denoting the asymmetric components. Due to the difference in magnitude of the asymmetric components, the normalized amplitude is shown in Figs. 2.2e-h using the time-mean value of each wavenumber within the eyewall region as a normalization factor, such that $V_{norm,m} = (V_m - \bar{V_m})/\bar{V_m}$, where V_m is the instantaneous amplitude for each wavenumber m and $\bar{V_m}$ is the time-mean value of the amplitude averaged between RMW - 5 and RMW + 5 from 10 to 1930 UTC. The normalization more clearly visualizes the relative changes in asymmetric tangential wind with warm colors denoting enhanced asymmetries and cool colors denoting reduced asymmetries. The relative changes in asymmetric tangential wind are not very sensitive to the averaging radii.

Early in the analysis period around 1030 UTC, the elliptical eyewall seen in the radar reflectivity (Fig. 2.1c) is also evident in the retrieved wavenumber-2 tangential wind component (Fig. 2.2f). By 1130 UTC, both wavenumbers-1 and 3 components strengthened (Figs. 2.2e and g). Between 1200 and 1330 UTC, the eyewall was dominated by a wavenumber-1 asymmetry that continued to intensify up to ≈ 23 m s $^{-1}$. Enhanced wavenumber-1 asymmetry is usually diagnosed as a result from the VWS impact, but the local VWS magnitude from the P3 flight radar analysis was only 2.9 m s^{-1}, suggesting that VWS was not the cause of the increasing wavenumber-1 asymmetry. The GVTD analysis and P3 in situ data suggests that wavenumber-1 asymmetries seemed more likely to be connected to internal processes in the inner core due to the presence of a trochoidal oscillation of the center at this time. Around 1300 UTC as the wavenumber-1 was near its maximum amplitude, the higher-order asymmetries were suppressed and the mean vorticity in the inner core decreased slightly. The analysis shows an appearance of a sign reversal of the mean radial vorticity gradient inside the RMW, suggesting the onset of dynamic instability.

One hypothesis for the wavenumber-1 asymmetry evolution as an algebraic instability was proposed by Smith and Rosenbluth (1990) and Nolan and Montgomery (2000). The algebraic instability is different from the barotropic instability, and the initial condition requires the initial perturbation vorticity to be inside of the angular velocity maximum for the growth to occur. Enhanced eye-eyewall mixing by the prior wavenumber 2 and 3 asymmetries may have provided that initial perturbation vorticity, but due to the lack of scatterers in the eye we cannot verify whether that was the case. Nolan and Montgomery (2000) showed that the presence of a wavenumber-1 algebraic instability causes the TC center to have trochoidal motion with respect to the time-averaged motion vector. The dynamic centers derived from aircraft in situ winds (Fig. 2.1a) show a trochoidal motion from 1223 to 1430 UTC that is consistent with the theoretical growth of this instability.

Between 1330 and 1500 UTC, high wavenumbers 3 and 4 grew in amplitude as the wavenumber-1 amplitude decreased. The RMW contracted during this period and the mean vorticity in the inner core strengthened to greater than 6×10^{-3} s^{-1}. At 1530 UTC the eyewall reflectivity pattern was triangular (Fig. 2.1c), consistent with the retrieved wavenumber-3 wind asymmetry at this time. Subsequently, Michael gradually axisymmetrized as the mean vortex intensified and the asymmetric components of tangential wind weakened by 1630 UTC. The RMW then began to expand and the magnitude of asymmetries increased again as the hurricane continued the northeastward trajectory and started to be impacted by the land interaction. Michael made landfall at 1730 UTC as the environmental VWS concurrently intensified and the hurricane intensity weakened significantly.

The analysis of Michael's inner core evolution suggests that the asymmetric VRW dynamics played an important role in modulating the structure and intensity changes. As described in the introduction, previous observational analyses have yet to document the high-wavenumber kinematic structure propagation due to lack of both high spatial and temporal resolution data. Here we use the GVTD retrieved asymmetric tangential winds as a proxy for vorticity and utilize the high temporal resolution to estimate the azimuthal propagation speed. Figure 2.3a shows an azimuth-time diagram of wavenumber-2 wind near the RMW during the period with a rotating elliptical eyewall. There is a clear cyclonic propagation of the wavenumber-2 amplitude during this time. Concurrent with this propagation, the mean vorticity structure derived from both P3 dual-Doppler and single Doppler radar analysis (Fig. 2.3b) shows a steep vorticity gradient at the inner edge of the eyewall that would support VRW propagation. There is a good agreement in the retrieved axisymmetric vorticity across all radii, providing confidence in the radar analysis for investigating the vortex dynamics.

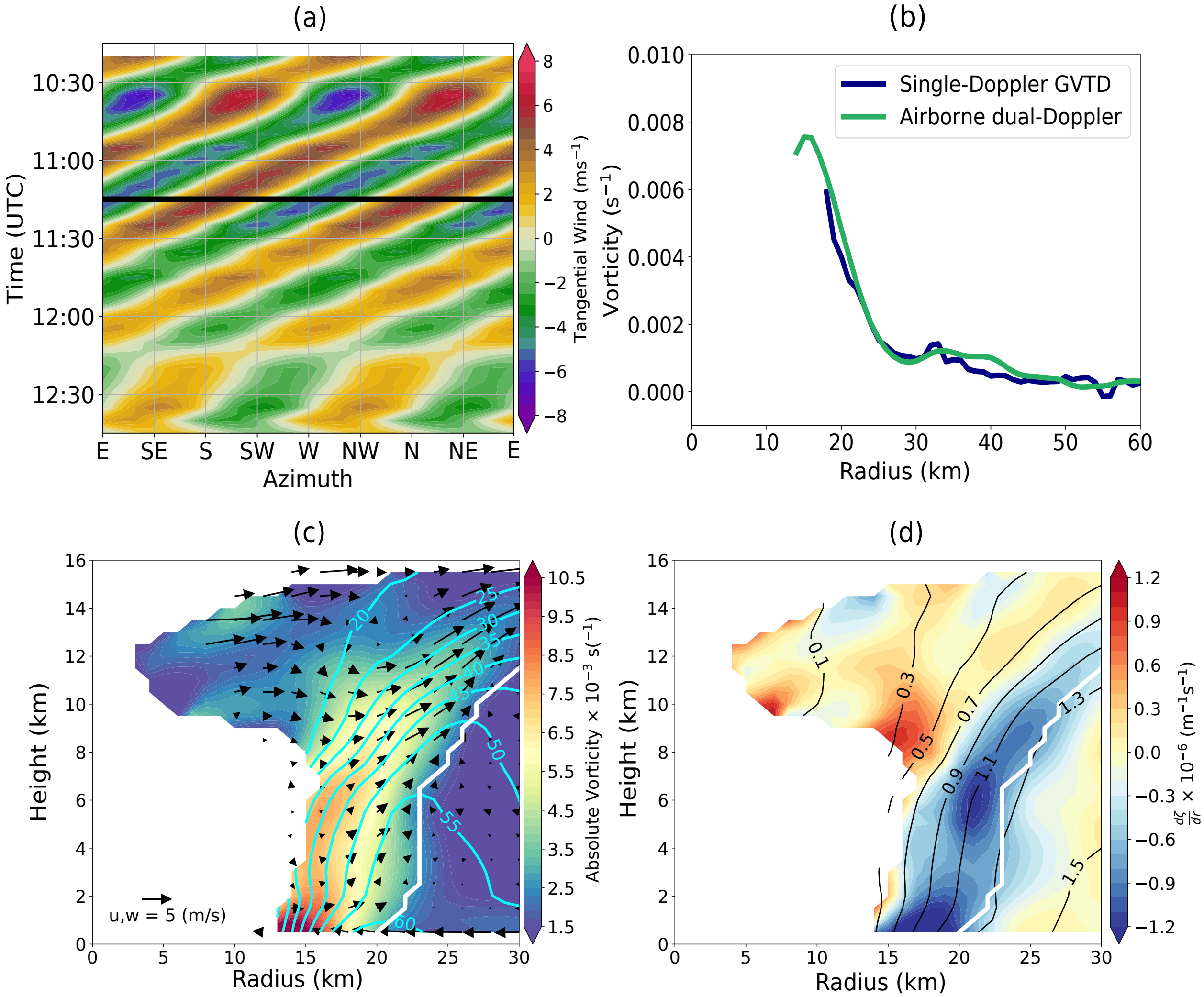

Figure 2.3: (a)Time-azimuth diagram of the wavenumber-2 tangential wind at z = 3 km averaged from r = RMW - 3 km to r = RMW + 3 km from 1020 to 1245 UTC 10 October. (b) The radial profile of axisymmetric absolute vorticity derived from the P-3 dual-Dopppler analysis (green) synthesized from 1100 to 1130 UTC, and the single-Doppler GVTD retrieval (blue) at z = 3 km on 1115 UTC 10 October, corresponding to the black line in (a). Radius-height diagram of azimuthal mean storm-relative (c) absolute vorticity (shading), secondary circulation (vector), tangential wind (cyan contour), and radius of maximum wind (white contour), (d) radial gradient of absolute vorticity (shading) and angular momentum surfaces (black contour) from the P-3 dual-Doppler analysis.

The enhanced sensitivity and pseudo dual-Doppler scanning strategy of the P3 allow for a retrieval of the full axisymmetric kinematic structure at the time of the aircraft penetration (from 1100 to 1130 UTC 10 October). Figure 2.3c shows the radius-height mean structure of vorticity, tangential wind, and secondary circulation. A local maximum of vorticity exceeding 9 × 10^{-3} s^{-1} is evident in the low-levels, with a tower of positive vorticity extending to the upper troposphere. A updraft maximum in the upper-levels suggests an ongoing development of the vorticity tower in the vertical. Due to the enhanced sensitivity of the P3 radar in the storm, a reversal in the vorticity gradient at the inner edge of the eyewall is captured by the dual-Doppler analysis at upper levels, and can be inferred at low-levels (Fig. 2.3d). The couplet of positive and negative radial gradient of vorticity satisfies the Rayleigh condition for barotropic instability that could support the exponential growth of higher order asymmetries. The tightly packed angular momentum surfaces in Fig. 2.3d are nearly upright in low-levels and slant outward in approximate congruence with the secondary circulation at upper-levels.

The elliptical and triangle eyewall patterns are hypothesized to be the result of combined barotropic/baroclinic instability. The presence of the hollow vorticity tower during that period (Fig. 2.3) suggests that wavenumber 2 and 3 modes could grow via barotropic/baroclinic instability (Terwey and Montgomery 2002) and result in vorticity mixing between the eye and eyewall. This vorticity mixing can transport the perturbation vorticity into the core, and can lead to weakening of the symmetric vortex. In Hurricane Michael however, sustained deep convection and vortex stretching were evidently able to maintain and intensify the symmetric vorticity tower despite the growth of asymmetric perturbations.

A power spectrum analysis in the frequency domain of the tangential wind and reflectivity were performed in order to calculate the propagation speed of the asymmetries quantitatively (Figs 2.4 a and b). In the supporting information (5) we provide the details of the power spectrum analysis. The asymmetric tangential winds have clearly separated spectral peaks that correspond to different azimuthal propagation speeds. The asymmetric reflectivity spectra have distinguishable peaks for the propagation signals for low wavenumbers ($m = 1$ and 2) , whereas the high-wavenumber signals ($m > 2$) are noisier and have multiple peaks of signal making it harder to recognize the propagation velocity.

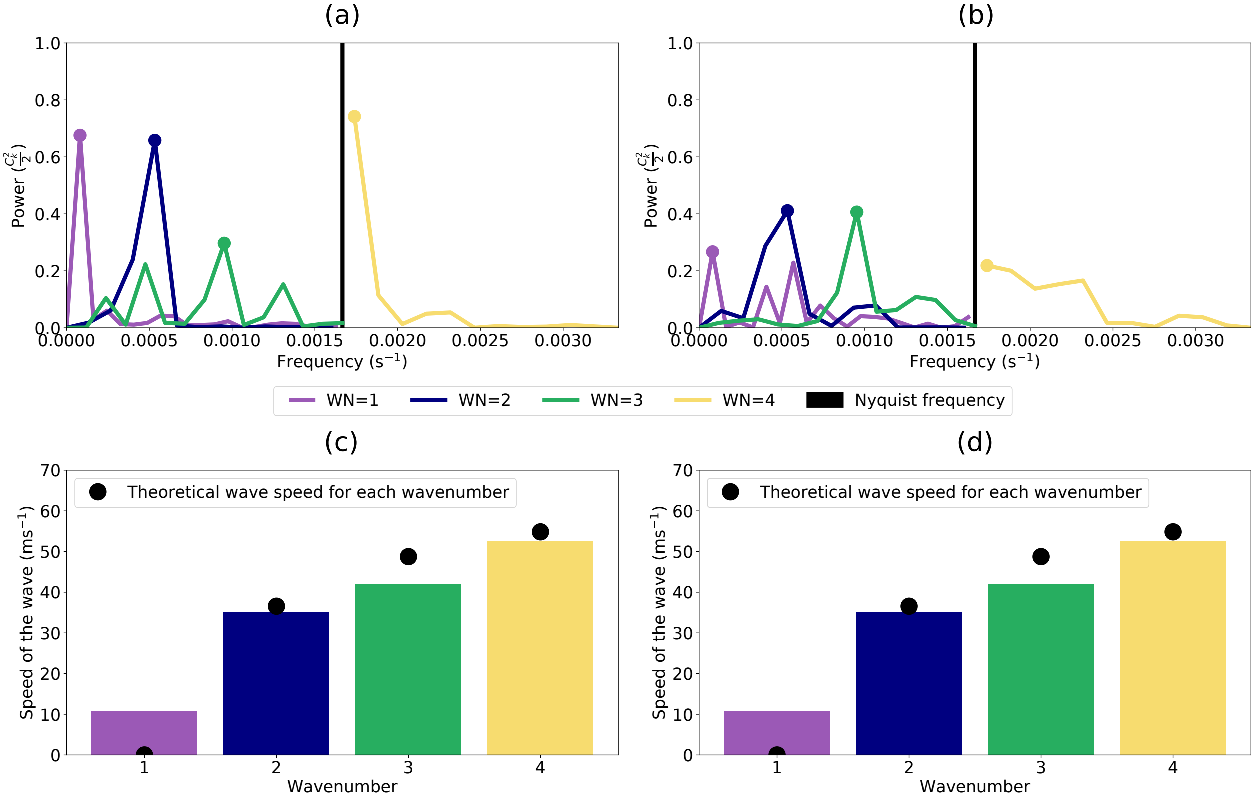

Figure 2.4: Spectral time decomposition of m = 1 - 4 (a) tangential wind components (b) reflectivity components. The Nyquist frequency is derived from the measuring frequency of the radar (0.00167 s^{-1}). The derived propagation speeds of each (c) tangential wavenumber and (d) reflectivity wavenumber and the theoretical VRWs propagation speed from the linear wave theory.

Figures 2.4 c and d display the theoretical speed calculated from equation S1 and the observed speed. The strongest power of each wavenumber is selected as the observed VRW propagation velocity. In the supporting information we provide the derivation of azimuthal velocity of each wavenumber. The observed values are remarkably consistent with the linear wave theory, suggesting that the observed asymmetries are well-described by VRW theory. Moreover, the propagation speeds of asymmetric reflectivity signals are also consistent with the linear wave theory (Fig. 2.4 d) despite the broader power spectra. The observed asymmetric propagation of both wind and reflectivity provides further support for the theoretical framework of linear wave theory, suggesting that nonlinear wave interaction may be of secondary importance in the propagation speed.

The similar propagation speed of tangential wind and reflectivity at the altitude of 3 km implies that the vorticity and divergence fields are coupled together in the low to mid-troposphere. Due to sampling limitations of the radar beam, it is unclear whether this coupling originates in the boundary layer or is only in the free troposphere. Kuo et al. (2016) used a nondivergent barotropic model for the free atmosphere and an asymmetric slab boundary layer underneath and found a tangential wind maximum at the minor axis of the elliptic vortex in the free atmosphere, whereas the wind maximum was closer to the major axis within the boundary layer. In a real, baroclinic vortex that decays with height, the theoretical wave speed for VRWs is height dependent such that a vertically coherent asymmetry that propagates at the same speed over some depth will deviate from the theory at different levels. While Michael's symmetric vorticity tower was quite strong through the depth of the troposphere (Fig. 2.3c), the mean flow still decayed with height suggesting barotropic theory cannot fully describe the evolution. The good correspondence between theoretical and observed wave speeds does indicate that barotropic theory is a reasonable approximation in this case.

Previous studies have shown that the vortex structure and the location of diabatic heating play important roles in the intensification of TCs (Schubert and Hack 1982). Latent heat release is the leading order effect in PV generation in the TC inner-core and VRWs can transport the diabatically generated PV inward (Chen and Yau 2001). In barotropic models, mixing associated with VRW activity leads to weakening of the symmetric vortex. The simultaneous amplification of symmetric vortex (Fig. 2.2b) and cycles of intensification and weakening of asymmetries (Fig. 2.3d) throughout the RI stage suggest that the asymmetries are not necessarily a negative impact on TC intensification, consistent with the recent study by Lee & Wu (2018) . Whether the vortex would have intensified even more rapidly in the absence of the asymmetries is unknown and remains to be explored with numerical modeling in future work.

2.4 Conclusion

The structure and evolution of Hurricane Michael were examined using single Doppler radar observations, providing the first observational evidence of the evolving wind field of a polygonal eyewall during rapid intensification (RI) to Category 5 intensity. Quantitative evidence of growing structures with low (1 - 4) azimuthal wavenumbers in the tangential wind and reflectivity fields suggest the presence of rapidly-evolving vortex Rossby waves (VRWs). A spectral time decomposition analysis of the retrieved winds indicates that the propagation speeds of different VRWs are consistent with linear wave theory on a symmetric radial vorticity gradient. The appearance and growth of the asymmetries is proposed to be the result of a combination of wavenumber-1 algebraic instabilities and higher order barotropic/baroclinic instabilities. Aircraft center fixes document a period of trochoidal motion with an enhanced wavenumber-1 asymmetry when all other higher wavenumber asymmetries were suppressed. A period of higher-order VRW growth followed as the mean radial vorticity gradient amplified and the hollow vortex tower contracted, eventually becoming nearly symmetric prior to landfall. The simultaneous amplification of the symmetric vortex and cycles of growth and decay of asymmetries suggest that they were closely coupled. After Michael made landfall, both wind intensity and minimum pressure weakened significantly and the asymmetries increased due to land friction and increasing vertical wind shear.

The results presented here highlight the value of coastal radar observations to investigate physical mechanisms of TC intensity and structure evolution with high temporal and spatial resolution. Airborne dual-Doppler radar analysis supports the single Doppler wind retrievals and documents the vertical structure of the growing vorticity tower, indicating the necessary condition for barotropic/baroclinic instability. The evolution of the vorticity gradient derived from the single Doppler analysis further presents new insights on intensity and structure change, which will help to improve TC forecasts in the future. In addition, both the reflectivity and tangential winds show evidence of polygonal structure and propagate at a similar speed, indicating that the vorticity and divergence fields are closely coupled together. The interaction between the asymmetric vortex dynamics and diabatic generation of potential vorticity by the convection may play a salient role in rapid intensification and is an important topic for future research.

Chapter 3

Elliptical Eyewall Evolution in a Two-Layer Model

3.1 Introduction

Radar and satellite imagery have captured polygonal eyewall structures in numerous intensifying tropical cyclones (TCs), such as Typhoon Herb (1996) (Kuo et al. 1999), Hurricane Isabel (2003) (Kossin and Schubert 2004), Dolly (2008) (Hendricks et al. 2012), Karal (2010) (Guimond et al. 2016), and Michael (2018) (Cha et al. 2020). Since the precipitation structure is usually organized by the underlying dynamics, numerous theoretical studies have conceptually described the dynamics behind the observed polygonal shape in the context of the growth of barotropic or combined barotropic-baroclinic instability through counter-propagating vortex Rossby waves (VRWs). This instability can further lead to the breakdown of an enhanced potential vorticity (PV) ring and eye-eyewall mixing (Kuo et al. 1999; Schubert et al. 1999; Hendricks et al. 2010). In Chapter 2, it was demonstrated that barotropic theory is a reasonable approximation to explain the polygonal eyewall structure as a result of VRWs, and suggested a close coupling of the vorticity asymmetries and convective asymmetries through analysis of observed evolving reflectivity and retrieved tangential wind asymmetries of Hurricane Michael during rapid intensification. Remote sensing and in-situ measurements are able to obtain the detailed convective, dynamic, and thermodynamic characteristics, but are difficult to link the key physical processes due to limited high-temporal and spatial observations of full fields. Therefore, the mechanisms that force deep convection at the polygon vertices observed in nature, and how the convective asymmetries play a role in TC intensification were unable to be addressed with the observational dataset.

Full-physics modeling can provide four-dimensional dynamical and thermodynamical fields to study the relationships between eyewall dynamics and convective processes, but the results can depend on the design, initial conditions, and physics of the model. Additionally, the dynamics in full-physics models can be hard to interpret due to complex interactions among many different processes. An alternate approach to understanding the dynamics involves models with less complexity. A balanced vortex framework has been frequently employed to understand TC intensification, which assumes that an axisymmetric vortex continuously evolves in a state of gradient wind and hydrostatic balance (Eliassen 1951; Schubert and Hack 1982; Willoughby 1979; Smith et al. 2018). Although an axisymmetric balanced vortex framework can provide many insights to TC intensification (Ooyama 1969), it is unable to fully represent asymmetric mechanisms and boundary layer processes due to the inherent assumptions. In this study, we investigate the relationships between the asymmetric convection and vortex dynamics by using an asymmetric framework with an intermediate complexity in between full-physics and balanced models.

Previous studies using unforced nondivergent barotropic models have provided a basic understanding that an annular ring of high PV is barotropically unstable, and the PV mixing leading to a stable configuration results in weakened maximum winds. Although unforced models can explain the axisymmetrization of asymmetries observed in nature, but are unable to explain why TCs can still undergo intensification in the real atmosphere. Forcings by frictions and diabatic heating involving complex convective processes are critical in nature. Rozoff et al. (2009) developed a forced barotropic model by parameterizing diabatic heating as a vorticity generation term in an annular region representative of an eyewall. They show that the barotropic instability and vorticity mixing are a brief intensification brake, but continued forcing can lead to further intensification. Their results suggest that a forced vorticity generation in the eyewall allows for the rebuilding of an annular vorticity ring and intensification.

Building upon the Rozoff et al. (2009) study, Hendricks et al. (2014) advanced this approach by using a forced shallow-water model, which includes divergent effects and a parametrization of convective diabatic heating as a time dependent annular mass sink of various widths. Their results show that a constant net heating prescribed in the region of high inertial stability inside the radius of maximum wind can lead to intensification. Hendricks et al. (2014) notes that "...when the heating is prescribed to be proportional to the relative vorticity, the maximum velocity increased and the minimum pressure decreased during barotropic instability...". Both Rozoff et al. (2009) and Hendricks et al. (2014) demonstrate that intensification can occur with sufficient forcing even in the presence of barotropic instability.

Schubert et al. (2016) presented another approach to parameterize diabatic heating in an axisymmetric shallow water framework. Their approach parameterizes diabatic heating as a mass sink proportional to the fluid depth, resulting in a non-conservative contribution to the PV equation. They developed an analytic solution for TC intensification based on the Salmon (2014) wave-vortex approximation and prescribed heating. We adopt a similar approach to parameterize diabatic heating in the current study, but allow the forcing to be determined by the atmospheric flow.

Organized moist deep convection originates from the TC boundary layer (TCBL) where the surface heat fluxes and radial inflow provide fuel for intensification and maintenance (Ooyama 1969). An axisymmetric slab TCBL model employed by Williams et al. (2013) shows that a sharp radial gradient of inflow within a few kilometers produces a shock-like structure, which leads to strong updrafts to initiate convection in TC. Their results, Kepert and Wang (2001); Kepert (2017), and others have demonstrated that the location of strong updrafts is closely coupled to the boundary layer processes. A cloud resolving model simulation of supertyphoon Haiyan (2013) conducted by Tsujino and Kuo (2020) shows that the coupling of a TCBL strong updraft and large vorticity could build a PV tower, which suggests that TCBL processes can play an important role in determining the location of heating, generating PV, and intensifying the TC.

To study why deep convection locates at the vertices of a polygonal eyewall, Kuo et al. (2016) used a simple framework with a two-layer non-divergent barotropic model coupled with a slab boundary layer. They used a time-varying pressure gradient forcing derived from the barotropic model to drive the winds in the SBL model. Their results show that VRWs in the free atmosphere can organize the updrafts in the slab boundary layer, suggesting that deep convection should be located close to the vertices, and rotate in concert with the VRWs. While their finding sheds light on the dynamics of polygonal eyewalls we see in nature, the two-layer model they employed may be oversimplified. A non-divergent barotropic model has limitations to study the effects of free atmospheric divergence. Their modeling setup allows one-way interaction only, such that the TCBL cannot influence the free atmosphere. Furthermore, the barotropic model is unforced and has no vorticity source term, so the framework cannot be used to study TC intensification.

In this study, we develop a novel framework believed to capture the essential dynamics of the problem with a divergent shallow water model (SWM) on top of a slab boundary layer model (SBL) to emulate a frictional boundary layer underneath the free atmosphere. We seek to investigate both how the deep convection is organized at the vertices and how the heating from the convection impacts TC intensification. The two-layer model maintains an approximate gradient wind balance in the free atmospheric layer and parameterizes the diabatic heating produced by convection from the vertical motion out of the boundary layer. This approach avoids prescribing the location and strength of the heating as has been done in previous studies. In our framework, the evolution of the free atmosphere and the heating from the TCBL are closely coupled. Section 3.2 describes the model and experiment design. Section 3.3 presents the results from the numerical experiments, and a discussion and summary is given in section 3.4.

3.2 Model and Experimental Design

A simple modeling framework of a shallow water model on top of an asymmetric slab boundary layer model is used in the study. The one-way model allows the pressure gradient force from the shallow water layer to modulate the wind field in the slab boundary layer, but the boundary layer's flow cannot feed back to the upper layer. The two-way model allows for the two-way interaction. Details of the model design are shown below.

3.2.1 One-way model

The shallow water model (SWM) on an f plane solves the set of equations of inviscid flow with no diffusion and friction in a polar coordinate:

$$\frac{\partial u}{\partial t} = -u\frac{\partial u}{\partial r} - v\frac{\partial v}{r\partial \lambda} + fv + \frac{v^2}{r} - \frac{\partial (gh)}{\partial r}, \tag{3.1}$$

$$\frac{\partial v}{\partial t} = -u\frac{\partial v}{\partial r} - v\frac{\partial v}{r\partial \lambda} - fu + \frac{uv}{r} - \frac{\partial (gh)}{r\partial \lambda}, \tag{3.2}$$

$$\frac{\partial h}{\partial t} + \frac{\partial (ruh)}{r\partial r} + \frac{\partial (vh)}{r\partial \lambda} = 0 \tag{3.3}$$

where u is the radial velocity, v is the tangential wind h is the fluid depth, f is the Coriolis parameter and is set to 5.0 x 10^{-5} s $^{-1}$, and h is the deviation of the fluid height from the mean depth H in the SWM, which is set to a constant 2000.0 meters. For the one-way model, the SBL cannot feed back to the SWM, so the potential vorticity $P = (f + \zeta)/h$ is materially conserved. Relative vorticity ζ is defined as ζ=$\partial(rv)/r\partial r$-$\partial u/r\partial\lambda$, and the material derivative D/Dt=$\partial/\partial t +$ $u(\partial/\partial r) + v(\partial/r\partial\lambda)$.

In order to address the asymmetric dynamics in the boundary layer, the governing equations in a polar coordinates following (Williams et al. 2013; Williams Jr. 2015), which are

$$\frac{\partial u_b}{\partial t} = -u_b\frac{\partial u_b}{\partial r} - v_b\frac{\partial u_b}{r\partial \lambda} + w^-\left(\frac{u - u_b}{h_b}\right) + \left(fv_b + \frac{v_b^2}{r}\right) - g\frac{\partial h}{\partial r} - C_D U\frac{u_b}{h} + K\nabla^2 u_b \tag{3.4}$$

$$\frac{\partial v_b}{\partial t} = -u_b\frac{\partial v_b}{\partial r} - v_b\frac{\partial v_b}{r\partial \lambda} + w^-\left(\frac{v - v_b}{h_b}\right) - \left(fu_b + \frac{u_b v_b}{r}\right) + g\frac{\partial h}{r\partial r} - C_D U\frac{v_b}{h} + K\nabla^2 v_b \tag{3.5}$$

$$w_b = -h\left(\frac{u_b}{r} + \frac{\partial u_b}{\partial r} + \frac{\partial v_b}{r\partial \lambda}\right), \tag{3.6}$$

$$\tag{3.7}$$

The 10-m wind speed used to calculate surface fluxes is

$$U = 0.78\left(u_b^2 + v_b^2\right)^{\frac{1}{2}} \tag{3.8}$$

and

$$w^{-} = \frac{1}{2}\left(|w_b| - w_b\right) \tag{3.9}$$

is the rectified Ekman suction, which results in a source term for the horizontal momentum in the boundary layer. u_b is the radial wind, v_b is the tangential wind in the boundary layer, and w_b is the diagnostic vertical wind at the top of the boundary layer. A constant C_D drag coefficient is set to 2.4×10^{-3} following (Bell et al. 2012b), the horizontal diffusion K is set to 1500.0 $\mathrm{m}^2\ \mathrm{s}^{-1}$, and the height of the slab layer h_b is set to a constant 1000.0 meters. Additional details on the equation set can be found in (Williams et al. 2013).

The two-layers are primarily coupled together via the pressure gradient, which is largely in gradient balance with the rotational wind. The pressure gradient drives the SBL model and leads to sub- and supergradient winds, radial inflow, and BL pumping w, due to the force imbalance from the surface drag and mixing terms. The SBL model is solely driven by the free atmosphere dynamics from the pressure gradient terms and the downward-only vertical momentum flux associated with the w^{-} terms.

3.2.2 Two-way model

For the two-way model, we include a mass sink term $S(r, \lambda, t)$ (s^{-1})which simulates the effect of diabatic heating in a continuously stratified, compressible fluid. Unlike previous models that parameterized the effects of eyewall diabatic heating from a prescribed set of functions, here we allow the vertical motion to freely develop in response to the atmospheric and BL forcing.

We assume that the mass sink is proportional to the vertical motion produced by convergence and divergence in the boundary layer.

$$S(r, \lambda, t) = w_b S_1 \tag{3.10}$$

where S_1 is a constant and set to 10^{-5} m^{-1}. A larger value of S_1 corresponds to more intense heating for a given w. Equation 3.3 now becomes

$$\frac{\partial h}{\partial t} + \frac{\partial (ruh)}{r\partial r} + \frac{\partial (vh)}{r\partial \lambda} = -hS \tag{3.11}$$

Because of the mass sink term, P is no longer materially conserved, which becomes

$$\frac{DP}{Dt} = SP, \tag{3.12}$$

Therefore, P in the free atmosphere can be generated by the updraft coming out of the boundary layer in a similar manner to vertical gradients of heating in the Rossby-Ertel formulation in a stratified fluid. We note that this parameterized heating is a simplification that neglects entrainment and does not allow for any vertical structure in the heating profile. However, as will be shown the parameterization can act in a similar way to deep convection in a TC that leads to intensity and structure change.

3.2.3 Initial condition

We use the initial vorticity profile that resembles the axisymmetric Rankine vortex, and let it run for 3 hours to develop the boundary layer flow. The initial profile is

$$V_T = V_{max}\left(\frac{R}{R_{max}}\right), \qquad R \le R_{max}, \tag{3.13}$$

$$V_T = V_{max}\left(\frac{R_{max}}{R}\right), \qquad R > R_{max} \tag{3.14}$$

This idealized Rankine vortex possesses a circular rotation under the gradient wind balance with no transverse circulation. V_{max} is set to 50 m s^{-1} and R_{max} is set to 50 km. The mass field is initialized in gradient wind balance, which

$$\frac{V^2}{r} + fV = g\frac{\partial h}{\partial r} \tag{3.15}$$

We input this idealized profile to the two-layer model but allow one-way only, which means that the pressure gradient force in the shallow-water model can organize and develop the flow in the boundary layer, but the flow in the boundary is not allowed to feed back to the shallow water. The model integrates the momentum equation, and develops the radial flow and the boundary layer flow after running it for several hours. We take the output at 3 hours when the boundary layer flow is developed as the initial conditions for subsequent experiments with asymmetries and two-way forcing.. The wind flow in the shallow water model is still close to a Rankine profile and maintains approximate gradient wind balance. A “shock” like structure of the tangential wind is developed in the boundary layer, accompanied by the enhanced updraft up to 5 m s^{-1} and a strong radial inflow around -24 m s^{-1}. The supergradient winds are inside the local RMW. The sharp radial gradient of radial flow transitioning from inflow to outflow around the R_{max} suggests a convergence of radial momentum and an induced updraft, which is consistent with the vertical velocity profile. In this simple analytic case, the mean vorticity is mainly 0.002 s^{-1} inside the R_{max} with a very small deviation due to numerical integration. The mean vorticity radial gradient is near zero inside R_{max} and with a sharp negative radial vorticity gradient between 40 and 60 km, supporting the propagation of stable wave perturbations. The fluid depth field shows the effective pressure gradient that drives the flow in the boundary layer.

After the initial spin-up of the model and SBL response, we then add a wavenumber 2 vortex Rossby wave perturbation to the vortex following (Lamb 1932; Lee et al. 2006):

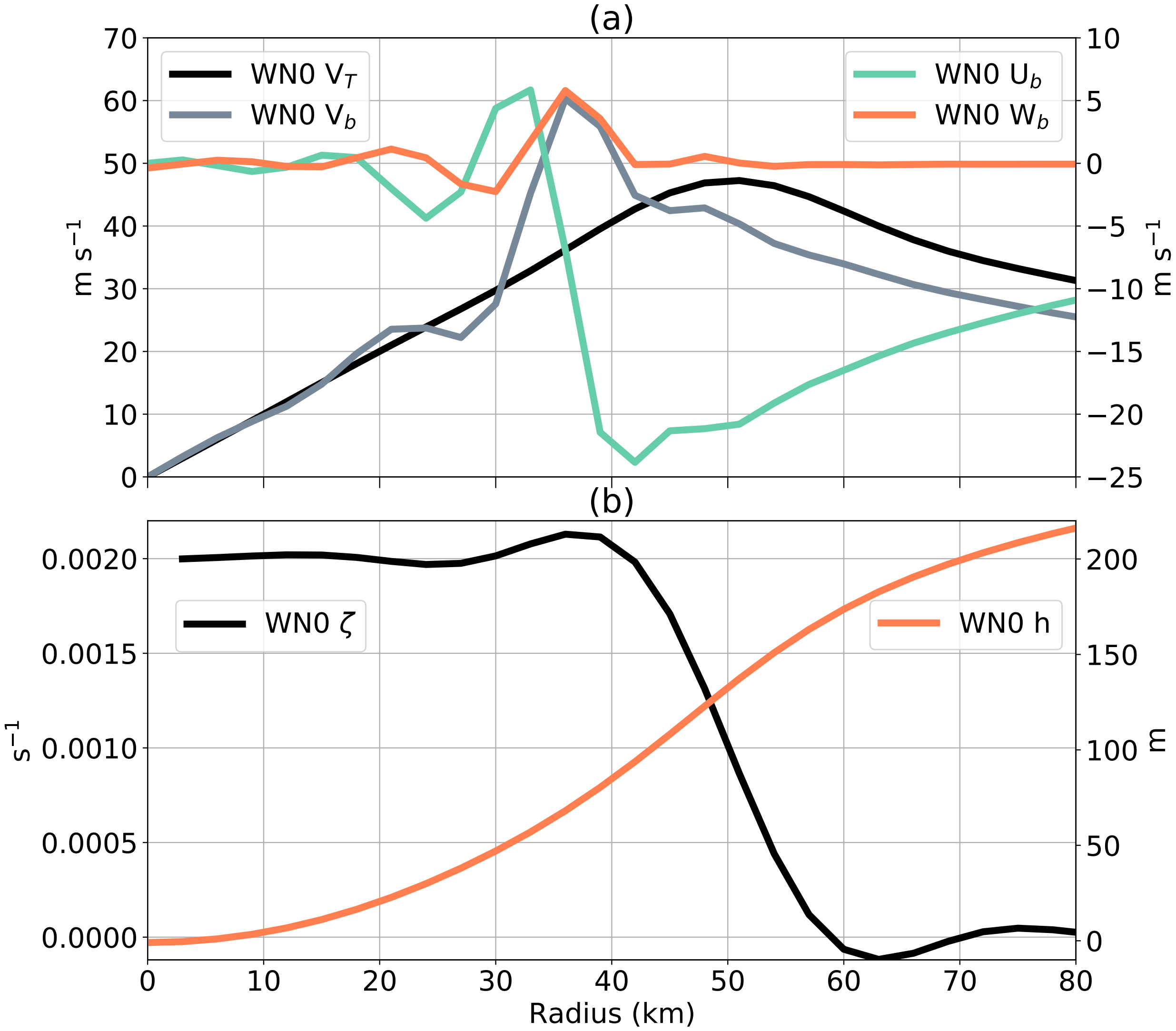

Figure 3.1: The initial axisymmetric radial profile of the wind flow, vorticity, and the shallow water depth deviation from the mean.

$$V_T = \frac{1}{2}\zeta R\left(\frac{\epsilon}{R_{max}} cos(2\lambda)\right), \qquad R \le R_{eli}, \tag{3.16}$$

$$V_T = -\frac{1}{2}\zeta \frac{R_{max}^2}{R}\left(\epsilon \frac{R_{max}}{R^2} cos(2\lambda)\right), \qquad R > R_{eli}, \tag{3.17}$$

$$V_R = \frac{1}{2}\zeta R\left(\frac{\epsilon}{R_{max}} sin(2\lambda)\right), \qquad R \le R_{max}, \tag{3.18}$$

$$V_R = \frac{1}{2}\zeta \frac{R_{max}^2}{R}\left(\epsilon \frac{R_{max}}{R^2} sin(2\lambda)\right), \qquad R > R_{eli}, \tag{3.19}$$

where ϵ is a scaling factor set to 5 km, and $R_{eli} = R_{max} + \epsilon cos(2\lambda)$ is the elliptical boundary of maximum winds. This perturbation superimposes a wavenumber two disturbance onto the Rankine vortex.

The magnitude of the tangential and radial wind of this wavenumber 2 VRW is the same but with a $\pi/4$ (45^o degree) difference across all radii. The wavenumber 2 disturbance manifests itself as two pairs of counter-rotating vortices. The total circulation becomes an ellipse with the added wavenumber 2 disturbance. This profile with a balanced Rankine vortex and added wavenumber 2 VRW is used as the initial condition for running subsequent one-way and two-way experiments.

3.2.4 Numerical model design

The numerical model is formulated in polar coordinates using the spectral transform method (Orszag 1970) to integrate the coupled shallow water and boundary layer equations forward in time. The spatial fields are discretized using finite elements in the radial direction and Fourier series in the azimuthal direction. The finite elements are cubic b-splines (Ooyama 2002a) similar to the numerical representation in the SAMURAI variational analysis package (Bell et al. 2012a). The radial nodal spacing of the b-spline amplitude points is 3 km, with 3 Gaussian quadrature points in between each node that are spaced ~1 km apart. One advantage of the finite elements over periodic basis functions is the ease of imposing boundary conditions. The boundary conditions are a Dirichelet zero wind condition at the origin for u, v, and w, and a Neumann zero first derivative at the outer boundary.

In the azimuthal direction, a reduced Gaussian grid is employed starting with 8 points around the circle at the radius closest to the origin. Four points are added at each successive radius, and are offset from the previous ring to form approximate triangles in physical space. This arrangement is similar to that employed in the 'octahedral' grid employed by the European Center for Medium Range Weather Forecasting (ECMWF) global model where the spherical Earth is approximately projected onto an octahedron. In the current polar geometry, the grid is essentially a triangular tesselation with ~1 km spacing between gridpoints throughout most of the domain, with slightly smaller spacing near the origin.

The time integration is similar to that described by Ooyama (2002a). Here we use a 3rd order Adams-Bashforth time integrator which provides better numerical stability and accuracy than the second order method (Durran and Blossey 2012). A time step of 3 seconds is used for the integration.

At each time step, the spectral amplitudes of the Fourier modes and cubic b-spline elements are used to calculate the wind and fluid depth at each gridpoint in physical space in both layers. The spectral method allows for high accuracy in the calculation of the spatial derivatives in both the radial and azimuthal directions. Nonlinear advection terms are calculated in physical space, then transformed back into spectral amplitudes to be applied as time tendencies. The Fourier amplitudes are filtered according to the 'cubic representation' such that the shortest wave on the grid is represented by 4 points. This filtering and the transform method eliminates spectral aliasing in the nonlinear terms.

The so-called 'pole problem' associated with converging radials near the origin is handled through the combination of the reduced Gaussian grid and the Fourier filtering. At the ring closest to the origin, only azimuthal wavenumber 1 is retained after filtering. Increasing wavenumbers are allowed as the number of points is increased radially. The model shows good numerical stability and accuracy in a wide variety of test cases and in the scientific results presented herein.

3.3 Results

Time series of the one-way and two-way simulations of the maximum wavenumber 0 tangential velocity and the radius of maximum wind in the SWM are shown in Figure 3.2. Since the SBL is not allowed to transport momentum upward in the one-way model and there are no other forcings, the maximum wavenumber 0 tangential wind in the SWM stays mostly unchanged with a magnitude oscillated between 40 and 45 m s^{-1} due to the model numerical integration, suggesting that the simulation reaches to a steady state since there is neither source added nor dissipation. The radius of maximum wavenumber 0 tangential wind (RMW) is mostly at around 50 km, same as our initial condition setup.

The two-way interaction simulation allows for the diabatic heating to freely develop and heat up the free atmosphere. The maximum wavenumber 0 tangential wind continues to intensify throughout the simulation, but at a different intensification rate. The first time period denoted by the black dashed line has an intensification rate of 0.7 m hr^{-1} after applying a 1-2-1 filter to damp the noise. The second time period denoted by the red dashed line has an intensification rate of 1.6 m hr^{-1}, which surpasses the rapid intensification (RI) standard. The RI definition is shown in Chapter 2 (Kaplan and DeMaria 2003). Oscillations in the wavenumber 0 tangential wind intensity are found in the time series between 400 and 800 minutes, suggesting the presence of asymmetries. After 800 minutes, there are less oscillations, and the wind speed intensifies steadily. The purple dashed line denotes the time when the intensification rate slows down with a reappearance of intensity oscillation, suggesting that the structure becomes dynamical unstable again. Figure 3.2b shows the contraction of the radius of maximum wind for the two-way simulation. During the first period, the RMW oscillates around 42 km but does not change much. When the tangential wind steadily intensifies (period 2), the RMW contracts from 40 km to 35 km within 6.4 hr. The contraction rate becomes slower after 1100 minutes and the RMW stays around 30 km while the tangential wind continues to intensify.

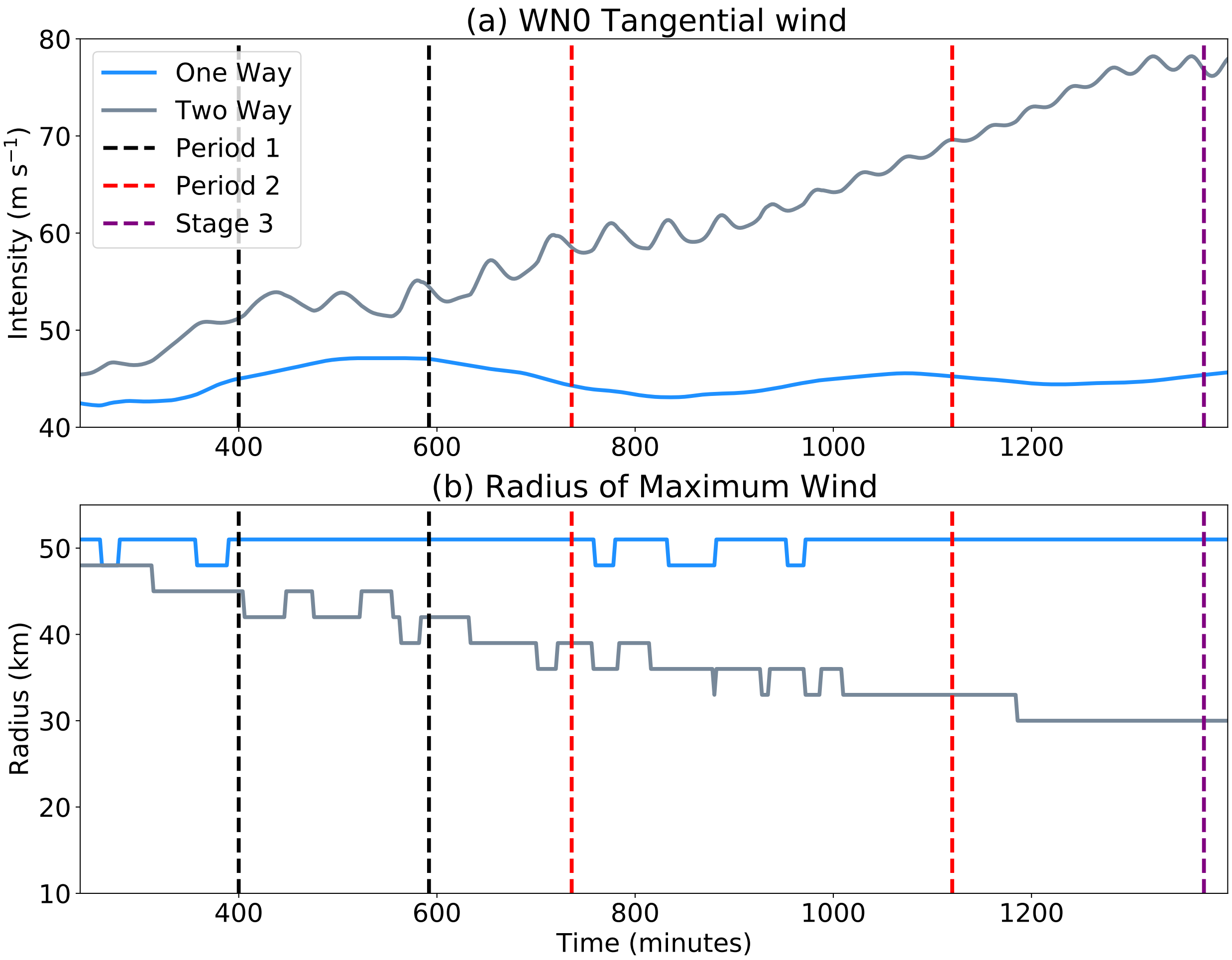

Figure 3.2: Time series (in minutes) of (a) maximum wavenumber 0 tangential velocity, and (b) radius of maximum wind (RMW) for the shallow-water layer in the one-way and two-way simulations. Time period of the subsequent horizontal cross sections is denoted by the dashed lines.

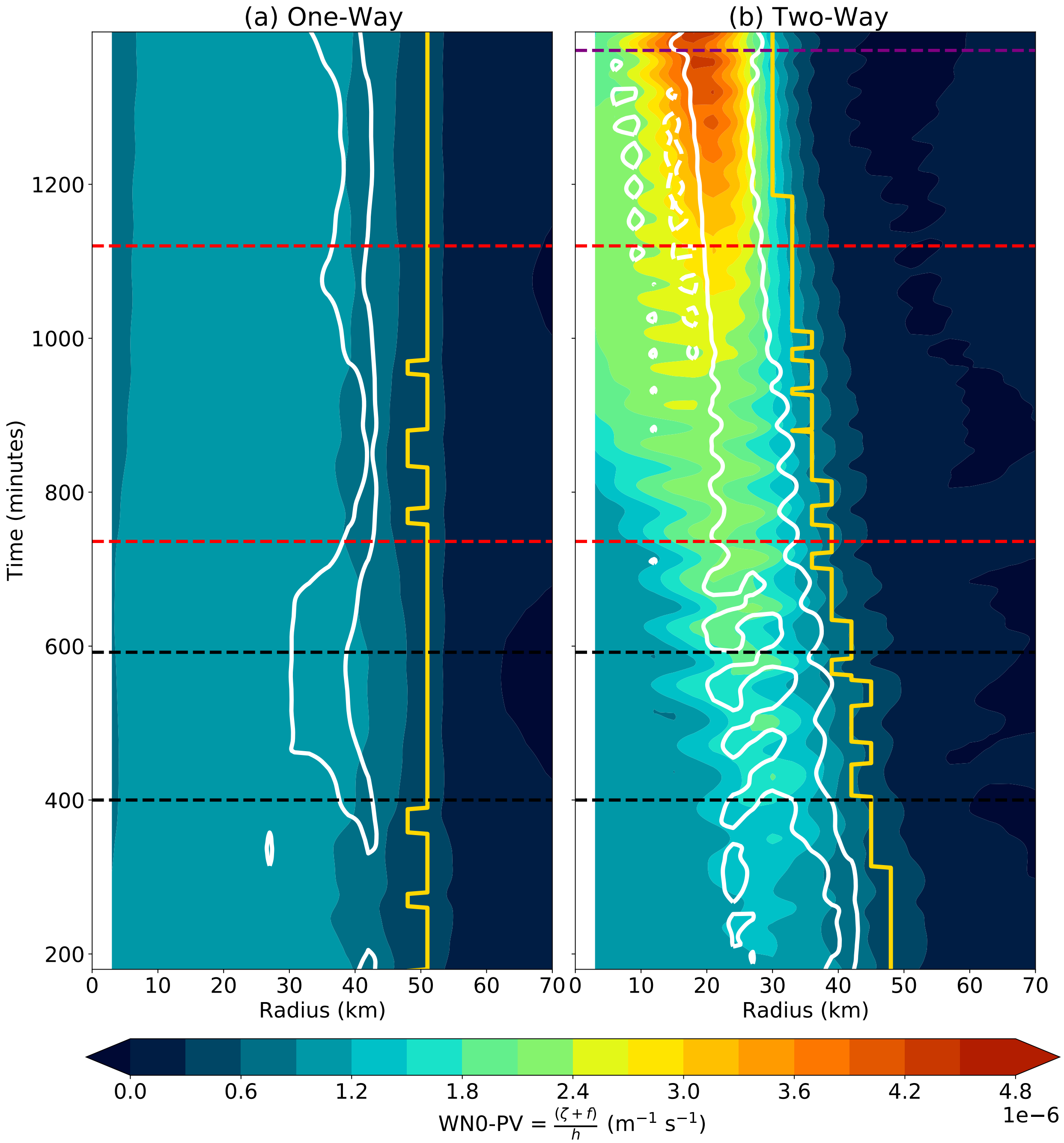

Figure 3.3: Time radius diagram of wavenumber 0 potential vorticity (shading) in the SWM and the wavenumber 0 vertical velocity (white contour with an amplitude of 2 m s^{-1} in the SBL. The yellow line denotes the RMW, and the dashed lines denote the time periods which are consistent with Fig. 3.2.

Figure 3.3 shows a time-radius diagram of the wavenumber 0 PV in the SWM and the wavenumber 0 vertical motion in the SBL. The wavenumber 0 PV in the one-way model stays mostly unchanged with a monopole structure, and the wavenumber 0 updraft locates about 10 km inwardly than the RMW, consistent with Kepert (2017). The wavenumber 0 PV in the two-way model starts from a monopole structure, and an enhanced PV appears between 25 and 35 km radius after running the model for 200 minutes. The PV ring collocates with the updraft in the SBL and continues to intensify and contract. The PV ring breaks down and evolves into a monopole after 800 minutes, and an enhanced PV signal starts to appear around 950 minutes, suggesting the onset of the PV ring development. The PV continues to intensify and the enhanced PV ring collocates with the wavenumber 0 upward motion. The transient slow-down of the intensification and reintensification are similar to Rozoff et al. (2009)'s result.

Figure 3.4 shows a time-radius diagram of wavenumber 0 tangential and wavenumber 2 PV amplitude. The one-way experiment shows the presence of wavenumber 2 signal from 200 to 450 minutes, and the asymmetry weakens following by intensifying wavenumber 0 tangential wind. When the tangential wind becomes weaker around 700 minutes, the wavenumber 2 asymmetry appears. The reverse pulses of amplification of symmetric vortex and asymmetries may suggest that the growth of symmetric vortex may be at the expense of decaying asymmetries, but more budget analyses are needed to address the interaction between the mean and the asymmetries. The two-way experiment shows that the wavenumber 0 tangential wind is up to 48 m s^{-1} at 200 minutes while the one-way experiment vortex is below 45 m s^{-1}. Interestingly, even though the two experiments were initialized with the same wavenumber 2 VRW perturbation, the two-way experiment does not have an enhanced wavenumber 2 PV signal until 500 minutes. The PV perturbation depicted by the selected contour appears at around 500 minutes and diminishes at around 900 minutes. In the meantime, the wavenumber 0 tangential wind continues to intensify with some fluctuations in intensity, accompanying by the contraction of RMW. After the depicted 5×10^{-7} (m^{-1} s^{-1}) wavenumber 2 PV contour disappears, the mean tangential wind intensifies with an even faster intensification rate, and reaches over 80 m

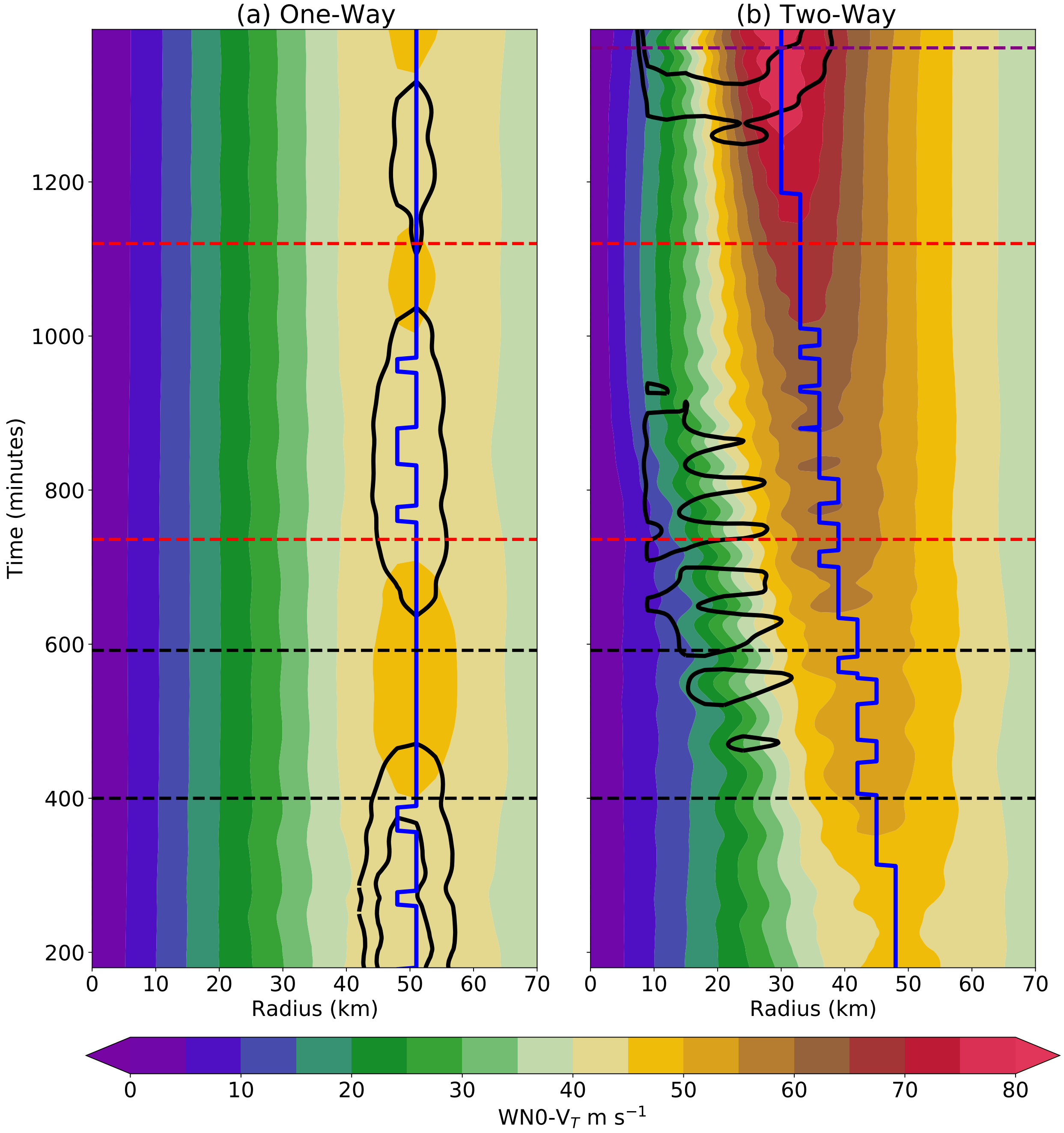

Figure 3.4: Similar as Fig. 3.3 but for the wavenumber 0 tangential wind (shading) and 2.5×10^{-7} and 5×10^{-7} (m^{-1} s^{-1}) wavenumber 2 PV (black contour). Blue line denotes the RMW.

s^{-1} when the PV asymmetries start to appear again. A close coupling between the intensifying mean tangential wind and PV, and a steadily enhanced boundary layer updraft suggests that the diabatic heating maintained by the boundary layer processes can continuously replenish PV generation in the free atmosphere (Figs. 3.3 and 3.4).

The radial vorticity gradient plot shows that the vorticity is mostly like a monopole for the entire analysis period from the one-way simulation result (Fig. 3.5a). On the other hand, the two-way experiment shows an appearance of a dipole pattern around 400 minutes when the positive radial voriticty locates mostly inside the 30 km and the negative radial vorticity gradient is around 40 km. There is an enhancement of the dipole radial vorticity gradient between 400 and 800 minutes, and the amplitude is weaker between 800 and 1100 minutes. The radial vorticity gradient becomes more intense and reaches to an amplitude over 4×10^{-7} ($m^{-1}s-1$) after 1200 minutes. The growth of the asymmetries has a close coupling with the radial vorticity gradient (Fig. 3.5). VRWs exist on the radial vorticity gradient, and their propagation acts to diminish the vorticity gradient by the vorticity mixing process. Figures 3.4 and 3.5 show an overall correspondence of the enhanced vorticity gradient and the wavenumber 2 amplitude.

Figure 3.6 shows the time evolution of the elliptical vortex in the SBL from 400 min to 592 min from the one-way model simulation. Similar to Kuo et al. (2016)'s finding, strong updrafts are at the major axis of the ellipse, collocated with high-speed boundary layer tangential wind. By performing a spectral analysis similar as Chapter 2's approach, the cyclonic rotation speed of the wavenumber 2 boundary layer updraft, tangential flow, and PV in the SWM are all 27.53 m s^{-1}, which takes 194 minutes for a complete rotation. This simple calculation is confirmed by Figure 3.6 where the 192 minutes evolution of boundary layer are displayed. The harmonic rotation between the boundary flow and the PV in the SWM suggests a close coupling between the deep convection and the PV structure.

Figure 3.7 shows the dynamic structure evolution in the shallow water model. The h field refers to the pressure field, which shows an elliptical eyewall shape and is similar to the boundary layer upward motion pattern shown in Fig. 4.7 as the boundary layer flow is organized by

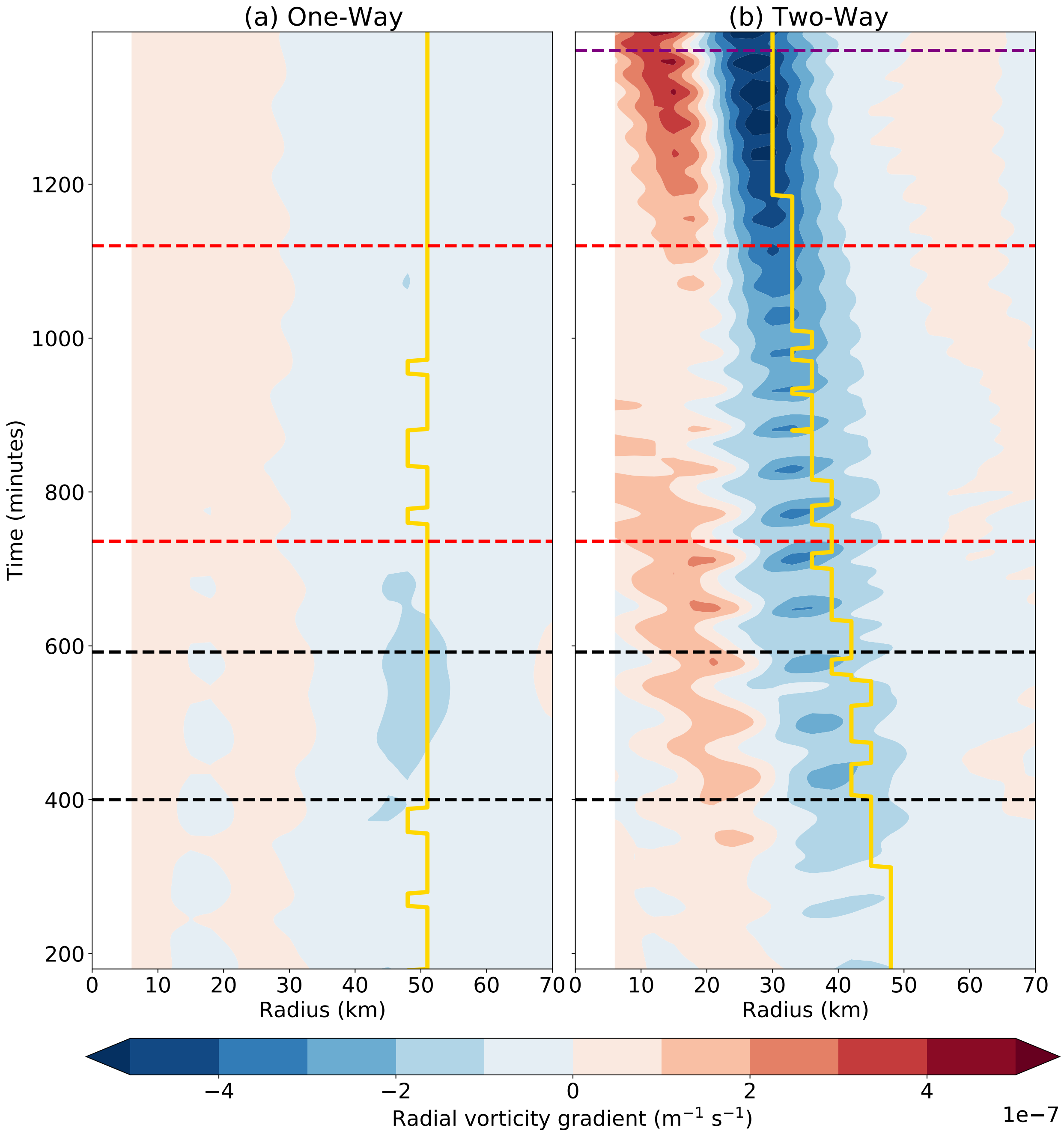

Figure 3.5: Similar as Fig. 3.3 but for the wavenumber 0 radial vorticity gradient (shading).

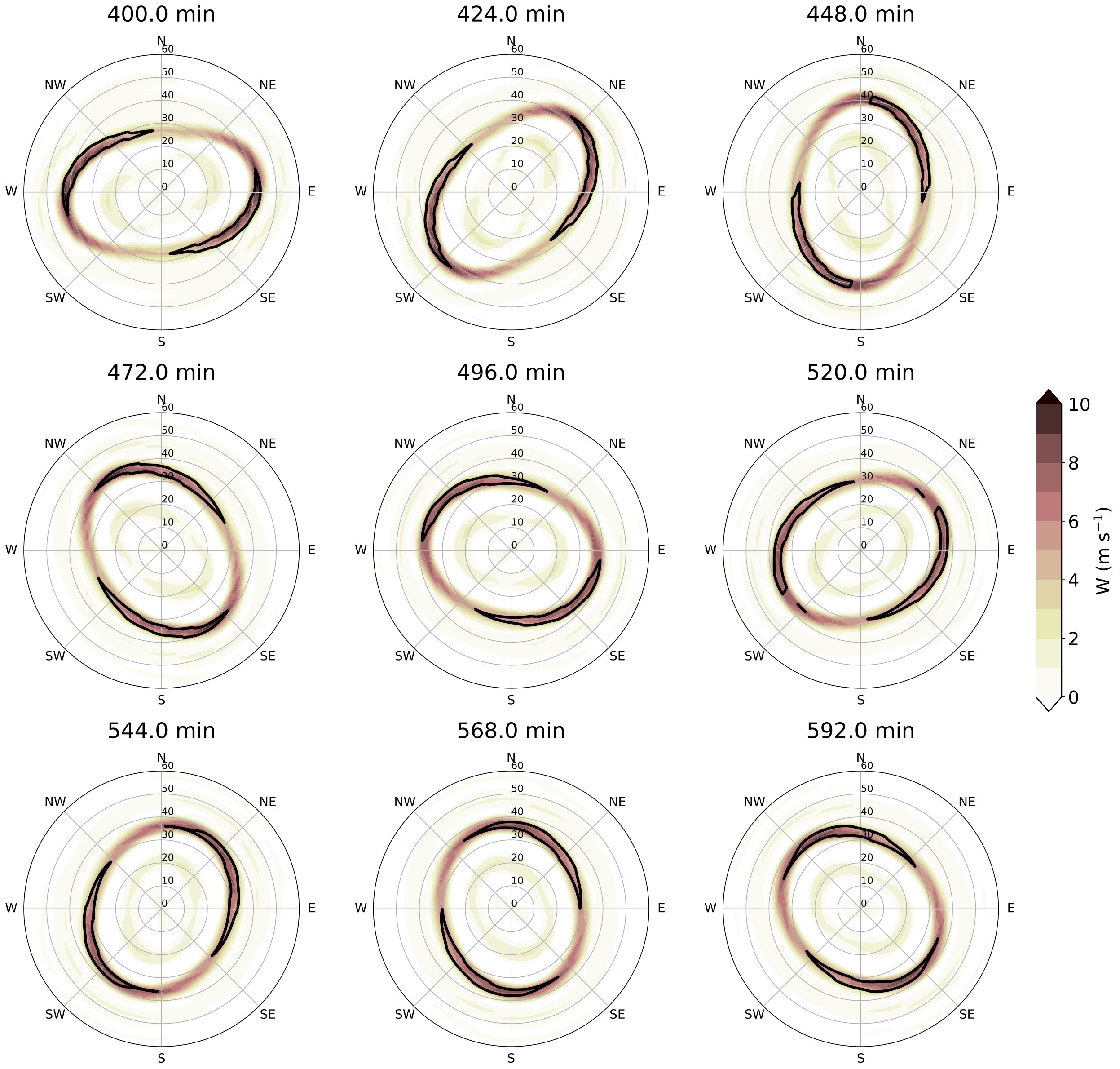

Figure 3.6: The 192 minutes evolution of boundary layer updraft (shading) and 65 m s^{-1} tangential wind (contour) from 400 min to 592 min in the one-way simulation. The interval between the panels is 24 minutes.

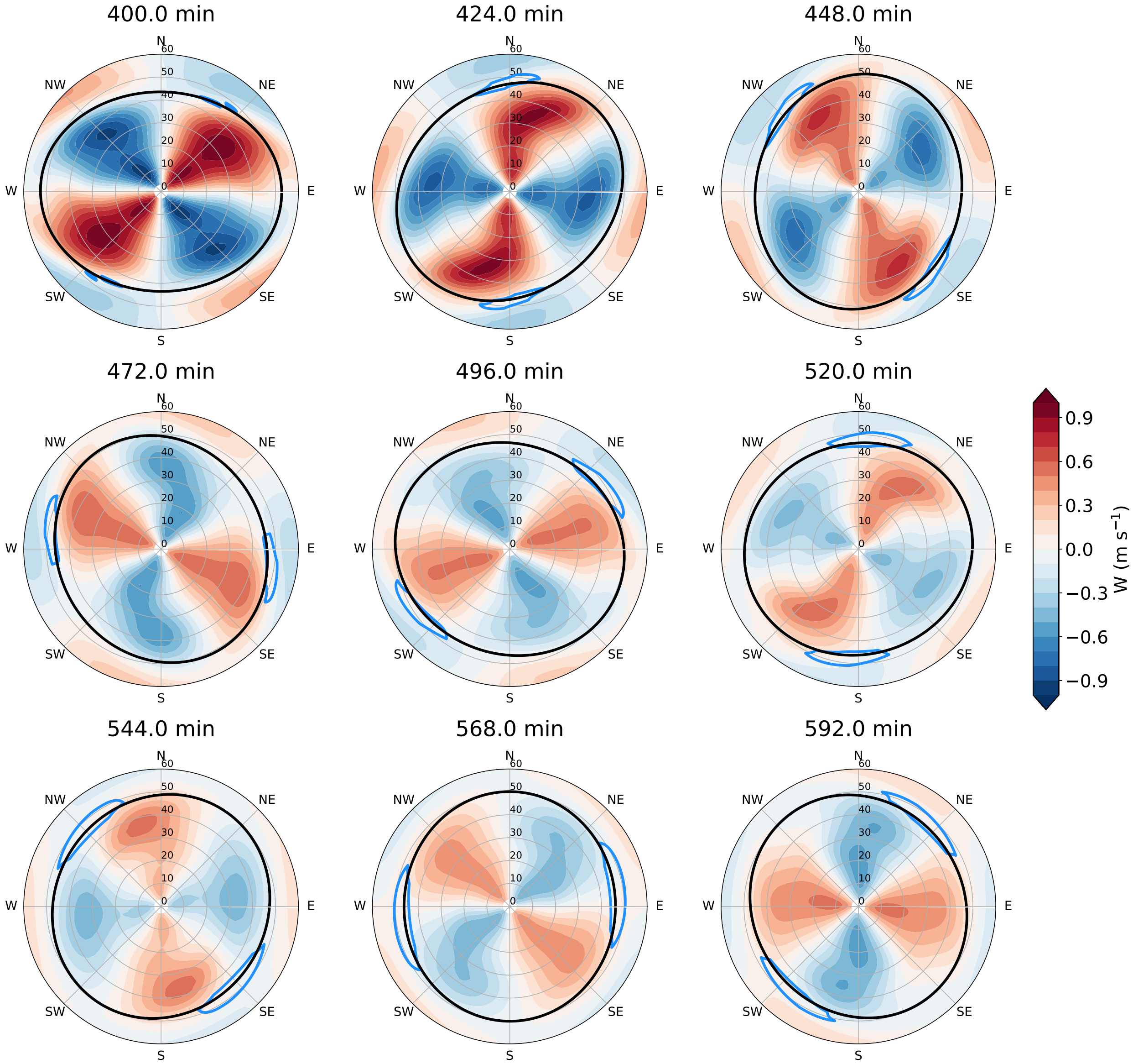

Figure 3.7: Similar as Fig. 3.4 but for the evolution of vertical motion (shading), 120 m SWM fluid deviation depth (black contour), and 48 m s^{-1} tangential wind (blue contour) from the one-way model results.

the pressure gradient force. The high-speed tangential wind is denoted by a blue contour, and has an opposite pattern compared to the boundary layer tangential wind. Kuo et al. (2016) also found a similar characteristic for the different tangential wind patterns between the boundary layer and the free atmosphere. They interpret the tangential wind at the minor axis of the ellipse through the tangential momentum equation neglecting the pressure gradient force term:

$$\frac{Dv}{Dt} = -\left(\frac{v}{r} + f\right) u \tag{3.20}$$

The radial inflow is largest at the major axis, which results in the strongest Dv/Dt located at the major axis. Largest Dv/Dt pushes downstream to the minor axis where the tangential jet maximum locates.

The magnitude of diagnostic vertical velocity in the SWM ranges from -1 to 1 m s^{-1}, which is way much weaker than the boundary layer vertical motion. The vertical velocity in the SWM has a dipole pattern but does not necessarily locate at the edge of the elliptical vortex. Differences in vertical velocity pattern between the SWM and SBL suggest that the boundary layer dynamics help with the enhanced reflectivity locates at the vertices, but not through the dynamics above the boundary layer.

Figure 3.8 shows the two-way model evolution. The upward motion in the boundary layer depicts an elliptical shape with maximum at the major axis at 400 min, evolves into a square at 496 min, and transitions back to an elliptical shape at 592 min. The boundary layer tangential wind collocates with the upward motion and rotate cyclonically together. The propagation speed of wavenumber 2 tangential and vertical motion in the boundary layer are both 23.06 m s^{-1} and the mean radius of maximum wind is at $\approx$ 42.7 km, which results in 194 minutes to complete a rotation. The rotation period is same as the one-way model result.

Figure 3.9 shows the upward motion, h, and 57 m s^{-1} tangential wind speed in the shallow water layer. The upward motion is not at the major axis, but instead, a $\pi/4$ phase ahead of the upward motion in the boundary layer. The upward motion collocates with the convergence field, and the vertical motion is about 2 m s^{-1} amplitude. Comparing the vertical motion in the

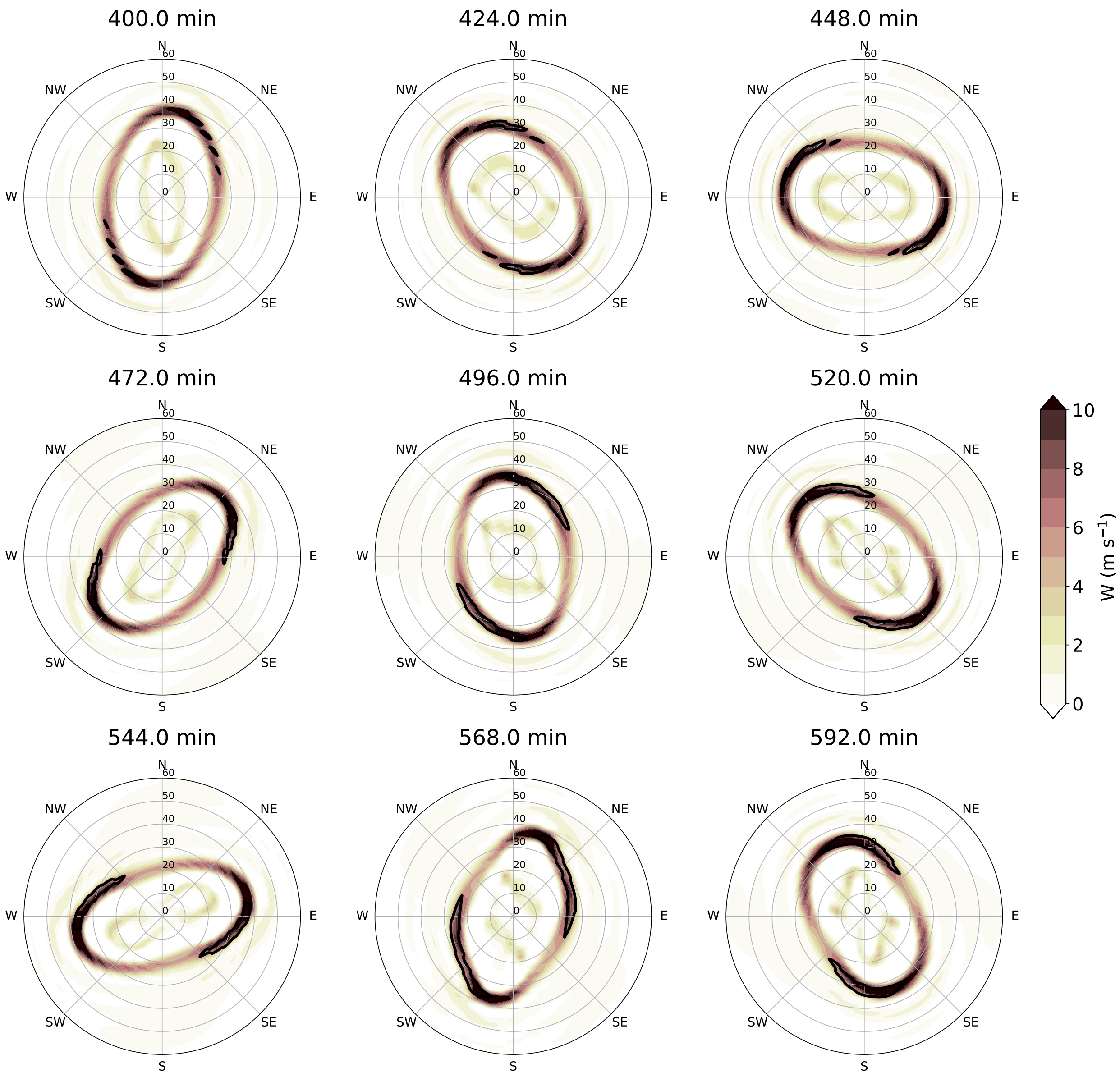

Figure 3.8: Similar as Fig. 3.6 but for the two-way model.

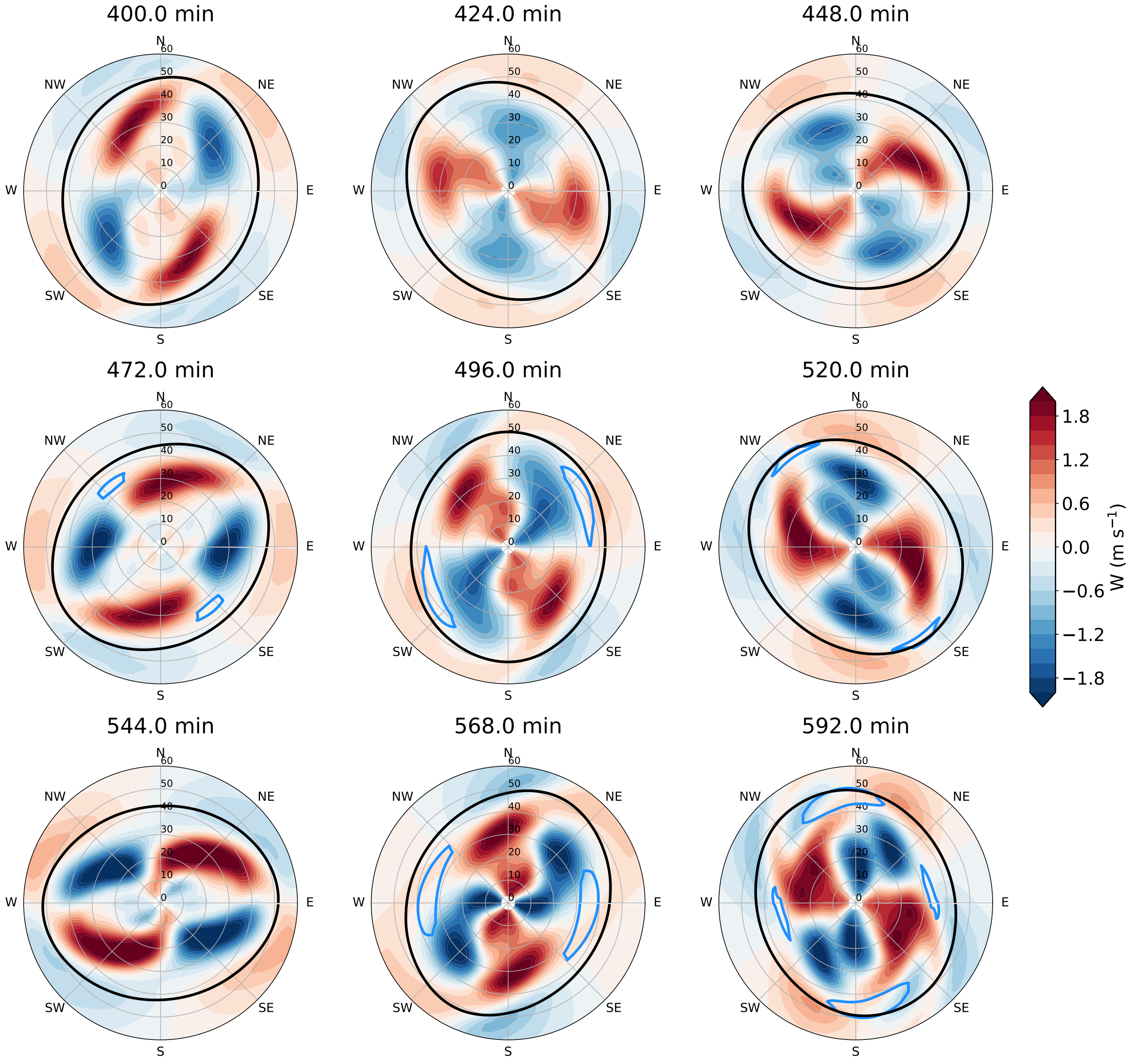

Figure 3.9: Similar as Fig. 3.7 but for the two-way model with 100 m SWM fluid deviation depth (black contour), and 57 m s^{-1} tangential wind (blue contour).

SWM to the vertical motion in the SBL, the SWM vertical motion is substantially weaker than the motion in the SBL, which suggests that the SWM maintains approximate gradient wind balance, and the agradient flow is weak.

Comparing the upward motion and the tangential wind pattern in the SWM to the SBL (Fig. 3.8), the enhanced tangential signal does not collocate with the strongest upward motion. During this period, the enhanced tangential wind signal are not always at the minor axis, and locates at the major axis at 520 min, which is different from the one-way model result.

The dynamical evolution in the boundary layer and the shallow water during the first period is accompanied by a development of PV ring, pulses of wavenumber 2 PV signal, and enhanced radial vorticity gradient (Figs 3.3, 3.4 and 3.5). The wavenumber 0 structure suggests an onset of the barotropic instability so the asymmetric evolution is expected and similar to other previous studies.

For the second period denoted in the time-radius diagrams, the vortex becomes more compact and the elliptical eyewall contracts to a smaller RMW compared to the first period. Figure 3.10 shows the evolution of the vertical velocity and tangential wind in the boundary layer. At 720 min, the maximum updraft and tangential wind are at the major axis. The elliptical shape evolves into a square shape at 832 min and becomes more circular at 1072 min with a over 10 m s^{-1} upward motion ring.

Figure 3.11 shows the PV evolution overlaid with the boundary layer updraft, capturing the period of the weakening radial vorticity gradient and the intensification. At 736 min, the elliptical shape has two PV patches with a magnitude of 3×10^{-6} $m^{-1}s^{-1}$ downstream of the major axis and hollow PV inside the eye. The patch of vorticity circles the vortex while the patch of high vorticity settles into the vortex center, accompanied by its associated trailing spiral bands of PV. At 1120 min, the nearly circular PV at the vortex center with a maximum of $3.6\times10^{-6}m^{-1}s^{-1}$. Because the boundary layer updraft continues to provide diabatic heating to help with the PV generation, so the total PV after mixing is larger than the total PV before mixing (at 736 minutes, Eq. 3.16). Meanwhile, the mean vortex continues to intensify. The vorticity mixing process has

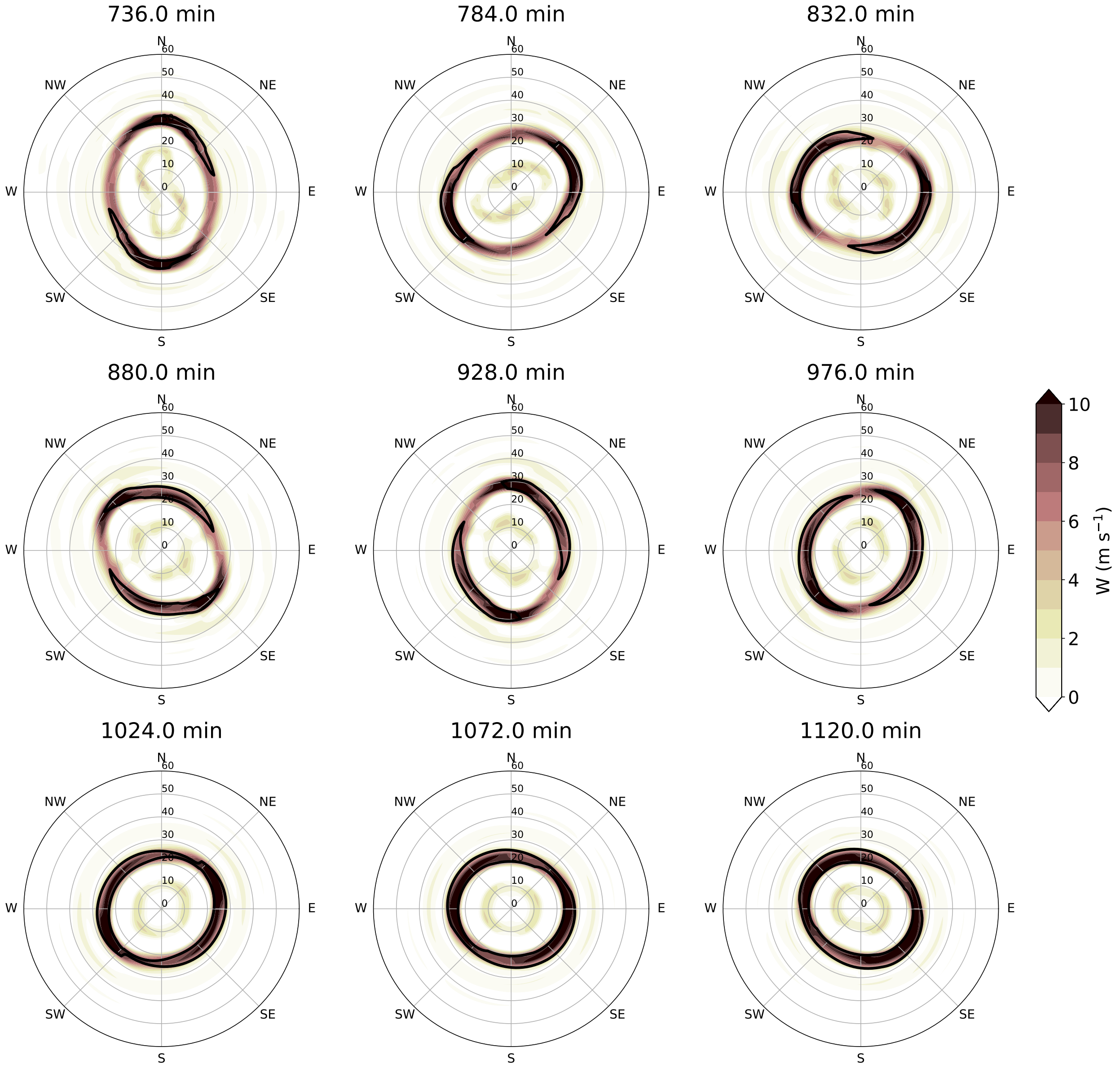

Figure 3.10: Similar as Fig. 3.8 but for the period from 736 to 1120 minutes in the two-way model and 80 m s^{-1} boundary layer tangential wind (black contour).

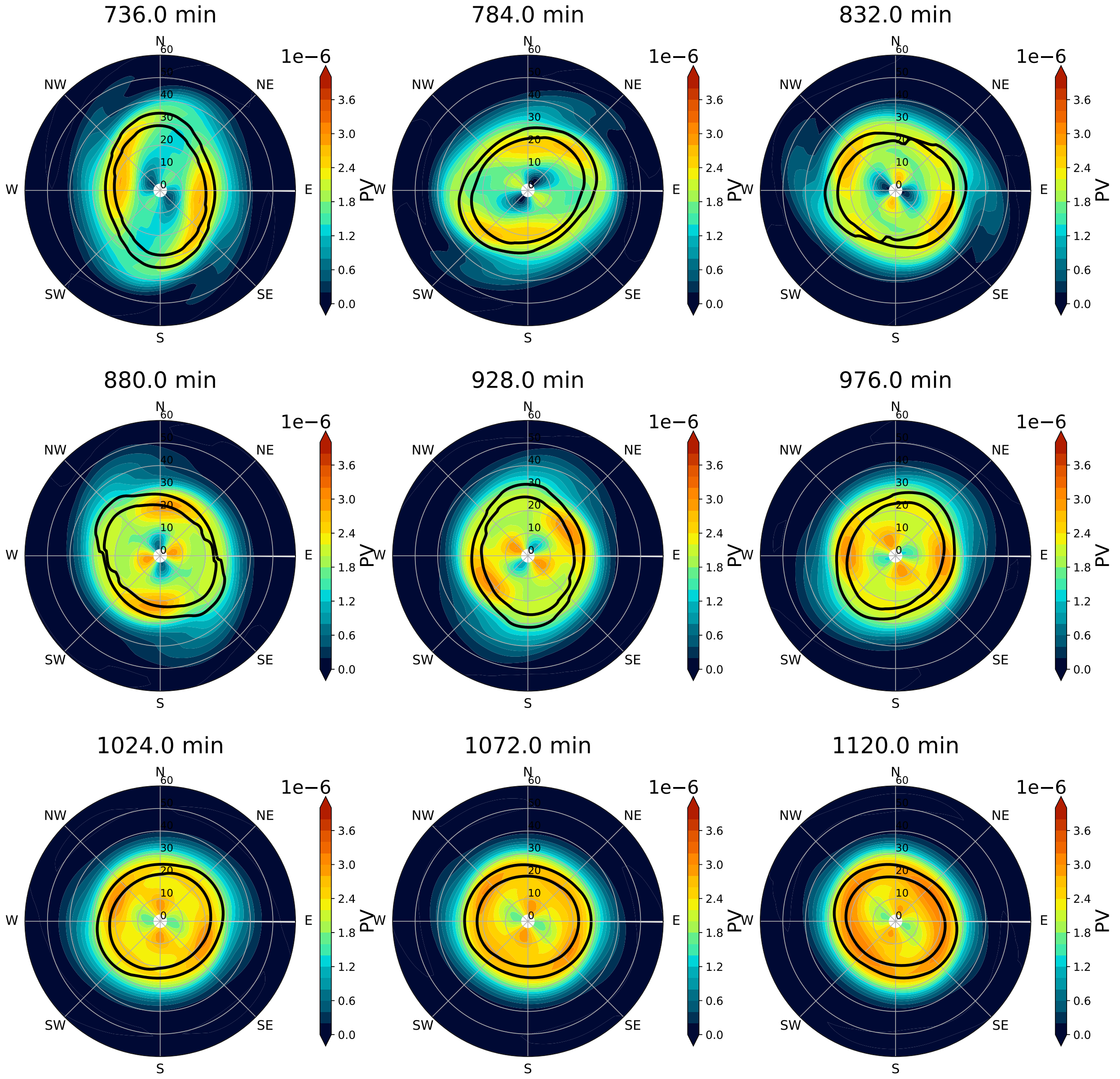

Figure 3.11: Similar as Fig. 3.10 but for the evolution of potential vorticity (shading) and 6 m s^{-1} boundary layer upward motion (black contour) in the two-way model.

been suggested to be a detrimental process in previous barotropic models. With the aid of deep updraft, the vortex was able to sustain and even intensify after the mixing process.

The evolution of rising asymmetries to axisymmetrization can be inferred from the wavenumber 0 PV structure and the radial vorticity gradient. Between 600 and 800 minutes, the wavenumber 0 PV structure with positive radial vorticity on the inner edge of the ring and negative radial vorticity on the outer edge of the ring support the growth of two vorticity waves and propagation (Figs. 3.3 and 3.5).

The wavenumber 0 tangential wind is steadily intensify with minimal asymmetries after 1120 min (Fig. 3.4. The wavenumber 2 PV signal reappears around 1250 min, and the intensification rate starts to slow down. Figure 3.12 shows a snapshot of the PV and boundary layer updraft at 1338 min. The vortex evolves to an elliptical shape again. The PV ring with two PV maximum patches over $4.8\times10^{-6}\mathrm{m}^{-1}\mathrm{s}^{-1}$ collocated with the strong updraft ring. The evolution of the dissipation of asymmetries and intensification of the mean vortex, and followed by the regeneration of asymmetries and the growth of a PV ring suggests that the diabatic heating provided by the boundary layer dynamics is important to TC intensification.

3.4 Discussion, conclusion and future work

In this study, the relationship between VRWs and the polygonal precipitation structure is explored through a simple modeling framework. A two-layer model consisting of a shallow water fluid on top of a slab boundary layer is used to understand the dynamical relationship. The model maintains approximate gradient wind balance in the free atmospheric layer and parameterizes the diabatic heating produced by convection from the vertical motion out of the boundary layer. In order to enable the two-way interaction, we parameterize the diabatic heating effect by the boundary layer vertical motion which can feed back to the free atmosphere, similar to the framework described in Schubert et al. (2016). Unlike previous studies with a prescribed heating profile (Rozoff et al. 2009; Hendricks et al. 2014; Schubert et al. 2016), the vertical motion in the boundary layer can develop freely, so the location and intensity of diabatic heating are changing at each time step, which is a more realistic heating distribution. We

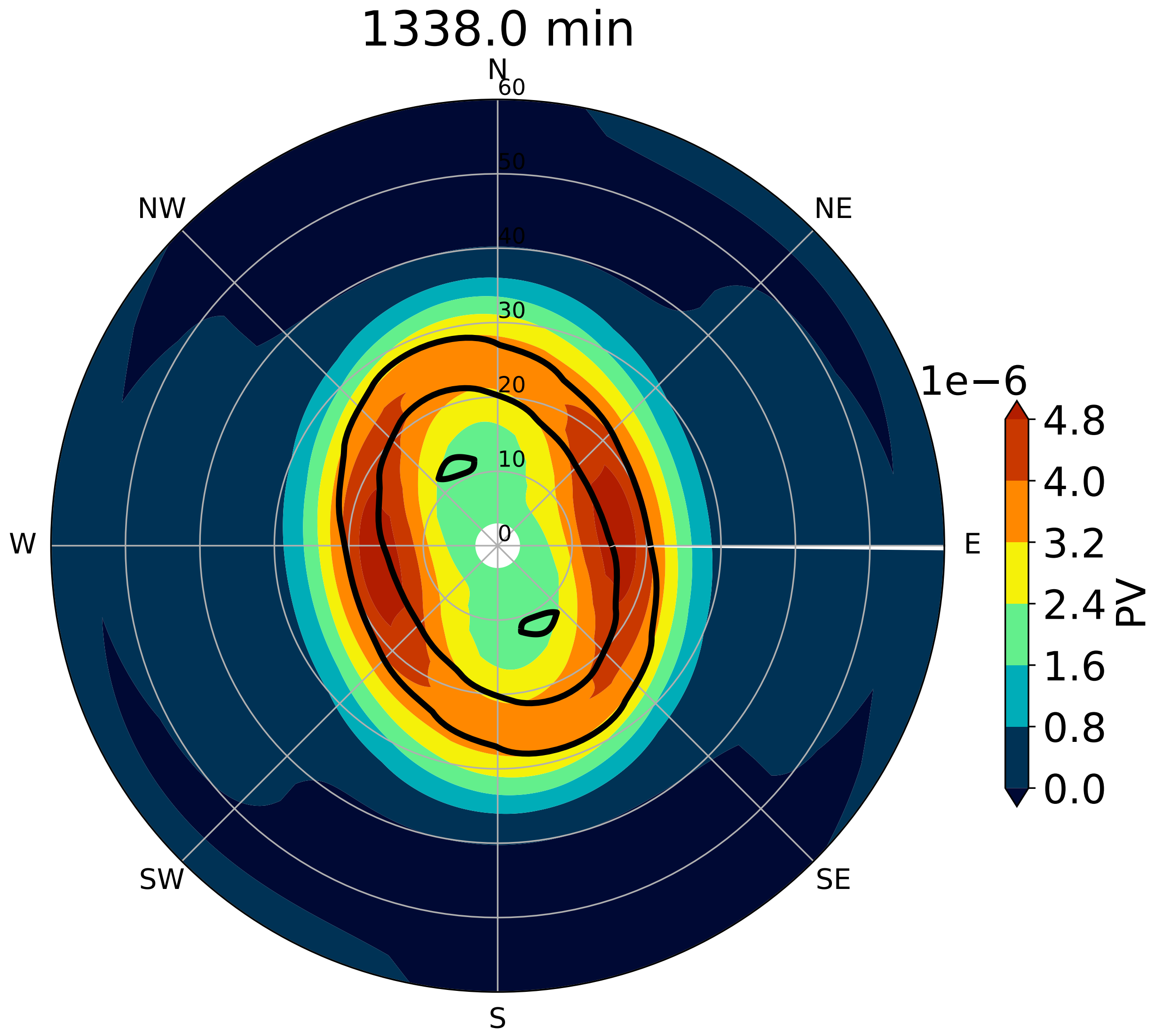

Figure 3.12: Similar as Fig. 3.11 but at 1338 minutes.

conduct two experiments: one-way and two-way. These two experiments both use an approximate Rankine vortex with an added wavenumber 2 perturbation as the initial condition.

Results from the one-way experiment shows that the boundary layer updraft locates at the major axis of the ellipse, whereas the vertical velocity in the shallow water layer does not possess any elliptical shape. The vertical velocity in the boundary layer rotates cyclonically, and propagates harmonically with the PV signal in the free atmosphere. This result confirms Kuo et al. (2016)'s hypothesis and findings that the VRW in the free atmosphere can organize the updrafts in the SBL, so deep convection we see in nature is likely to locate at the polygonal vertices.

Our one-way and two-way experiments further show that the vertical velocity derived from the shallow water layer is about 1 order of magnitude smaller than the vertical velocity derived from the boundary layer. The SWM has a maximum amplitude only up to 2 m s^{-1} and does not locate at the ellipse, whereas the vertical motion in the SBL can be over 10 m s^{-1} and is associated with the elliptical eyewall shape. A much weaker vertical motion in the SWM suggests that the convergence induced by the agradient flow aloft is weak as compared to the convergence produced by frictional imbalance in the TCBL. The finding provides a new insight that the convergence in the free atmosphere has little direct impact on the location of deep convection even though our model allows the development of the agradient flow aloft.

Results also show that the VRW theory is reasonable to describe the wavenumber 2 propagation in the one-way model simulation. Our one-way model presents the close coupling between the convection and the polygonal vertices, and is similar to Kuo et al. (2016)'s finding. Similar results obtained from two different model setups suggest that a nondivergent barotropic model coupling with a SBL could be sufficient enough to capture the essential dynamics, and might be one of the simplest model frameworks to understand VRWs and their associated convection.

However, further intensification of the mean vortex cannot occur in the one-way experiment; whereas results from the two-way experiment show that diabatic heating driven by the boundary layer processes can contribute to the growth of a PV ring and the mean vortex intensification. The results are consistent with Rozoff et al. (2009) and Hendricks et al. (2014)'s findings that the diabatic heating can produce a strengthening PV ring, and an intensification can occur even during barotropic instability. Hendricks et al. (2014)'s sensitivity experiment suggests the prescribed heating should be close to the center of the storm in order to intensify rapidly. Our model does not prescribe the diabatic heating location and intensity, but the free atmospheric flow organizes the heating close to the RMW through TCBL processes. The location of the heating is coupled with the contraction of the RMW and the building of the PV ring. The boundary layer updraft can develop freely and feed the diabatic heating to the free atmosphere, so the vortex keeps contracting and intensifying. This evolution of the heating, RMW, and PV ring are broadly consistent with Martinez et al. (2019)'s observational study of Hurricane Patricia's (2016) rapid intensification.

The two-way experiment shows that nonlinear interactions modulate the intensification rate, the growth and decay of asymmetries, the growth and the breakdown of the PV ring throughout different stages of vortex evolution. Our result confirms Chapter 2's finding that intensification of the mean vortex can occur even during barotropic instability, and shows a similar evolution to Chapter 2's observations and analyses, including 1) growing high-order asymmetries accompanying by a reverse sign of the mean radial vorticity gradient, 2) axisymmetrization of asymmetries and a weakening mean radial vorticity gradient, and 3) a close coupling between the convection and polygonal vertices. The similarity between our model results and the observations suggests that the presented modeling framework with two-way interactions could be a simplified framework approach to study TC intensification under the presence of evolving asymmetries in the real atmosphere.

Future work should consider more sensitivity experiments to see what parameters would disrupt the intensification or favor the intensification, and also sensitivity tests on initializing different wave perturbation for the initial condition to see if the deep convection locates at the vertices, initializing the PV ring with different initial condition to see how different size of PV ring impacts the intensification and asymmetries evolution. Other modifications are including changing the heating rate, length of Rossby deformation, boundary layer depth, and free atmosphere depth to obtain a insight into the interactions for the interaction between the free atmosphere and the boundary layer.

Chapter 4

Three-Dimensional Variational Multi-Doppler Wind Retrieval over complex terrain [2]

4.1 Introduction

The vertical transport of water vapor and air plays a critical role in the weather and climate system. However, vertical motion (w) remains one of the most poorly observed wind components and is difficult to predict. Over complex terrain, orographically-induced air flow plays an important role in modulating the vertical motion and physical processes of weather systems. The intensity of precipitation can be enhanced and the structure of cloud systems can be altered by the interaction between clouds and topography. When a moist airmass moves over terrain, multiple mechanisms can play a role in modulating the clouds and precipitation (Houze 2012). These interactions can lead to extreme rainfall (Chien and Kuo 2011) and intense convective storms (Zipser et al. 2006).

Doppler radar observations present an opportunity to understand airflow associated with orographic interactions and the key ingredients impacting the intensity and duration of severe weather. Multiple-Doppler radar observations can be used to reconstruct a full three-dimensional wind field (Ray et al. 1979), but the accuracy of w remains challenging, especially when the precipitating system is over a mountainous area. The retrieved w is mainly dependent on the mass continuity equation when the radar beams are at low-elevation angles. The mass continuity equation enforces the mass-weighted vertical flow to be physically consistent with the divergence of the mass-weighted horizontal flow. Accurate representation of the boundary conditions on w is required to retrieve a reasonable three-dimensional wind field and to further

---

[2] The results outlined in Chapter 4 have been submitted to the *Journal of Atmospheric and Oceanic Technology.*

study storm dynamics. In this study, we implement boundary conditions at the terrain height to represent the topographic forcing and surface impermeability in three-dimensional variational data assimilation (3DVAR) multi-Doppler radar software to recover the wind field over complex terrain.

Different sources of uncertainties in the three-dimensional wind reconstruction include instrument effects, sampling effects, and algorithm effects. Hildebrand et al. (1994) shows that the instrument effects can contribute to errors of up to 1-2 m s^{-1} caused by the radar processor design and measurement technique. Sampling effects include data spacing and density impacted by the geometry of dual or multi-radar beams and beam blockage by terrain, temporal evolution of weather phenomena, and data collection time span (Hildebrand and Mueller 1985; Cha and Bell 2021). Oue et al. (2019) uses a radar emulator to investigate the quality of vertical wind retrieval caused by observational error sources. They show that the volume coverage pattern (VCP) elevation strategy and sampling time can have a significant impact on the retrieved vertical velocity, and using rapid-scan radars to shorten the data collection period can substantially improve the quality. Algorithm effects include the interpolation and smoothing techniques used to map the radar polar grid to a common Cartesian coordinate (Collis et al. 2010), hydrometeor fall speed estimates (Steiner 1991), and other algorithm assumptions (e.g. mass continuity integration, Matejka and Bartels (1998)).

Variational techniques have been used widely for multi-Doppler retrievals (Gamache et al. 1995; Gao et al. 1999, 2004; Potvin et al. 2012; Bell et al. 2012a; North et al. 2017). The 3DVAR approach solves for the optimal wind field by minimizing a cost function including different types of observations, the mass conservation equation, and some forms of low-pass filters with prescribed weak or strong constraints. This approach can mitigate retrieval instabilities in data sparse areas and along the radar baseline. Most 3DVAR approaches have been developed for retrievals over a flat surface, but the retrieval over complex terrain requires consideration of the topographic forcing and impermeability at the terrain height. Georgis et al. (2000) was one of the first studies that developed a variational approach to take the orographic effects into account for multi-Doppler radar analysis. Their approach uses a first guess of the vertical velocity obtained from the integration of the mass continuity equation, and solves the vertical wind iteratively until reaching to a convergence. Chong and Cosma (2000) improved the variational MUltiple-Doppler Synthesis and Continuity Adjustment Technique (MUSCAT; Bousquet and Chong (1998)) by implementing the capability to resolve the wind flow over complex terrain. Chong et al. (2000) further integrated the above two approaches and presented an improved multiple-Doppler analysis method to recover the wind field over mountainous regions in real-time, and the wind flow along the radar baseline is able to be partially recovered by using a low-pass filter.

Liou and Chang (2009) developed a variational multiple-Doppler radar three-dimensional wind synthesis method over flat terrain, and the accuracy of vertical velocity retrieval was improved by including the vertical vorticity equation and reducing the assumption of prescribed vertical velocities at the data boundary. Liou et al. (2012) further advanced the technique by employing the immersed boundary method (IBM) using a ghost cell method to recover the wind field above the terrain which takes the topographic forcing into account (Tseng and Ferziger 2003). The IBM approach can provide realistic topographic forcing for a standard Cartesian grid without converting to a terrain-following coordinate system.

The SAMURAI analysis technique uses a finite element approach with a series of overlapping cubic B-spline basis, which has some benefits compared to a conventional grid-point representation (Bell et al. 2012a; Foerster et al. 2014). The finite element representation of functions can yield a scale-controlled analysis with analytic spatial derivatives. In SAMURAI, observations do not need to be interpolated to a Cartesian grid, but can be used in the variational minimization in their native locations. This reduces one of the potential interpolation errors in the analysis. Additionally, constraints on the spatial gradients can be treated as pseudo-observations that are implicitly integrated during the cost function minimization rather than explicitly integrated. First-order spatial derivative constraints can be obtained from physical equations, such as the mass continuity equation and/or the momentum equations (Foerster et al. 2014). The finite element formulation allows for the specification of these derivative constraints as pseudo-observations at any point and space.

The current study improves the SAMURAI technique by adding retrieval capability over complex terrain. We implement the IBM method as pseudo-observations which allows for the boundary conditions at any specified terrain height with adjustable observational errors. Spatial derivatives are analytic therefore avoiding the need for the ghost cell approach used in finite difference methods. The outline of the paper is as follows. Section 4.2 describes the details and the formulation of the 3DVAR approach over the complex terrain. The accuracy of the immersed boundary solver is examined by a series of Observing System Simulation Experiments (OSSEs) using simulated data from Typhoon Chanthu (2021) that produced heavy rainfall over complex topography in northern Taiwan. Section 4.3 presents the dataset and sensitivity experimental setup. Section 4.4 explores the performance of the newly developed method, and the sensitivity tests of variant strength of terrain forcing constraint at the boundary, the resolution and details of complex terrain slope, the contribution of vertical wind retrieval from the mass continuity and terrain forcing, and the grid spacing and Gaussian recursive filter setting. Section 4.5 demonstrates the applicability of the wind retrieval over complex terrain using real radar data from Typhoon Chanthu (2021). Section 5 summarizes and discusses the results.

4.2 Methodology

4.2.1 SAMURAI

SAMURAI refers to Spline Analysis at Mesoscale Utilizing Radar and Aircraft Instrumentation (Bell et al. 2012a). SAMURAI uses a set of cubic B-spline basis that are continuous and differentiable to the third-order derivative. Combining a set of spline functions allows to form the shape of any function and still be differentiable. Using the spline basis for the underlying representation of the atmospheric structure can specify pseudo-observations of spatial gradients.

The nodal spacing determines the minimum feature size resolved by the function. The finite element approach in SAMURAI allows for a flexible nodal spacing and spatial gradients to be specified at any point and space. The pseudo-observations of spatial gradients are then integrated during the cost function minimization along with the observations and background. The cost function is an incremental form $J(\hat{\mathbf{x}})$ that uses observations, observation errors, background state estimates, and background state errors as weights:

$$J(\hat{\mathbf{x}}) = \frac{1}{2}\hat{\mathbf{x}}^{\mathbf{T}}\hat{\mathbf{x}} + \frac{1}{2}(\mathbf{HC}\hat{\mathbf{x}} - d)^{T}\mathbf{R}^{-1}(\mathbf{HC}\hat{\mathbf{x}} - d) \tag{4.1}$$

where $\mathbf{H}$ represents the linearized observation operator, $\mathbf{C}$ represents the square root of the background error covariance matrix, $\mathbf{R}$ represents the observation error covariance matrix, and d represents the difference between the observations and the nonlinear observation operator applied to the background state estimate. The minimized cost function error is the most likely atmospheric state at the analysis time based on the input data and specified errors. A nonlinear Conjugate Gradient (NCG) method was used to minimize the cost function (Gao et al. 2004), which requires the computational cost to evaluate the gradient and perform a line search during each iteration until it reaches to convergence. Dennis et al. (2022) improved the optimization solver performance by implementing a Truncated Newton (TN) solver, code optimization, and porting SAMURAI to GPU environment, which had a profound impact on overall execution time speedup. More details for the improvement can be found Dennis et al. (2022).

SAMURAI has three spatial filters that can act as smoothing the analysis and spreading information from the observations throughout the domain, including Fourier spectral filter, Spline cutoff, and Gaussian recursive filter. The Fourier spectral filter is mainly used for removing high-wavenumber features in the spectral domain and axisymmetric type of analysis. The spline cutoff is implemented as a third derivative constraint on the cubic B-spline basis during the spline transform (Ooyama 2002b). The Gaussian recursive filter is a Gaussian low-pass filter through an efficient recursive operator (Purser et al. 2003). Smaller filter lengths retain more detail, but they may fit noise. Larger filter lengths smooth more and lose detail. These filters can be used individually or be combined to produce different responses. Using an appropriate filter type and length for the data distribution is very important to obtain the desired physical scales of interest analysis.

In this study, we use a combination of the spline-cutoff filter with 2 nodal points in the horizontal and the Gaussian recursive filter with 4 nodal points in the horizontal and 2 nodal points in the vertical. The sensitivity of the Gaussian recursive filter setting will be carried out in section 4.4, but the sensitivity of the Fourier filter and the spline cutoff setting are omitted in this study.

4.2.2 The immersed boundary method

Urban and mountainous environments are generally associated with steep slopes and complex geometries. The IBM method enables flows with complex terrain to be simulated on their native spacing without conforming to any coordinate system, which retains topography with high-order boundary representations. Therefore, winds induced by terrain forcing can be realistically resolved.

IBM has been implemented into the WRF model (Lundquist et al. 2010), and a observational wind retrieval technique Wind Synthesis System using Doppler Measurements (WISDDOM, Liou et al. (2012)). Previous studies have adopted a finite-difference approach, where the body force term is applied at ghost cells located inside the terrain. This method is able to handle rigid boundaries and produces a sharp representation of the fluid solid interface. In SAMURAI, the ghost cell approach can be avoided due to two primary implementations: First, SAMURAI uses the finite element approach, so that the terrain boundary nodal does not have to be at any specific computational nodes and the boundary spatial derivatives can be at their native location. Second, SAMURAI uses a set of overlapping cubic-b splines which are differentiable to the third-order derivative, so the boundary condition can be enforced at the terrain height rather than a traditional ghost cell.

Two boundary conditions are implemented into SAMURAI, following Liou et al. (2012)'s method:

$$
\begin{aligned}
\frac{\partial u}{\partial n} = 0 = \nabla u \cdot n &= \frac{-(\frac{\partial h}{\partial x})}{\sqrt{1+(\frac{\partial h}{\partial x})^2+(\frac{\partial h}{\partial y})^2}}\frac{\partial u}{\partial x} + \frac{-(\frac{\partial h}{\partial y})}{\sqrt{1+(\frac{\partial h}{\partial x})^2+(\frac{\partial h}{\partial y})^2}}\frac{\partial u}{\partial y} + \frac{1}{\sqrt{1+(\frac{\partial h}{\partial x})^2+(\frac{\partial h}{\partial y})^2}}\frac{\partial u}{\partial z} \\
\frac{\partial v}{\partial n} = 0 = \nabla v \cdot n &= \frac{-(\frac{\partial h}{\partial x})}{\sqrt{1+(\frac{\partial h}{\partial x})^2+(\frac{\partial h}{\partial y})^2}}\frac{\partial v}{\partial x} + \frac{-(\frac{\partial h}{\partial y})}{\sqrt{1+(\frac{\partial h}{\partial x})^2+(\frac{\partial h}{\partial y})^2}}\frac{\partial v}{\partial y} + \frac{1}{\sqrt{1+(\frac{\partial h}{\partial x})^2+(\frac{\partial h}{\partial y})^2}}\frac{\partial v}{\partial z}
\end{aligned}
\tag{4.2}
$$

$$
w = u\frac{\partial h}{\partial x} + v\frac{\partial h}{\partial y} \tag{4.3}
$$

where n is the unit vector perpendicular to the boundary, u is the zonal wind, v is the meridional wind, w is the vertical wind, and h denotes the terrain height. The Neumann boundary condition is applied to u and v, and the Dirichlet boundary condition is used for w. The Neumann boundary ensures that the total flux of mass across the boundary should be set to be zero, so the mass flux cannot penetrate the terrain. The Dirichlet boundary ensures that the vertical velocity at the terrain height is induced by the horizontal wind u and v, so the topographic forcing is considered here.

4.3 Data and Sensitivity experimental setup

4.3.1 Typhoon Chanthu (2021)

Figure 4.1a shows Typhoon Chanthu's track and intensity. The maximum wind speed of Chanthu according to the Japan Meteorological Agency (JMA) was 115 kt (59 m s^{-1}) when Chanthu was northeast of Luzon. Although Chanthu underwent a weakening trend after peak intensity, the radar composite reflectivity shows the eyewall convection was still intense with over 50 dBZ at 05:30 UTC 12 September (Fig. 4.1c). The associated rainband with 35-40 dBZ made landfall in northern Taiwan. The spiral rainband was oriented mostly perpendicular to the mountain slope, which caused an enhanced rainfall parallel to the ridge. Figure 4.1b shows the 24-h rainfall accumulation from 08 UTC 12 September to 08 UTC 13 September. A band of enhanced precipitation parallel to the snow mountain ridge was recorded with a maximum of over 200 mm. Interestingly, the minimum rainfall over the Central mountain was only 20-30 mm. The variation in rainfall accumulation and pattern suggests that topography plays a salient role in modulating the amount of rainfall in addition to the typhoon circulation. The orographic widespread precipitation and strong wind speeds were in a region captured by the Wufenshen (RCWF) and Shulin (RCSL) radar observations under an adequate dual Doppler geometry (Table 4.1). Therefore, Typhoon Chanthu is selected to be the case to test the improved technique (Table 4.1).

4.3.2 Dataset

An observing system simulation experiment (OSSE) is conducted for Typhoon Chanthu on 12 September 2021 when the typhoon rainband moved onshore to the northern Taiwan and produced more than 50 mm within an hour in a mountainous region. OSSE studies are generally used to assess the impacts of operational observing systems on observation based value-added products and weather forecasts. The WRF simulation provides kinematic and thermodynamic variables with a physical understanding of orographic effects on precipitating clouds and wind flow.

The WRF simulation uses version 4.1.3 (Skamarock 2021). The domains are configured as fixed triple-nested domains with two-way interaction for the second and third domains. The outermost domain has a horizontal grid spacing of 9 km, 3 km for the second domain, and the inner-most domain has a resolution of 1 km. The innermost domain has a horizontal grid spacing of 1 km and 51 σ-layers in the vertical, initialized from the initial and boundary conditions provided by the 3-km simulation. The horizontal resolution of WRF terrain height data is 30 arc seconds, which is approximately 1 km horizontally with an averaged slope of 6E-2 (∇h, unitless), and is available at each grid point. The WRF simulation native output is in the pseudo-pressure coordinate, so the vertical grid is stretched in physical space. The minimum vertical grid spacing in the WRF grid is $\Delta z_{min} \approx 8.47$ m and occurs at the peak of the hill, and the

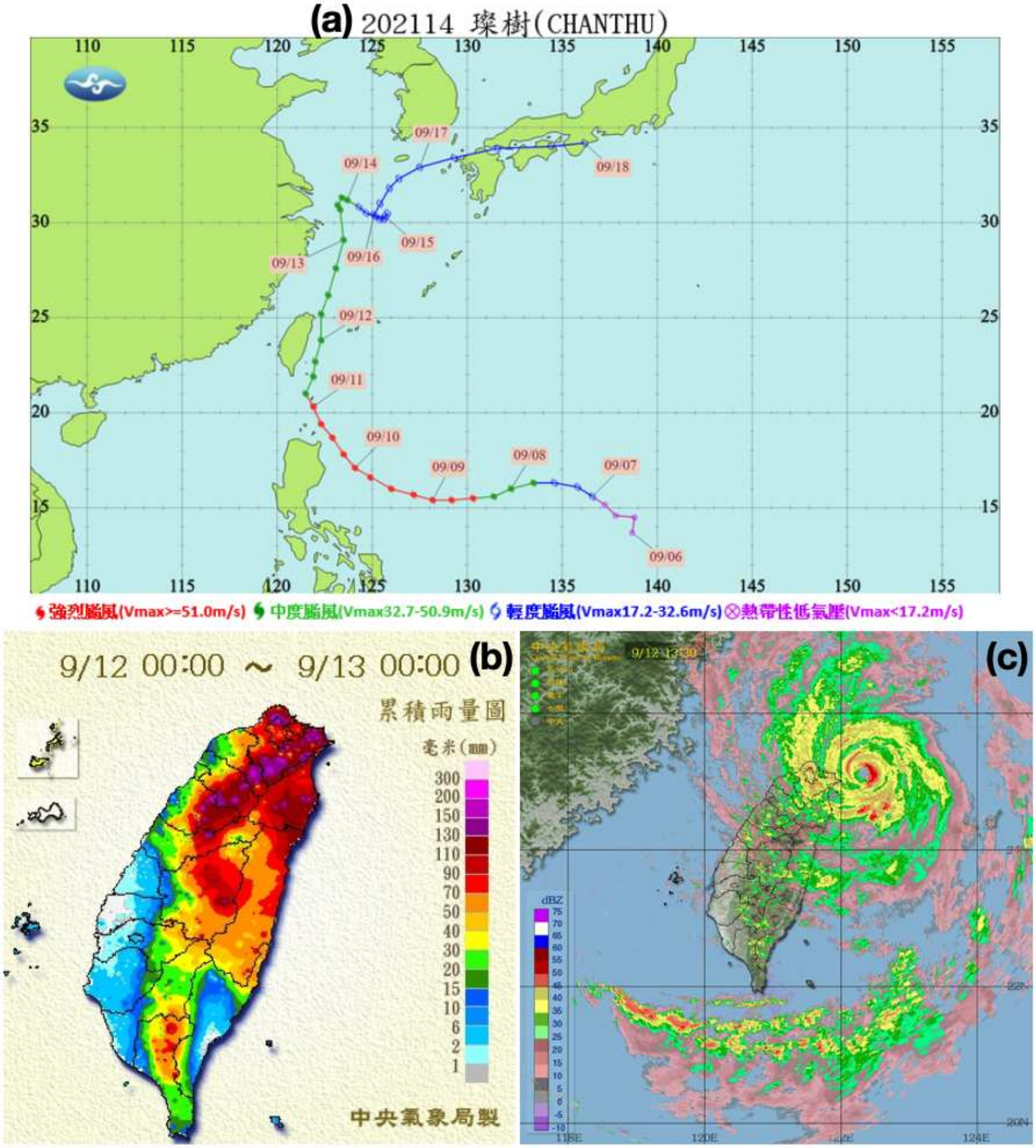

Figure 4.1: (a) Typhoon Chanthu's track and intensity. (b) 24-h rainfall accumulation from 08 UTC 12 September to 08 UTC 13 September. Time shown in the plot is in LST. (c) The composite radar reflectivity at 0530 UTC 12 September. All the figures were derived from the Central Weather Bureau Typhoon Database.

maximum vertical grid spacing is ≈ 20530.44 m at the domain top. The 1-km simulation was initialized after running the first and second domains for 3 hours. The innermost domain is set up to cover the northern part of Taiwan when Typhoon Chanthu's rainband interacted with the topography.

Three OSSE model datasets were generated and tested in the following order:

1. We produce the set of simulation data with known three-dimensional wind field (u, v, w), temperature, water vapor mixing ratio, dry air density, moist air density, and reflectivity data at WRF native coordinates. Data were extracted from the simulation and fed into SAMURAI with an observational error of 1 with the unit corresponding to the variables.

2. We use a radar simulator to resample the WRF-generated field and produce the volume coverage pattern (VCP) of a dual-Doppler radar system with radar measurements at WRF grid coordinates (Table 4.1).

3. We produce radar observables (reflectivity and Doppler velocity) at radar coordinates with more realistic radar characteristics.

Since the WRF simulation is on a sigma coordinate and the filtering length and the actual resolving scale are expected to be slightly different from the SAMURAI-Terrain output, the sigma-level output of the innermost WRF domain at 05:30:02 UTC 12 September snapshot was loaded to SAMURAI-Terrain with a magnitude of 1E-3 terrain boundary error (unitless). The sampling time for the radar VCP and the storm evolution are not considered in this study because we focus on the impact of complex terrain on wind retrieval. This first dataset is treated as the "truth" to compare against other sensitivity tests (Table 4.2).

The WRF output is used as an input to the Cloud resolving Model Radar SIMulator (CR-SIM, Oue et al. (2020)) to simulate equivalent radar reflectivity factor (Z_{hh}) and Doppler velocity (V_d) at the model grid to produce the second dataset. CR-SIM is a radar simulator that emulates multi-wavelength, zenith-pointing, and scanning radar observables from high-resolution cloud-resolving models. CR-SIM can convert the model variables into the form of radar and lidar observables using the same microphysics scheme, which can enable the direct comparison between numerical weather model output and radar observations. The simulated radar observables take the sampling strategy into account so that we are able to assess errors caused by sampling and uncertainties from the multi-Doppler wind retrievals, and ultimately find an optimized radar sampling strategy. The purpose of evaluating this dataset against the truth is to investigate the Doppler errors when there is no direct vertical wind observations. The third dataset is produced by projecting the second dataset to the radar polar coordinates based on a specified VCP provided in Table 4.1. This is evaluated against the first and second dataset to investigate the radar geometry and sampling errors. One caveat is that the dataset described above does not consider any beam blockage effect, which should be addressed in future work.

Figure 4.2 shows the “true” fields of reflectivity and vertical velocity, which are used to illustrate the retrieval performance for the sensitivity tests. The white area in the horizontal cross section at 1 km (Fig. 4.2a and b) is due to terrain (Fig. 4.2c). In order to objectively select an area of interest under reasonable radar beam geometry and appropriate spatial resolution, the dual-Doppler lobes are shown in Fig. 4.2d. An effective dual-Doppler measurement area mainly depends on three factors: the minimum spatial resolution adequate for resolving the phenomenon, the largest acceptable error in horizontal velocity, and the radar separation distance. Increasing radar separation can improve the accuracy of the two velocity components over a large area but degrade the spatial resolution close to the radars. The dual Doppler lobes can be defined by the intersection of the acceptable velocity error variance, and the maximum of the desired spatial resolution (Davies-Jones 1979; Friedrich and Hagen 2004). The maximum spatial resolution is determined by the radar separation distance and a selected cross-beam angle. In our case, the distance between the RCSL and RCWF is 39.26 km, yielding a fine resolution at close range. The beam crossing angle (β) is chosen to be 35^o so that the resolution of the resulting merged data is ≈ 1 km. The horizontal wind solution is a geometrically weighted sum of the radial velocities, and a square root of Doppler mean velocity variance can determine if the

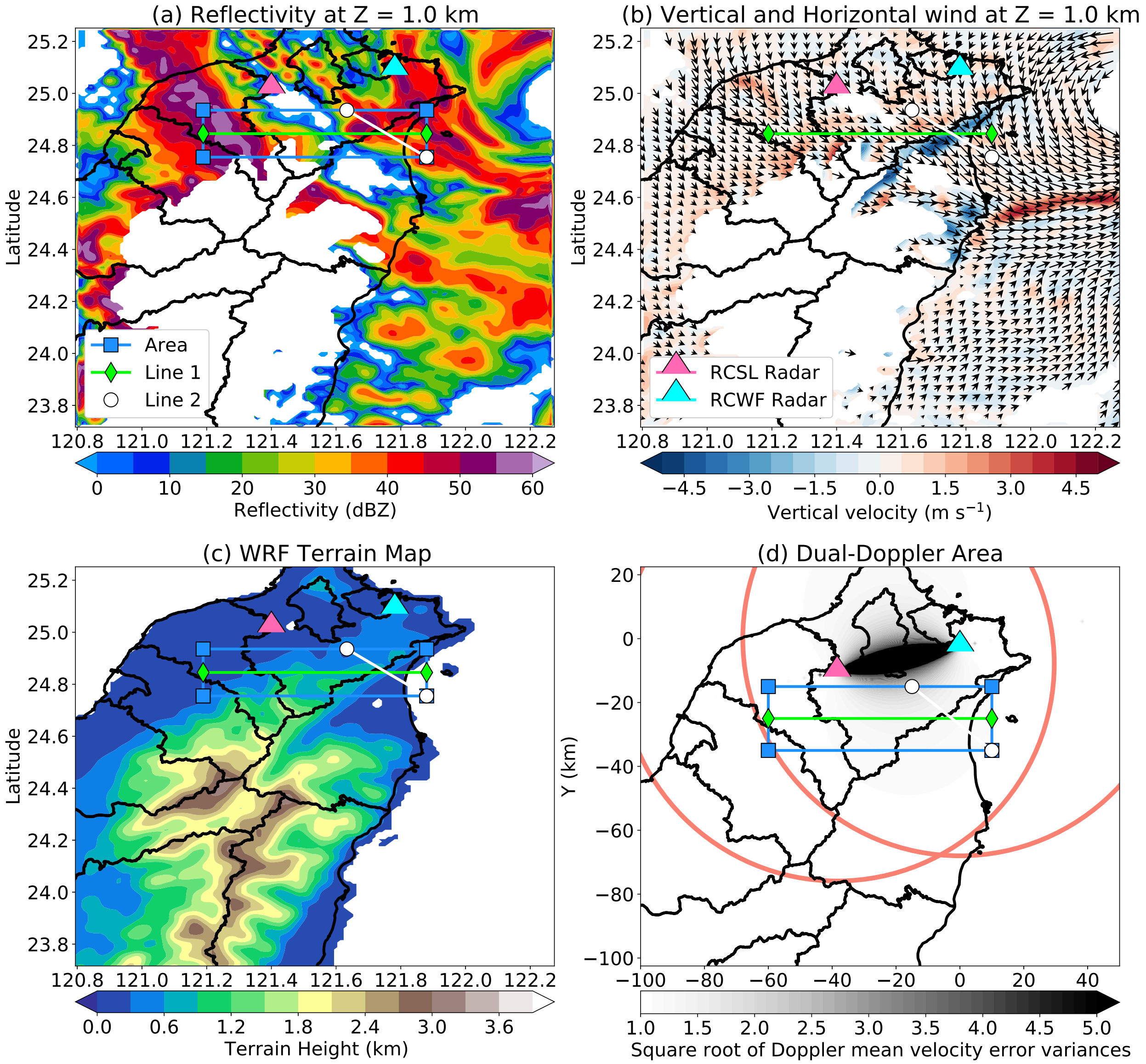

Figure 4.2: Horizontal cross sections of (a) reflectivity and (b) vertical and horizontal wind at 1 km altitude from the “truth”. (c) WRF terrain map. (d) The effective dual-Doppler radar lobes. Large red circles represent the maximum observing range of RCSL and RCWF, respectively. The shading denotes the Doppler mean velocity error variances of the two radars, which is determined by the dual Doppler radar beam geometry.

Table 4.1: The configuration of RCWF and RCSL radars.

Radar	RCWF	RCSL
Radar location	(25.071182N, 121.781205E)	(25.00N, 121.4E)
Radar height (m)	765	298
Radar frequency (GHz)	3.0 (S band)	5.5 (C band)
Beamwidth	0.89	0.92
Range resolution (m)	250.0	250.0
Elevation angle	0.4833984, 0.8789062, 1.318359, 1.801758, 2.416992, 3.120117,3.999023, 5.097656, 6.416016, 7.998047, 10.01953, 11.99707, 14.01855, 16.69922, 19.51172	1, 2, 3, 4, 5, 6, 9.9, 14.6, 19.5, 24.5, 29.9

geometry of two radar beams is ill-posed. Considering the above factors, the resulting area that is good for a dual-Doppler analysis is shown in Fig. 4.2d.

To conduct realistic testing using the Taiwanese radar operational network and assess the overall wind retrieval for the section 4.5 with real radar observations, we use the RCWF and RCSL radar configuration for the simulated radar measurements (Table 4.1). Plan position indicator (PPI) of simulated reflectivity and Doppler velocity observed by the RCSL and RCWF are shown in Fig. 4.3 as an example.

4.3.3 Assessment of accuracy

The accuracy of the retrieved results against the true variables is evaluated using the spatial correlation coefficient (SCC), and the root-mean-square error (RMSE), including horizontal wind field (u and v combined), vertical wind, and the first derivative of the wind field: divergence, and vorticity, are computed (Liou et al. 2012).

$$SCC(A) = \frac{(A_r - \bar{A_r})(A_t - \bar{A_t})}{\sqrt{(A_r - \bar{A_r})^2 (A_t - \bar{A_t})^2}} \tag{4.4}$$

$$RMSE(A) = \sqrt{\frac{\sum (A_r - A_t)^2}{M}} \tag{4.5}$$

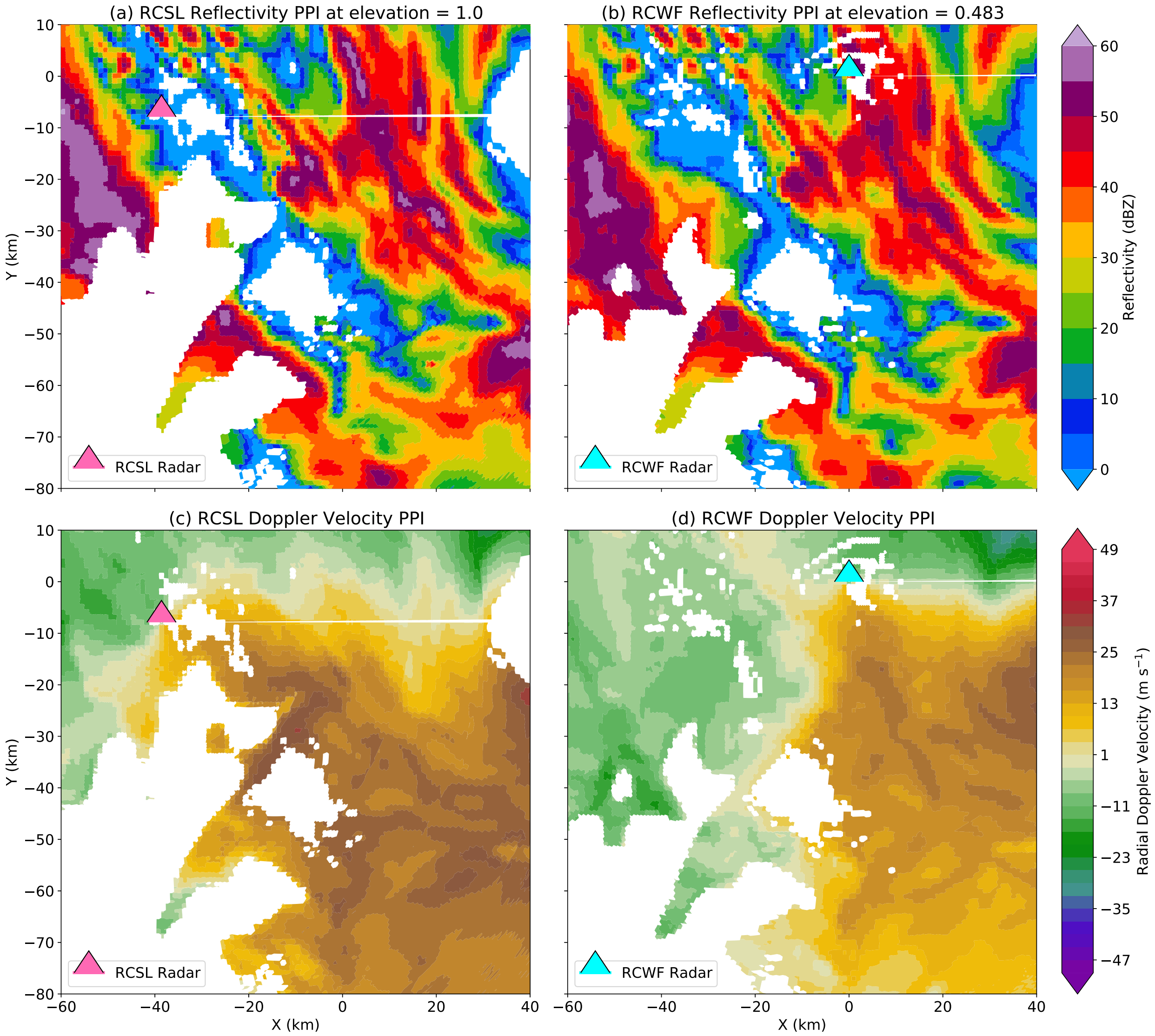

Figure 4.3: PPI scans of radar reflectivity from (a) RCSL at the elevation angle of 1 degree and (b) RCWF at 0.483 degree. (c) and (d) are Doppler velocity observed by RCSL and RCWF at the same PPI, respectively.

$$RRMSE(A) = \sqrt{\frac{\sum(A_r - A_t)^2}{\sum(A_t)^2}} \tag{4.6}$$

The subscripts "r" and "t" denotes the "retrieved" and "true" quantities, and M is the total number of grid points used in the computation. $\bar{A}$ denotes the value of the domain average.

The performance and code accuracy of the IBM method was first examined by an idealized two-dimensional mountain wave over a bell-shaped hill provided by the WRF (not shown). This test case was used to verify that topographic forcing is correct at the bottom boundary and the code is implemented reasonably because the slope of the hill is smooth and shallow. The SCC scores for u, w, and divergence 0.91, 0.96, and 0.96 respectively compared to the WRF simulation, demonstrating that the boundary is implemented correctly and the physical assumptions of the impermeability and topographic forcing are consistent with the model.

4.4 Sensitivity tests

In this section, we carry out a series of experiments to test the sensitivity of the prescribed strength of Neumann and Dirichlet boundary constraints, the algorithm assumptions of mass continuity and terrain boundary on the vertical wind and divergence retrieval, the smoothness of complex terrain, and the grid spacing and Gaussian recursive filter setting.

4.4.1 Terrain error sensitivity

Table 4.2 displays the experimental setup and their names for testing different terrain errors and the slope of terrain. Figure 4.4 shows the SCC score for the CR-SIM and radar-filter experiments with different terrain error setups. CR-SIM experiments with different prescribed terrain boundary errors all outperform the radar-filter experiments in the three-dimensional wind, divergence, and vorticity field. The CR-SIM experiments show that relaxing the pseudo-observational errors provided by the boundary to a higher degree can retrieve a horizontal wind field similar to the reference data with up to 0.992. The average SCC score for the horizontal wind across all 16 sensitivity tests is 0.99, suggesting that the horizontal wind retrieval from the Doppler velocity has high fidelity to the truth when there is sufficient data inside the domain of

Table 4.2: Configuration of different sensitivity experimental setups for testing the error of terrain boundary constraint, Doppler sampling limitations, and slope of terrain map.

Setup/Names	Reference (“Truth”)	CR-SIM: NE_**i**DE_**j**	Radar-Filter: NE_**i**DE_**j**	Radar-Filter: S_**k**
Data coordinates	WRF model grid (x, y, σ)	WRF model grid (x, y, σ)	Radar grid (azi, elev, range)	Radar grid (azi, elev, range)
Input data	u, v, w, T, q_v, ρ_a, ρ_m, Z_{hh}	Z_{hh}, V_d	Z_{hh}, V_d	Z_{hh}, V_d
Neumann Error (i) i in [0,1,2,3] (unitless)	1E-3	1E-3, 1E-2, 1E-1, 1E-0	1E-3, 1E-2, 1E-1, 1E-0	1E-1
Dirichlet Error (j) j in [0,1,2,3] (unitless)	1E-3	1E-3, 1E-2, 1E-1, 1E-0	1E-3, 1E-2, 1E-1, 1E-0	1E-1
Mean slope (k) (unitless)	6E-2	6E-2	6E-2	6E-2, 8E-2, 1E-1
# of experiment	1	4×4	4×4	3

interest. On the other hand, vertical wind retrieval is highly sensitive to the strength of imposing boundary conditions. If the Dirichlet error is relaxed to 1E-0, which is about two orders higher than the averaged terrain slope (6E-2), the SCC score is less than 0.78 and is insensitive to the order of the Neumann boundary error. If a strong Dirichlet boundary condition with an error of 1E-3 is imposed, the SCC score is below 0.76. When the Dirichlet error is set to 1E-1, only an order higher than the averaged terrain slope, the SCC score can reach as high as 0.9. The CR-SIM results highlight that setting the Dirichlet error to a similar order of the terrain slope map is important to reconstruct the wind field, but the Neumann boundary condition has less impact on the retrievals from our experiments when the data distribution and coverage are sufficient. The horizontal divergence and vertical vorticity are relatively insensitive to the different order of boundary errors (not shown). This experiment suggests that the Doppler error caused by the Doppler projection is trivial for the horizontal wind retrieval, but has more impact on the vertical wind because the vertical wind retrieval relies on the mass continuity equation and topographic forcing assumptions.

The average SCC score for the radar-filter sensitivity experiments is 0.94 and 0.73 for the horizontal and vertical wind retrieval, respectively. The scores are about 0.05 lower than the CR-SIM results, which are mainly due to fewer data points by the designed VCP. Interestingly, the highest SCC score of the horizontal wind field is found in the NE-1DE-1 experiment, and higher SCC score of the vertical wind mainly lies in the experiments with 1E-2 Dirichlet error, which is around the same order as the average slope of the terrain map. The shifting pattern compared to the CR-SIM experiments suggests that the imposed strength of terrain boundary conditions is more important when there is less data close to the surface and sparse data distribution.

Considering the SCC, and RMSE results (will be shown later), the NE-1DE-1 has the best retrieval in our case for this particular radar configuration and data distribution. Figure 4.5 shows a comparison of the "truth", the CR-SIM NE-1DE-1 experiment, and the radar-filter NE-1DE-1 experiment of the vertical cross sections (green line denoted in Fig. 4.2). A strong convective core with 60 dBZ at X = -55 km is associated with a 5 m s^{-1} updraft at z = 5 km. Although the retrieved vertical velocity from the CR-SIM and radar-filter experiments are both overestimated this particular updraft, the overall pattern is very similar to the "reality". The zonal wind depicts an enhanced upslope wind with divergence over the hill and is associated with a downdraft down the hill and negative vorticity from X = -30 to 0 km. The CR-SIM and radar-filter experiments resolve the feature of interest physically and qualitatively well, but the amplitude is not exact as expected due to Doppler errors, radar beam geometry, and limited data. One thing to note is that when there is less data close to the ground and poor geometry of dual-Doppler beams (X = 0-5 km), some artificial weak updraft and downdraft are produced. Nevertheless, the overall pattern resolves our scale of interest very well.

The RMSE of different boundary error experiments is shown in Fig. 4.7. The averaged RMSE of the horizontal wind field is 3.44 m s^{-1}, and 0.93 m s^{-1} for the vertical wind field. Similar to the SCC results, the CR-SIM experiments show that relaxing the Neumann boundary error achieves

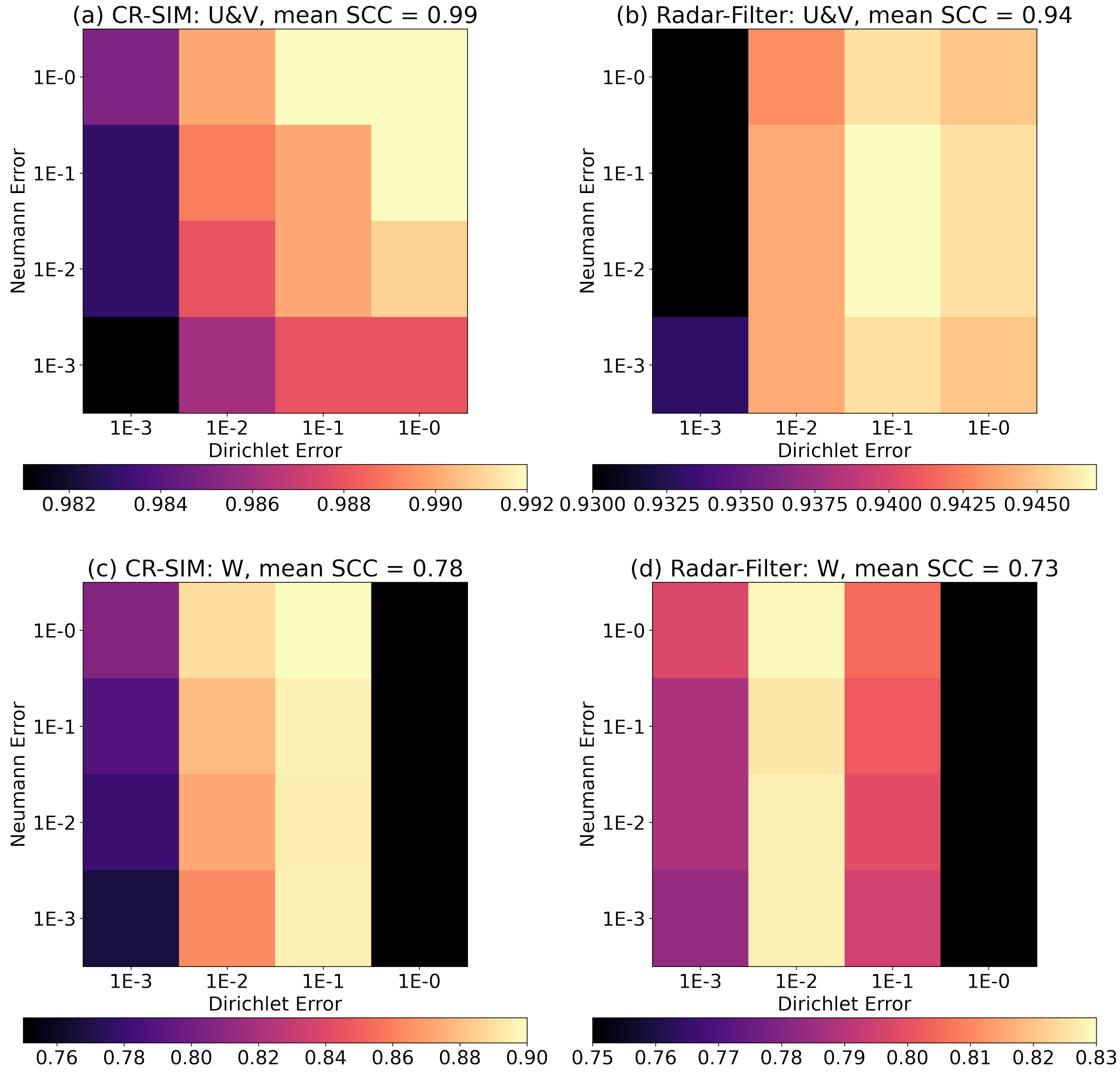

Figure 4.4: SCC score of wind field retrieved from the CR-SIM dataset (a and c), and radar-filter dataset (b and d). (a) and (b) are the score for the horizontal wind, and (c) and (d) are the score for the vertical wind. The score is computed using all the data point from the surface to 5 km within the blue box denoted in Fig. 4.2.

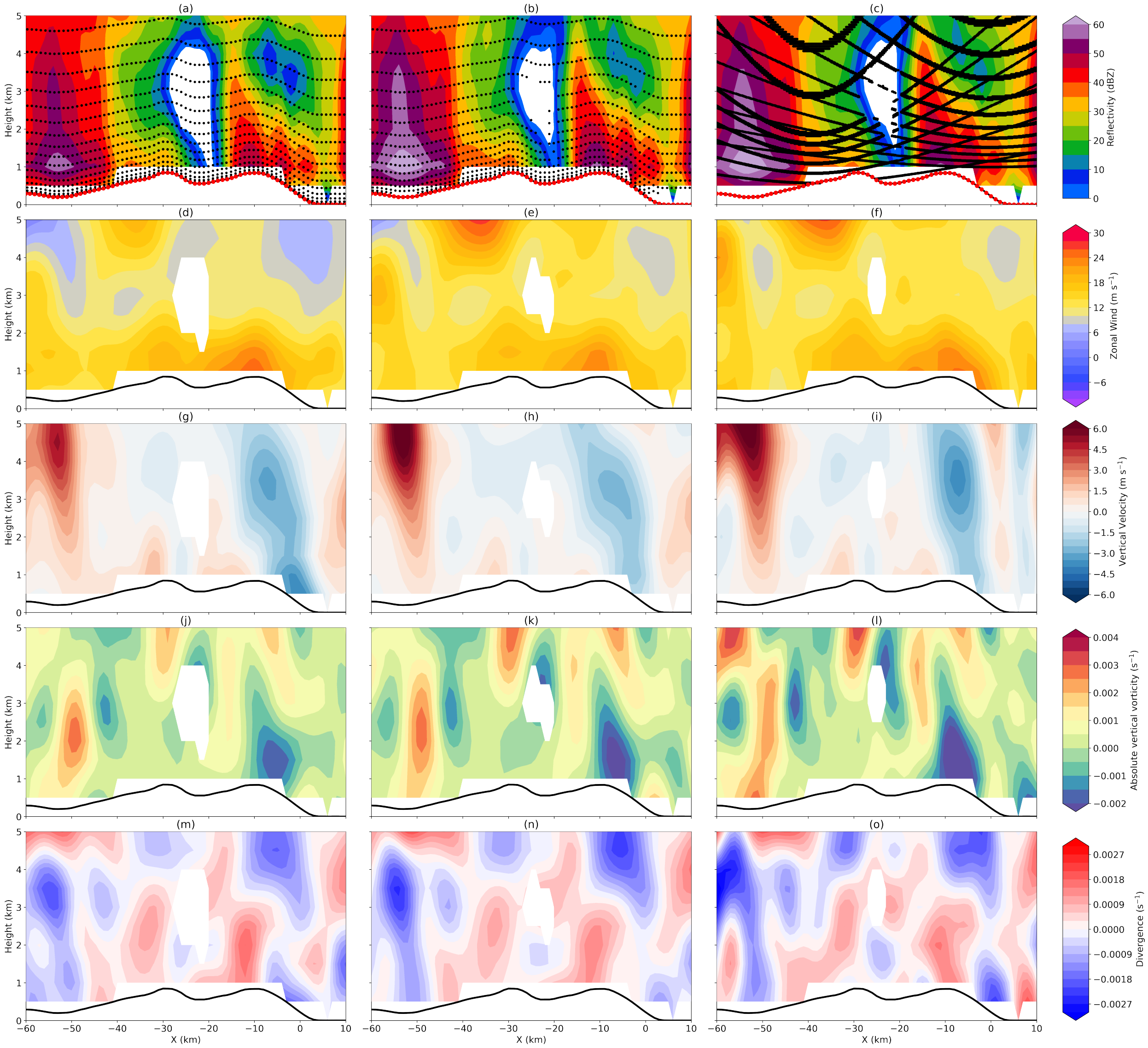

Figure 4.5: Comparison of the "truth", CR-SIM: NE-1DE-1, and radar-filter: NE-1DE-1 retrieval output (from left to right) with the vertical cross sections of reflectivity, zonal wind, vertical velocity, absolute vertical vorticity, and divergence (from top to bottom). The vertical cross section is the green line denoted in Fig. 4.2. The black dot denotes the data distribution, and the red dot denotes the pseudo-observations imposed by the Neumann and Dirichlet boundary conditions at the terrain height. The black line denotes the topography.

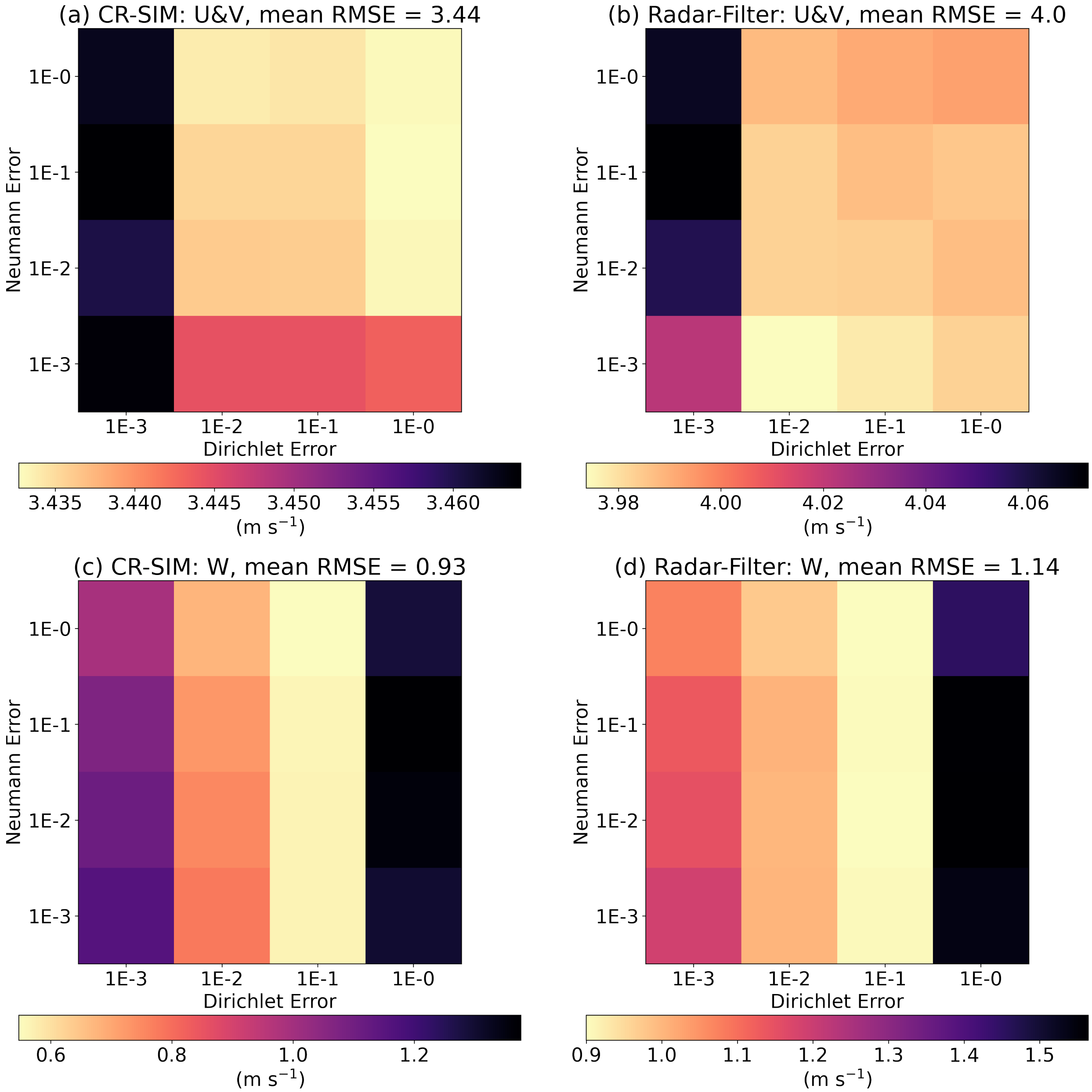

Figure 4.6: As in Fig. 4.4 but for the RMSE.

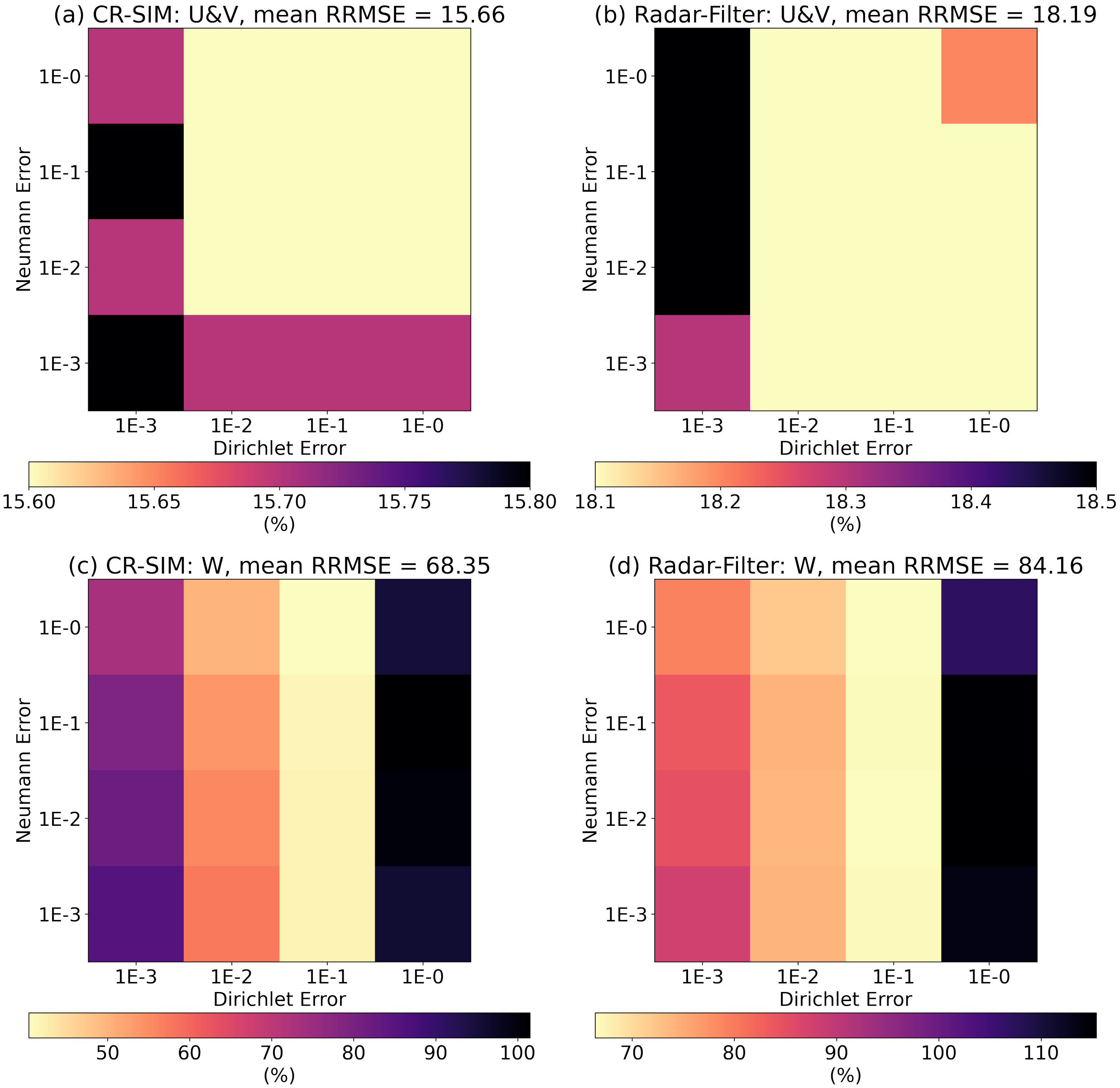
(a) CR-SIM: U&V, mean RRMSE = 15.66

(b) Radar-Filter: U&V, mean RRMSE = 18.19

(c) CR-SIM: W, mean RRMSE = 68.35

(d) Radar-Filter: W, mean RRMSE = 84.16

Figure 4.7: As in Fig. 4.3 but for the RRMSE.

the minimum RMSE, whereas the minimum RMSE (0.5 m s^{-1}) of the vertical motion is found when the Dirichlet error is set to 1E-1 across different magnitude of Neumann boundary error. The mean RMSE of the radar filter experiments is 4 m s^{-1} for the horizontal wind field, and 1.14 m s^{-1} for the vertical wind. The minimum RMSE of the horizontal wind is found in the NE-3DE-2 experiment. The range of horizontal wind RMSE is 0.1 between the maximum and the minimum, so the difference is very trivial. On the other hand, the RMSE of the vertical velocity in the radar-filter experiments has a similar pattern as the CR-SIM results. When the Dirichlet error changes from 1E-0 to 1E-1, the RMSE value shifts from 1.5 to 0.9 m s^{-1} on average, indicating that choosing a correct Dirichlet boundary constraint is important to have a better vertical wind retrieval result, consistent with the CR-SIM experiments. The RRMSE also shows a similar pattern as the RMSE results (Fig. 4.7). The mean RRMSE for the horizontal wind from the CR-SIM is 15%, and the radar-filter is 18% error. The mean RRMSE for the vertical wind is 68% for the CR-SIM, and 84% for the radar-filter.

Figure 4.8 shows another example of a vertical cross section across the snow mountain ridge denoted by the white line in Fig. 4.2. The shallow convection is associated with positive vorticity and upslope wind with a 2 m s^{-1} updraft and shallow convergence close to the ground. A jet with ≈ 32 m s^{-1} at $z = 3$ km is over the peak of the hill. CR-SIM and radar filter NE-1DE-1 experiments all pick up the pattern but with slightly underestimated downdraft magnitude at the lee side and an overestimated amplitude of the jet aloft and the position of the jet. The radar filter NE-1DE-1 experiment shows a strong updraft at 5 km height (between $X = 0$ and 5 km), which is due to the fact that there is no data close to the ground, so the mass continuity equation dominates the retrieval of vertical velocity over that region. Nevertheless, the retrievals with terrain boundary implementations can retrieve the scale of interest and are a good representation of the mesoscale features.

In order to address the sensitivity of various prescribed strengths of the boundary constraints, Figure 4.9 demonstrates the imposed boundary constraints can have a significant impact on the vertical velocity, vorticity pattern, and amplitude using the same vertical cross sec-

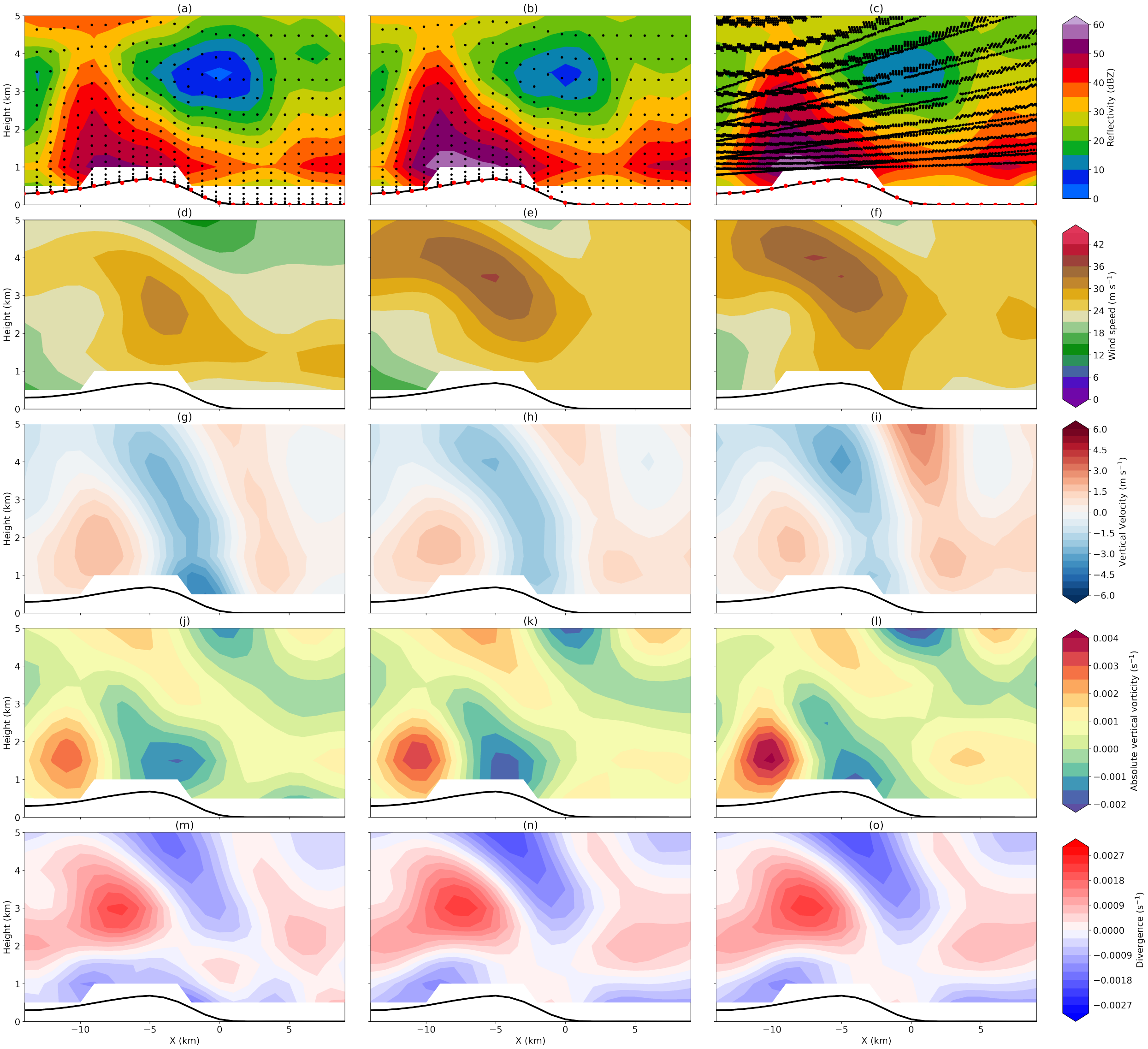

Figure 4.8: As in Fig. 4.5 but for the vertical cross section of reflectivity, wind speed, vertical velocity, absolute vertical vorticity, and divergence along the white line denoted in Fig. 4.2.

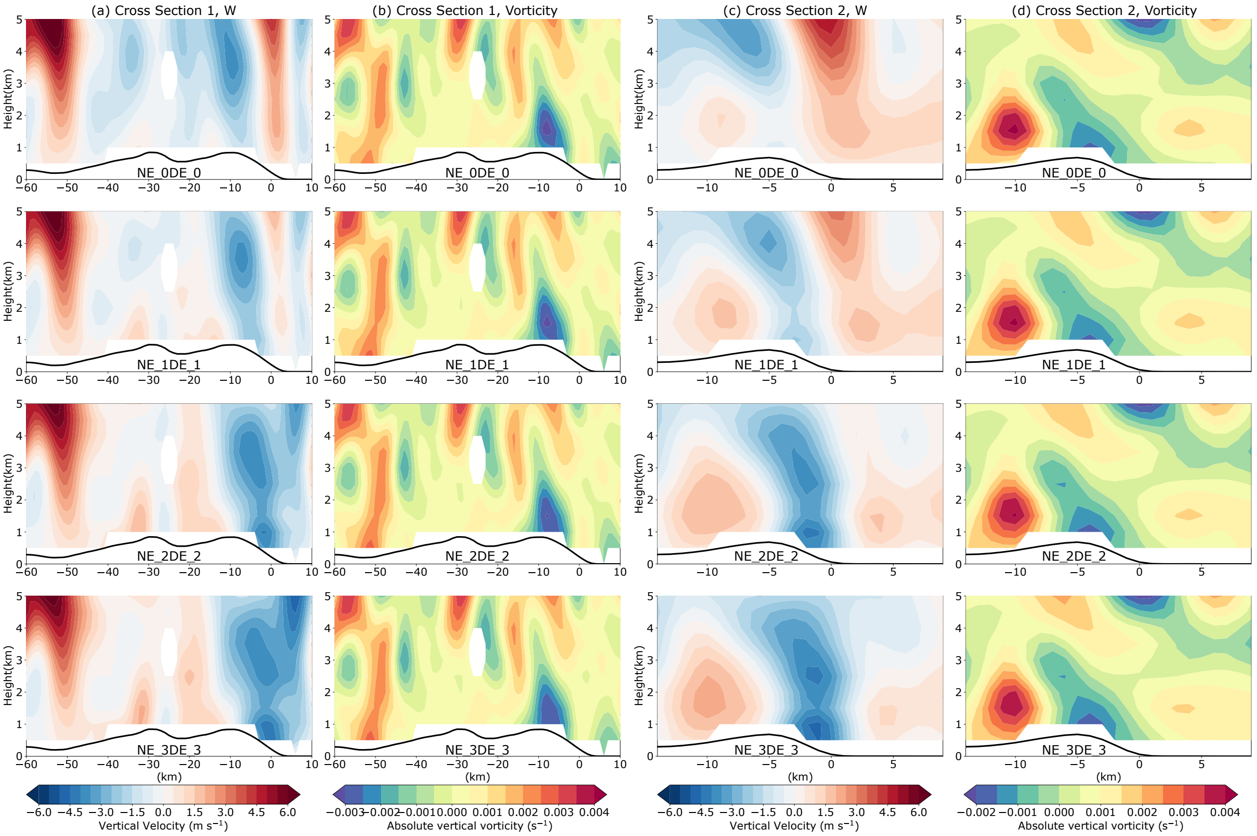

Figure 4.9: Comparison of the NE-0DE-0, NE-1DE-1, NE-2DE-2, NE-3DE-3 experiments (from the top row to the bottom). Vertical cross sections of (a), (c) vertical velocity and (b), (d) absolute vertical vorticity.

tion as Figs 4.5 and 4.8. The prescribed constraint for the mass continuity assumption is the same across all the experiments. When the Dirichlet boundary constraint is relaxed, enhanced vertical motion is mainly found above 3 km height from the two vertical cross sections. The mass continuity assumption dictates the vertical motion retrieval pattern. When the Dirichlet boundary condition is imposed with strict constraint, the terrain boundary becomes more influential on the vertical wind retrieval. For example, an enhanced downward motion locked to the terrain between -3 and 2 km is resolved better compared to the truth (Figs. 4.8g and 4.9c). As for the absolute vertical vorticity, the retrievals across all the experiments have good agreement with the WRF output when the data point and coverage are sufficient. The retrieval correctly identified an elongated positive vorticity from the surface to 3 km in between the two negative vorticity in the cross section 1 (Fig. 4.9b), and an enhanced negative vorticity on top of the peak between X = -10 and 0 km. The amplitude is slightly off but the pattern is identified well in general. Cross section 2 shows that the vorticity couplet close to the surface between X = -15 and 0 km is correctly identified but with slightly stronger amplitude compared to the WRF output.

The sensitivity experiment results for the order of terrain error show that the prescribed boundary constraint is necessary in order to retrieve a better vertical wind structure. The error order of the prescribed boundary constraint depends on the data density and distribution close to the ground. If data points are sufficiently close to the surface, the prescribed Neumann boundary constraint can be insensitive to the overall retrieval, but the Dirichlet boundary condition plays a more important role in the vertical wind retrieval. Although our results show that the best retrieval is obtained when the prescribed boundary constraint has a similar order to the averaged terrain slope, we only check this specific geometry, so the exact numerical errors may be different in other cases.

4.4.2 Averaged terrain slope sensitivity test

Orographic rainfall is sensitive to mountain dimensions, cross-barrier flow, moist static stability, and microphysical processes. An idealized two-dimensional modeling study conducted by Colle (2004) shows that the orographic precipitation is dependent on the mountain dimensions when the cross-barrier flow is less than 20 m s^{-1}. Kirshbaum and Durran (2005) using quasi-idealized numerical simulations shows that low-amplitude smooth topographic roughness is effective as more prominent sub-scale peaks at triggering and organizing banded orographic precipitation, and the bands created by isolated peaks can be sensitive to the location of those irregular peaks relative to the main ridge. On the other hand, a recent study conducted by Singh et al. (2021) suggests that using high-resolution topography for the model has the potential to reduce the biases of the local scale dynamics related to orographic features. Although the terrain resolution in our WRF simulation is 30-arc second (≈ 1 km) with an averaged mean slope of 6E-2 (Table 4.2), which is the actual physical scale that the model resolves, it is still worthwhile to explore how sensitive the retrieval is when using a terrain map with different degree of smoothing and filtering.

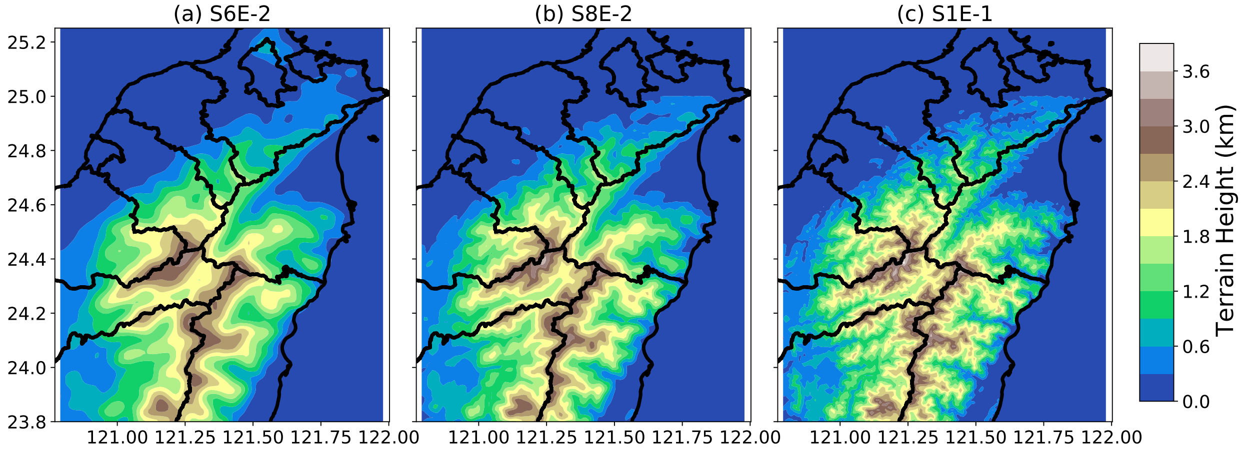

Figure 4.10: Complex terrain in Taiwan with a different averaged slope of (a)S6E-2, (b) S8E-2, and (c) S1E-1.

The Advanced Spaceborne Thermal Emission and Reflection Radiometer Global Digital Elevation Map (ASTER GDEM) was generated using stereo-pair images collected by the ASTER instrument (Spacesystems and Team 2019). The horizontal resolution of the ASTER GDEM data is 1 arc-second (≈ 30 m) grid of elevation postings. In order to reduce the computational time and match the scale of interest, we perform two methods to match the 1 arc-second data to the

30 arc-second grid. The first one is applying the Fast Fourier Transform (FFT) on the ASTER DEM data to remove any wavenumbers lower than 33 so that we can preserve the 1 km features approximately. This terrain map has an averaged terrain slope of 8E-2, which is very close to the terrain map in the WRF simulation but still retains some irregular peaks. The second one we sub-sample the ASTER DEM data and perform a nearest neighbor interpolation from high-resolution to low-resolution. This method preserves the most peaks with steeper slopes compared to the others, and the map has a value of 1E-1 averaged terrain slope.

Figure 4.10 displays the complex terrain with different degree of terrain slope. The topography in WRF has the most smooth terrain out of the three, and the terrain map using the nearest neighbor interpolation preserves the most detailed features. The sensitivity test in this section also varies the Neumann and Dirichlet boundary constraints to explore the relationship.

Figure 4.11 shows the RMSE results of using different terrain maps. As expected, using the terrain slope corresponding to the simulation has the minimum RMSE for the wind field because the original terrain map has a better representation of the phenomenon with the scale of interest. The RMSE of the S1E-1 retrieved wind is the highest among the three. In the S1E-1 experiment, the horizontal and vertical retrievals are the best when the Dirichlet constraint is prescribed with a 1E-1 error. The S8E-2 experiment also shows a similar pattern as the S1E-1, but with lower RMSE. All the experiments presented here are less sensitive to the Neumann boundary error, which can be due to the fact that the area of interest has good Doppler radar geometry.

Figure 4.12 shows the vertical cross sections with a value of 1E-1 for the Neumann and Dirichlet boundary error from the S6E-2, S8E-2, and S1E-1 experiments. The overall patterns are similar between the three and the model in general, which is consistent with the Kirshbaum and Durran (2005)'s results. When the terrain is steeper and has a more detailed structure, an enhanced downdraft close to the terrain peak (between X = -8 and -3 km) is found in the S8E-2 and S1E-1 experiments, and the enhanced downdraft in the S1E-1 has a magnitude up to 5.5 m s^{-1}. The divergence field shows that an enhanced convergence at 4.5 km height between X =

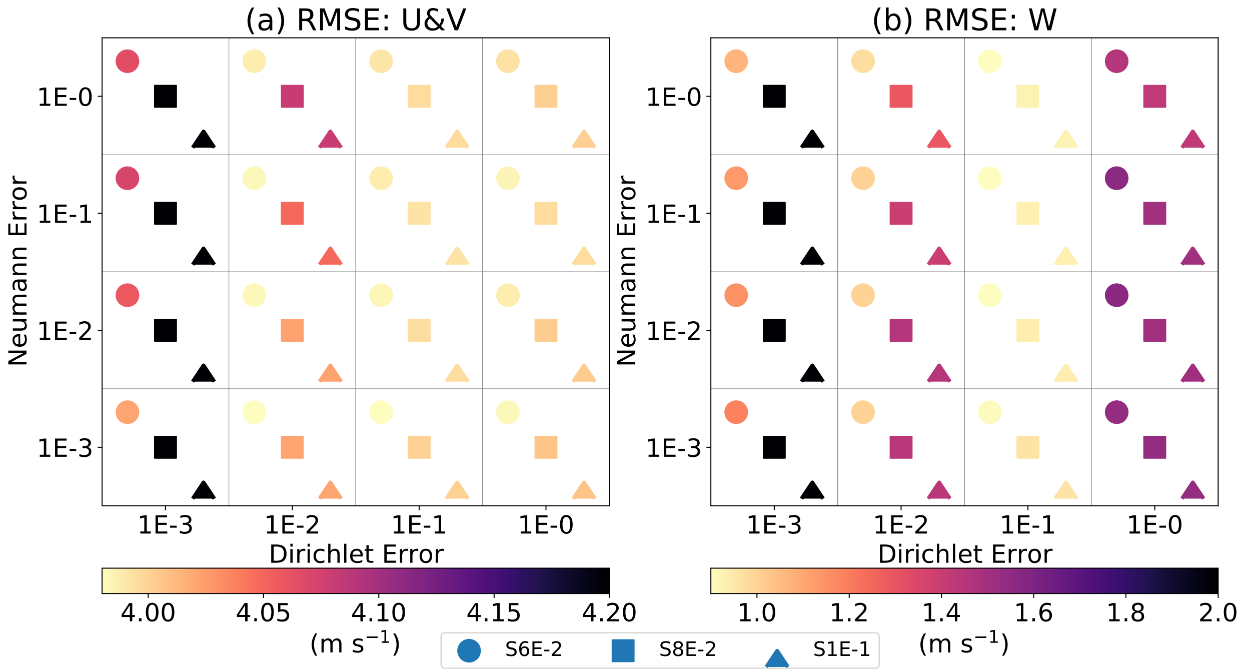

Figure 4.11: Scatter plot of the RMSE of the (a) horizontal wind and (b) vertical wind from the S6E-2, S8E-2, and S1E-1 experiments with different specified terrain boundary condition errors. The color shading of the dot denotes the magnitude of the RMSE.

-8 and -3 km is found in the S8E-2 and S1E-1, suggesting that the steepness of the terrain slope can propagate to higher altitudes but not just restricted to the low-levels. The results of this sensitivity experiment suggest that using the terrain map with an appropriate scale of interest is important to reconstruct the wind field. The terrain map with too steep terrain and detailed structure could potentially introduce features unable to be resolved properly on the grid scale.

4.4.3 Mass continuity equation and terrain boundary equation sensitivity test

The traditional way to retrieve the vertical air motion is to solve the integral mass continuity equation throughout the column through upwards integration from the bottom level and/or downward integration from the top level (Ray et al. 1980; Protat and Zawadzki 1999). This approach requires an estimate of horizontal wind divergence at each level, so the errors in horizontal wind divergence at each level can propagate and accumulate throughout the column, which further leads to a larger error in the retrieved vertical velocity. The variational approach has been shown to be less sensitive to the specifications of the boundary conditions for the ver-

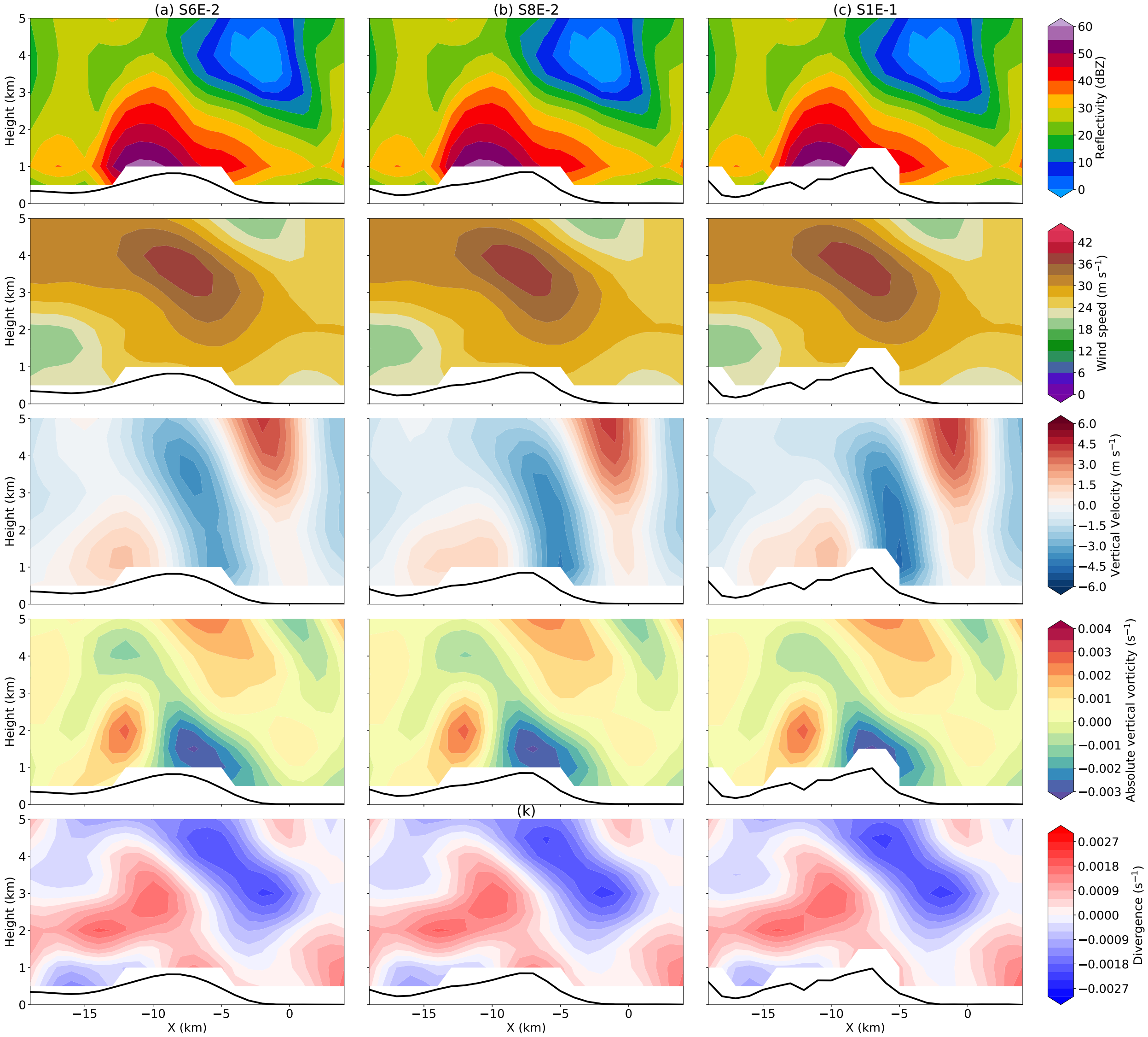

Figure 4.12: Same vertical cross section as in Fig. 4.8 but for the (a) S6E-2, (b) S8E-2, and (c) S1E-1 experiment with NE-1DE-1 error. The black line denotes the terrain height along the cross section.

tical velocity retrieval (Gao et al. 1999). In this sensitivity experiment, the algorithm assumptions of the mass continuity equation and terrain boundary conditions are explored with three types of experiments, and the configuration is detailed in Table 4.3.

Table 4.3: Configuration of different experimental setups for the purpose of testing the sensitivity of mass continuity and the IBM method for the three-dimensional wind retrieval. The prefix WM or NM indicates whether the mass continuity is activated or not. Similarly, the prefix WT or NT indicates whether the terrain boundary condition is activated or not.

Name	Mass Continuity, Error	Terrain boundary, (Neumann Error, Dirichlet Error)
WM-NT	Yes, 1	No, (N/A,N/A), $w = 0$ at z = 0
NM-WT	No, N/A	Yes, (1E-1, 1E-1)
WM-WT	Yes, 1	Yes, (1E-1, 1E-1)

Figures 4.13 and 4.14 show the vertical cross sections of the experiments. First of all, the WM-NT experiment produces artificial wind below the terrain, with weak zonal wind and vertical velocity close to the ground because there is no data below the topography so the data were interpolated to the z = 0 km. Second, the WM-NT result shows that the horizontal wind field, first-order derivative of the horizontal wind (vorticity and divergence) have a similar pattern when the retrieval is above the terrain. The zonal wind between X = -5 and 5 km close to the terrain height is up to 30 m s^{-1} speed, whereas the zonal wind retrieved by the WM-WT is only 25 m s^{-1}. Third, lack of terrain boundary constraints has a huge impact on the vertical wind retrieval. The WM-NT produces four strong updrafts with $\approx$ 6 m s^{-1} and one downdraft with 5 m s^{-1} maximized at 3.5 km height. The WM-NT resolves the two uphill updrafts (one is between X = -40 and -30 km, and the other one is between X = -20 and -10 km), but the amplitude is too strong and the motion extends vertically upward compared to the truth. For the NM-WT experiment, the horizontal wind, vorticity, and divergence field are in good agreement with the WM-WT experiment, which is similar to the WM-NT. The enhanced vertical velocity is locked to the terrain, and the vertical velocity is around zero above the height of 4 km.

Figure 4.14 shows the vertical cross section 2. The overall findings are similar to Fig. 4.13, but one interesting to note is that a weak updraft (between -10 and -5 km) associated with the upslope wind is not resolved by the WM-NT experiment. We suspect that the low-level jet between 3 and 5 km height is interpolated to the z = 0 km height, resulting in strong divergence below the terrain and a compensated downdraft aloft that mitigates the upward motion. The NM-WT experiment produces a much stronger downdraft up to -6 m s^{-1} and is shifted downhill and close to the surface compared to the WM-WT. These experiments show that the assumptions of the mass continuity and terrain boundary conditions are required in order to obtain an accurate and good representation of the vertical wind field.

4.4.4 Grid spacing and filter sensitivity experiments

In principle, five grid points at minimum are required in order to represent a wave on a grid so that the resolvable wave is of 2 data spacing Δn scale (Koch et al. 1983). In order to represent a proper resolvable wavelength, Δx should not be larger than 1/2 of Δn. For the lower limit, the grid spacing is not recommended to be too fine as calculations of derivative quantities are highly sensitive to the grid length. Therefore, the empirical ratio between the grid spacing Δx) and the data spacing Δn ($\Delta x/\Delta n$) lies in the range of 1/3 to 1/2. In SAMURAI, the resolved wind field is a function composed of finite elements. The grid-spacing determines the minimum spatial scale resolved by the cubic B-spline function. The Gaussian filter produces a Gaussian response to a point observation but can damp the amplitude of lower wavelengths and make the retrieval less sensitive to noise. Setting a combination of grid spacing and filter for the retrieval is critical in order to retrieve the best representation of the scale of interest. For example, if the scale of interest is 4 km, the grid spacing can be set to 1 km, and the Gaussian filter is set to 4. Or, the grid spacing can be set to 2 km, and the Gaussian filter is set to 2. This setting can have a good representation of the scale of interest, but features and noise with wavelengths less than 4 km will be damped.

The WRF output has a horizontal resolution of 1 km, and a typical WRF resolving scale is around $7\Delta x$ (Skamarock 2004). The radar-filter output resamples the WRF wind field and the

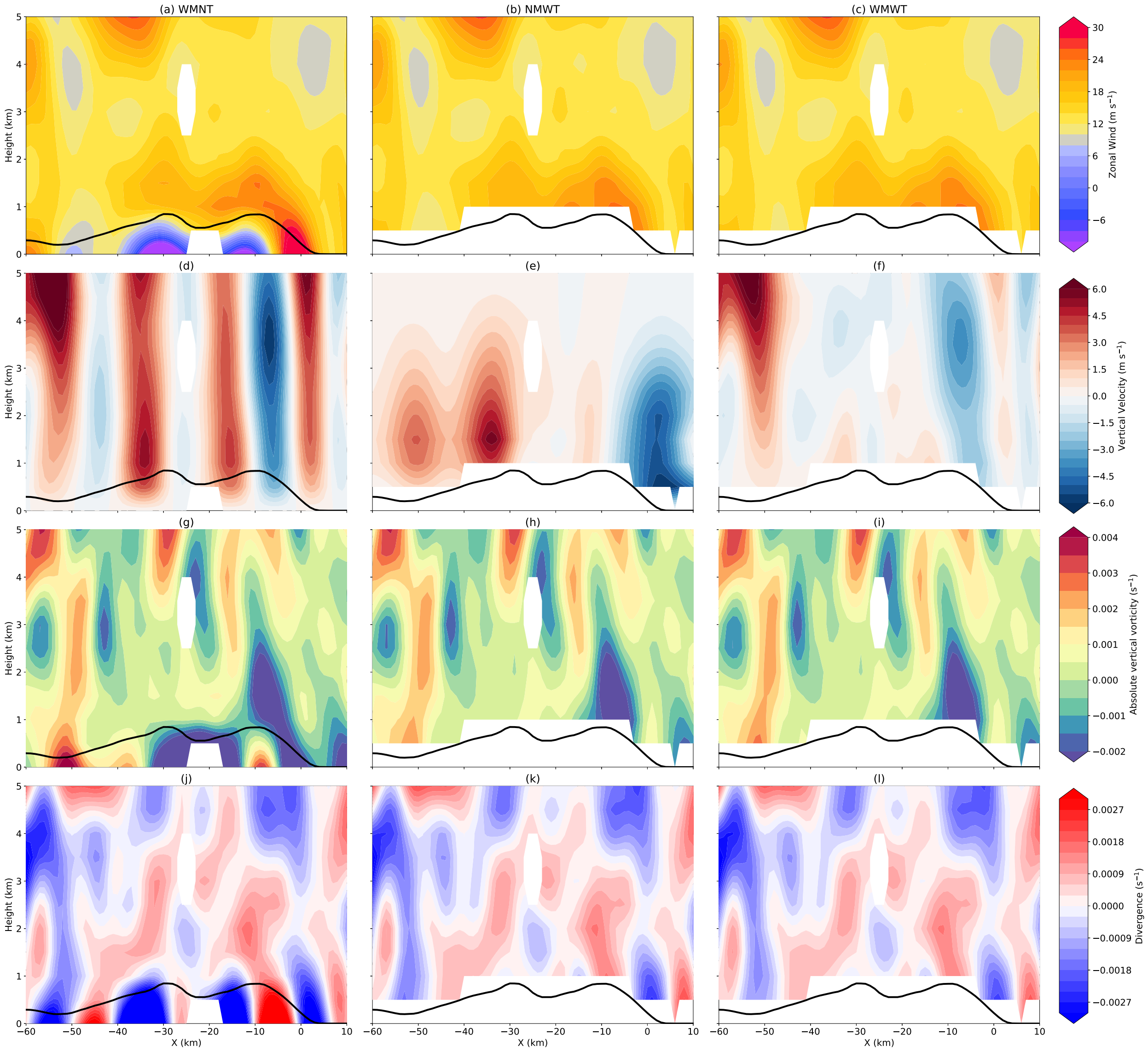

Figure 4.13: Same vertical cross section as in Fig. 4.5 but for the (a) WN-NT, (b) NM-WT, and (c) WM-WT experiment with zonal wind, vertical velocity, absolute vertical vorticity, and divergence from the top to the bottom. The black line denotes the terrain height along the cross section.

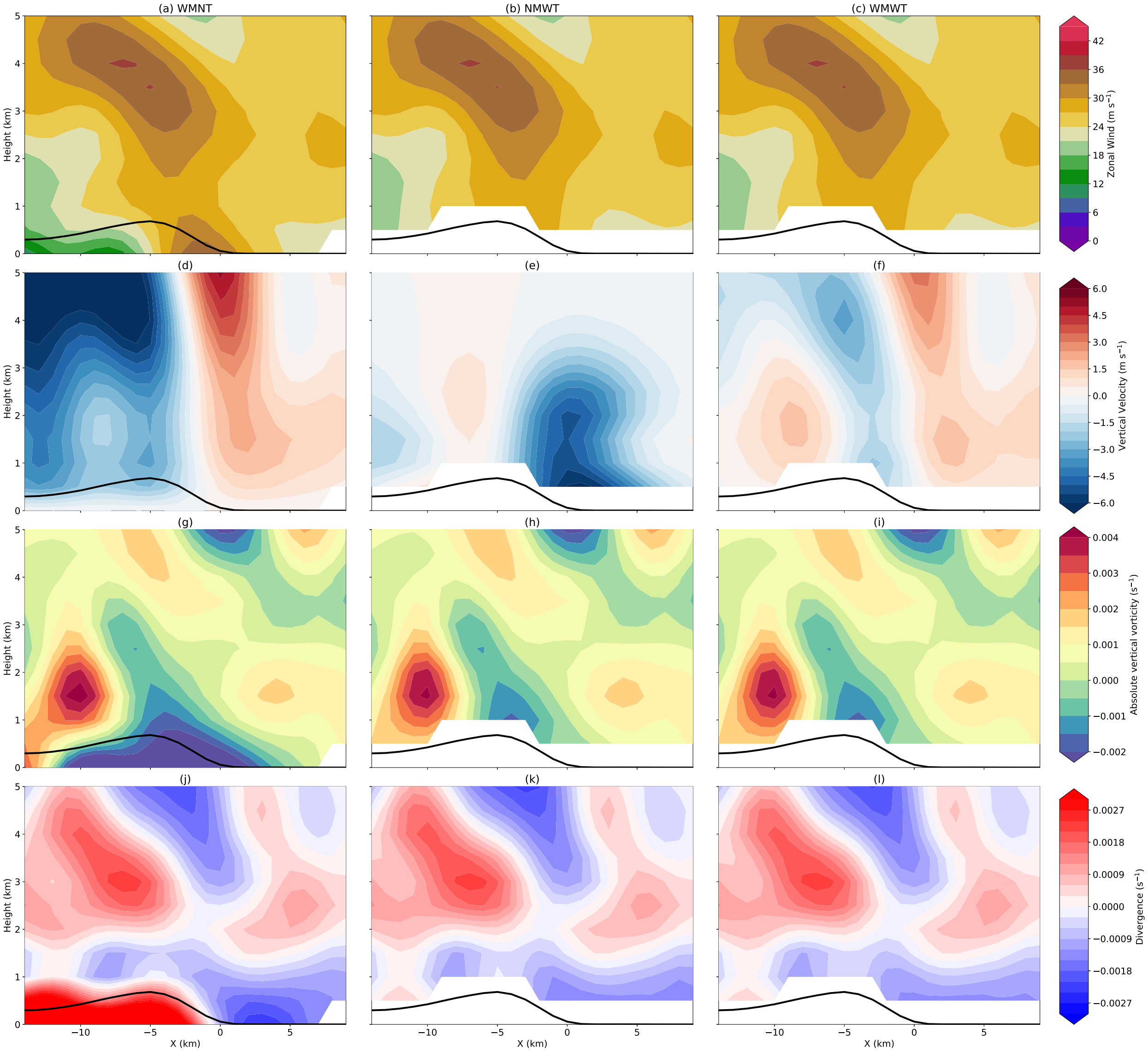

Figure 4.14: Same vertical cross section as in Fig. 4.8 but for the (a) WN-NT, (b) NM-WT, and (c) WM-WT experiment with wind speed, vertical velocity, absolute vertical vorticity, and divergence from the top to the bottom.

effective spatial resolution is ≈ 1 km in the region of interest. According to the given sampling and the theoretical understanding, setting the grid spacing to 0.5 km is more appropriate to resolve the detailed structure (Koch et al. 1983; Ooyama 1987, 2002b). A sensitivity test of different grid spacing and the length of filter setup is shown in Table 4.4.

Observations always contain a certain degree of noise, and the Gaussian filter can smooth the noise. The uncertainty in the wind field should be less than 2 m s^{-1} for a well-resolved Doppler geometry (Hildebrand et al. 1996). Considering the sub-grid scale turbulence and Doppler velocity instrument noise, we add Gaussian noise with 1 standard deviation of the Doppler velocity for the input data.

Figure 4.15 shows the results from each sensitivity experiment compared to the WRF simulation. The Grid05Filter222 retains more detail, but the overall retrieval is noisy, especially for the vorticity and divergence fields because the derivative of the wind field is more sensitive to the wind gradient. This experiment resolves the 1 km features and the Gaussian filter is not strong enough to dampen the noise. The RMSE of the vertical velocity is 0.77.

The Grid05Filter442 and the Grid10Filter222 resolve a similar horizontal scale as 2 km, but the Grid10Filter222 retains more details whereas the Grid05Filter442 analysis is smoother because the Gaussian filter is stronger to damp more noise (Fig. 4.15b and c). The Grid10Filter442 has a minimum of RMSE for the horizontal and vertical wind with 1.85 and 0.76 m s^{-1}, respectively across all the tests. The demonstration of the vertical cross section shows that the Grid05Filter442 and Grid10Filter222 can resolve a similar pattern as the WRF output with detailed structure, but the Grid10Filter442 has a better representation of the scale of interest.

Since the spatial resolution, resolved scales, and accuracy of the wind and terrain boundary constraint depend strongly on the Doppler velocity quality and sampling, it is not possible to recommend a specific filter length, grid spacing, terrain constraint, and the order of the terrain slope for all cases. The retrieval from OSSE experiments shows that a 0.5 km grid spacing in the horizontal and a 4 Δx Gaussian recursive filter lengths in the horizontal direction provide the most detailed structure, while 1 km grid spacing in the horizontal and a 4 Δx Gaussian recursive filter lengths in the horizontal direction provides higher confidence of the structure and magnitude of the dominant mesoscale features. The sensitivity experiments show different analysis settings can cause an inherent trade-off between the level of detail and point-wise accuracy. The settings must be assessed on a case-by-case basis and interpreted appropriately when making scientific conclusions.

Table 4.4: Configuration of different experimental setups for the purpose of finding the best resolving features with given horizontal data spacing of 1 km from the WRF simulation.

Name	Nodal spacing (km)	Gaussian Filter setting (i, j, k)	Approximately resolved scale (km)
Grid05Filter222	0.5	(2,2,2)	1
Grid05Filter442	0.5	(4,4,2)	2
Grid10Filter222	1.0	(2,2,2)	2
Grid10Filter442	1.0	(4,4,2)	4

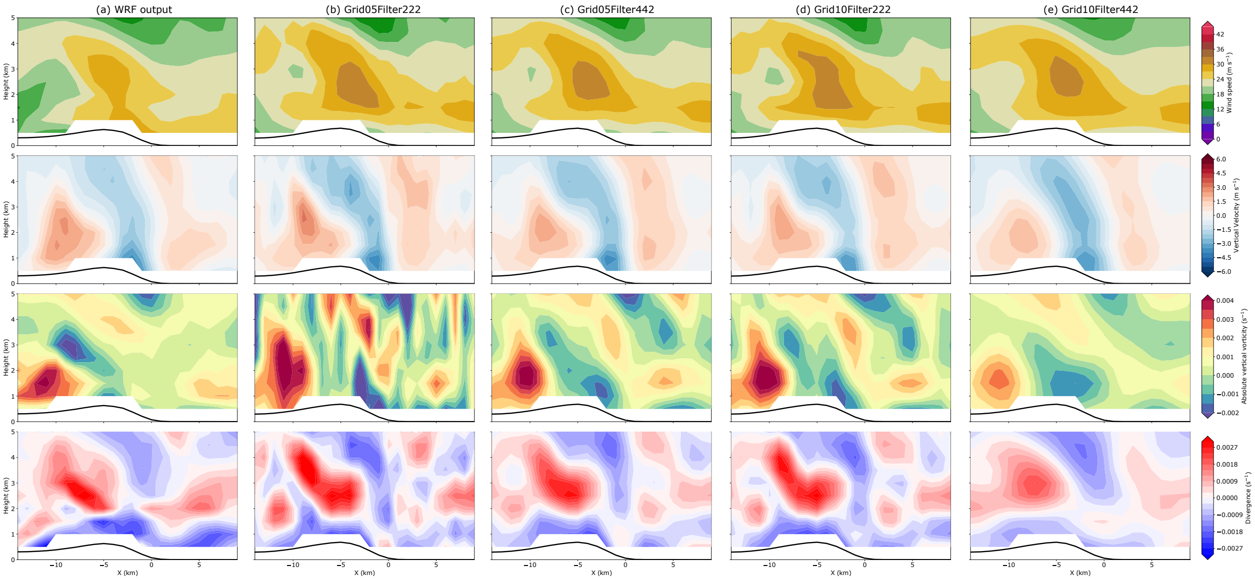

Figure 4.15: Same vertical cross section as in Fig. 4.8 but from the (a) WRF simulation, (b) Grid05Filter222, (c) Grid05Filter442, (d) Grid10Filter222, and (e) Grid10Filter442.

4.5 Application of real data

This section will demonstrate the applicability of the improved SAMURAI approach using real data from Typhoon Chanthu (2021) observed by the RCSL and RCWF radars. The radar configurations and settings are shown in Table 4.1. Using real data adds additional challenges because the data coverage is not complete and beam blockage will prevent observations near the ground and lee side of a hill in a mountainous region. Lack of data close to the terrain could limit the capability to understand the topographic forcing. In addition, the quality of the wind field depends on the Doppler velocity quality and scanning geometry. Considering all the sensitivity tests examined by the OSSE dataset and the limiting factors for real radar observations, the pseudo-observations of the Neumann and Dirichlet boundary with a prescribed constraint of 1E-1, terrain map with a mean slope of 6E-2, 1-km horizontal grid spacing, 0.5 km vertical grid spacing, and a 4Δ nodal spacing in the horizontal dimension and 2Δ spacing in the vertical dimension for the Gaussian recursive filter length were set for creating the analysis.

The radar sweep files were processed with Lidar Radar Open Software Environment (LROSE) software (Bell et al. 2021) and the National Center for Atmospheric Research (NCAR) SoloII software to correct Doppler velocity aliasing and remove non-meteorological echoes and noise. The edited sweep files were converted to the CfRadial format in the native radar polar grid and were analyzed by the improved SAMURAI technique.

Horizontal cross sections of the SAMURAI analysis show a rainband moving inland with reflectivity values over 50 dBZ at 1 km altitude, illustrating some enhanced precipitation on the uphill side (Fig. 4.16) Interestingly, an elongated, thin band of downward motion parallel to the mountain range (between 121.6 and 121.8 ^{o}E, 24.7 and 24.9 ^{o}N) is found at z = 1 km, collocated with a band of positive vorticity. Upward motion is most dominant on the windward side of the mountain range and increases with height, but the wind along the baseline has less confidence. Considering the dual-Doppler lobes and data scarcity, we focus on the vertical cross section denoted by the white line where the area has good dual-Doppler radar beam coverage. This cross

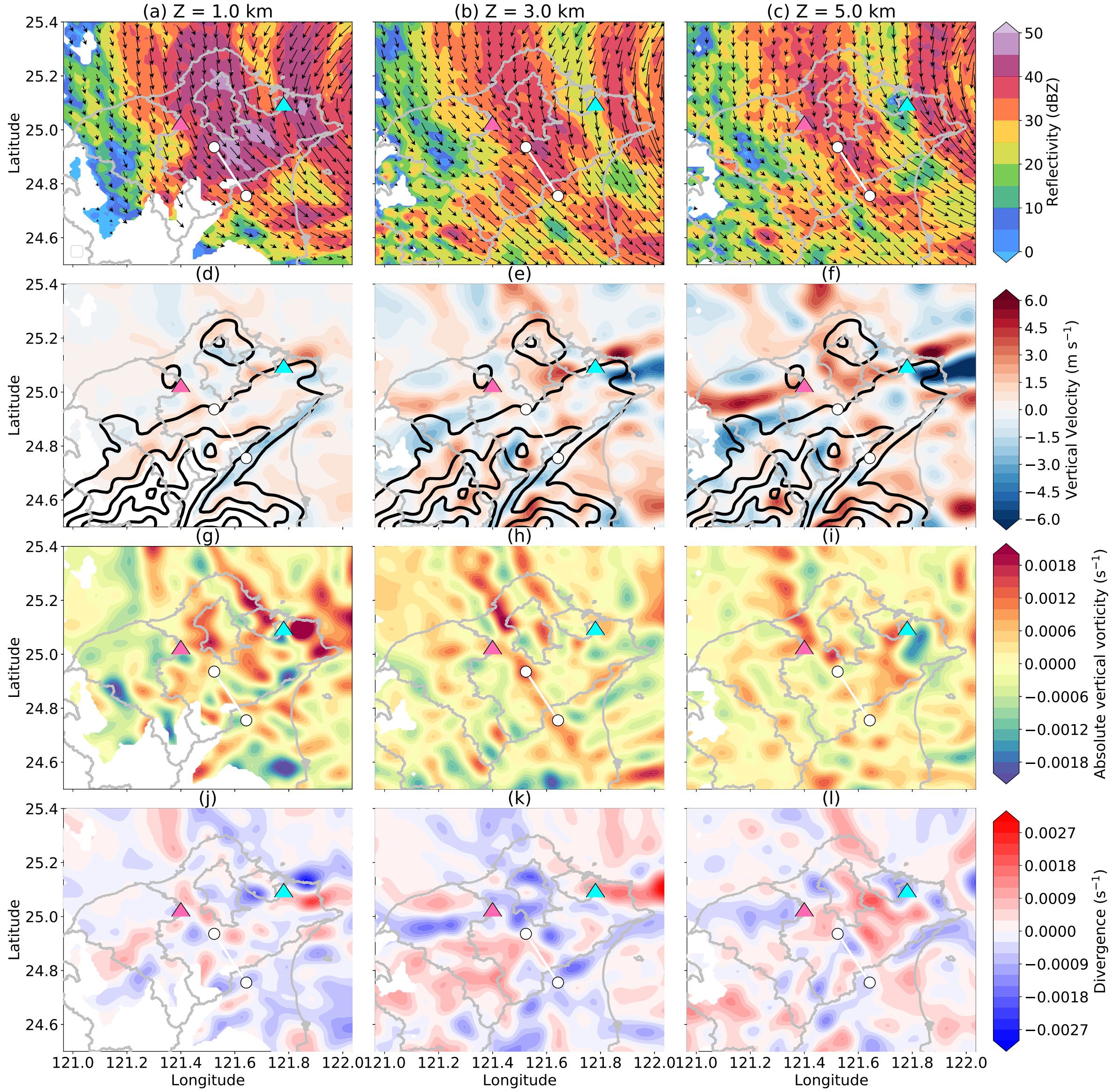

Figure 4.16: Horizontal cross sections of (a-c) reflectivity, (d-f) vertical motion, (g-i) absolute vertical vorticity, (j-l) divergence. (a), (d), (g), (j) are at 1 km altitude. (b), (e), (h), (k) are at 3 km altitude, and the black contour denotes the topography. (c), (f), (i), (l) are at 5 km altitude.

section is parallel to the rainband's horizontal wind flow, and is perpendicular to the mountain ridge, which makes it easier to assess if the retrieved wind field is physically realistic.

Figure 4.17 shows the vertical cross section of reflectivity, wind flow, vorticity, and divergence. Figure 4.17a shows a shallow reflectivity echo with 50 dBZ at 1 km height found on the windward side, and the enhanced echo extends to 6 km height (between X = -20 and -16 km). In this area, the shallow stratiform precipitation close to the ground is associated with upslope wind and divergence. The stratiform region has convergence at 4 km (Fig. 4.17e) with upward motion aloft and downward motion below (Fig. 4.17c), which is consistent with the understanding of a stratiform heating profile.

Between X = -16 and -12 km, as the wind flow climbs uphill, an induced upward motion (2 m s^{-1}) associated with negative vorticity (-0.0012 s^{-1}) and weak divergence are found near the terrain. The upward motion extends vertically with a maximum amplitude of 5 m s $^{-1}$ at 5 km height, and the vertical velocity is associated with a positive vorticity, convergence below, and divergence aloft.

A linear theory of orographic precipitation developed by Smith and Barstad (2004) shows that the orographic enhancement precipitation is highly correlated with the low-level cross-barrier flow when the low-level flow is unblocked by terrain. One forecasting criterion for evaluating terrain blockage is to calculate the mountain Froude number $F = U/NH$, where U is the upstream wind speed, H is the mountain height, and N_m is the Brunt-V$\ddot{a}$is$\ddot{a}l\ddot{a}$ frequency. In this vertical cross section, H is ~ 900 m, U is ~ 20 m s^{-1}, N_m ranges from an order of 10^{-3} to 10^{-2} depending on the moisture. Since we do not have a sounding profile for this case, F ranges from 2.2 to 22.2 by rough estimation. $F > 1$ implies that the airflow can ascend over the mountain. The cross-barrier wind flow is maximized at the mountain peak with over 25 m s^{-1}, and decreases in the lee. The enhanced cross-barrier wind at the peak demonstrates that the airflow successfully ascends over the mountains rather than being blocked. Our radar analysis is consistent with general theoretical understanding.

The flow in the lee is associated with downward motion, positive vorticity close to the topography, and convergence slightly above the ground. An in-depth analysis of the evolution of Typhoon Chanthu's rainband and its relationship to topography is beyond the scope of the current study and will be presented in a subsequent study.

4.6 Summary and discussion

The immersed boundary method is implemented to a three-dimensional variational-based multi-Doppler radar wind synthesis algorithm successfully. The performance of the improved SAMURAI technique is investigated using model-simulated datasets resampled by a radar emulator to provide more realistic setting for the simulated radar observables. The sensitivity of topographic forcing provided by the terrain boundary constraints, the sensitivity of terrain slope, the sensitivity of algorithm assumptions of the mass continuity equation and the terrain boundary conditions, and the sensitivity of grid spacing and filter setting are explored. Finally, an observational radar analysis is presented to support the conlcusion that this new technique can advance scientific analyses for understanding the impact on precipitation and wind flow caused by orographic forcing using observational datasets.

In this improved SAMURAI technique, the Neumann and Dirichlet boundary conditions are treated as pseudo-observations, so the strength of prescribed boundary constraints due to the topographic forcings can be adjusted by users. The sensitivity test shows that the Dirichlet boundary constraint has more impact on the vertical wind retrieval compared to the Neumann boundary condition in general. The sensitivity test also shows that the smoothness of the terrain map can have impact on the overall retrieval. A terrain map with too steep of a slope for a given grid resolution could produce erroneous results due to the inability to resolve sub-grid scale winds. A terrain map with shallower slope can provide a relatively smooth retrieval with good representation of mesoscale features. The algorithm assumptions of the mass continuity and topographic forcing provided by the Dirichlet boundary condition are required in order to produce realistic wind retrieval. Analyses losing one or the other will lead to incorrect wind retrieval representation and could be scientifically misinterpreted. The grid spacing and Gaus-

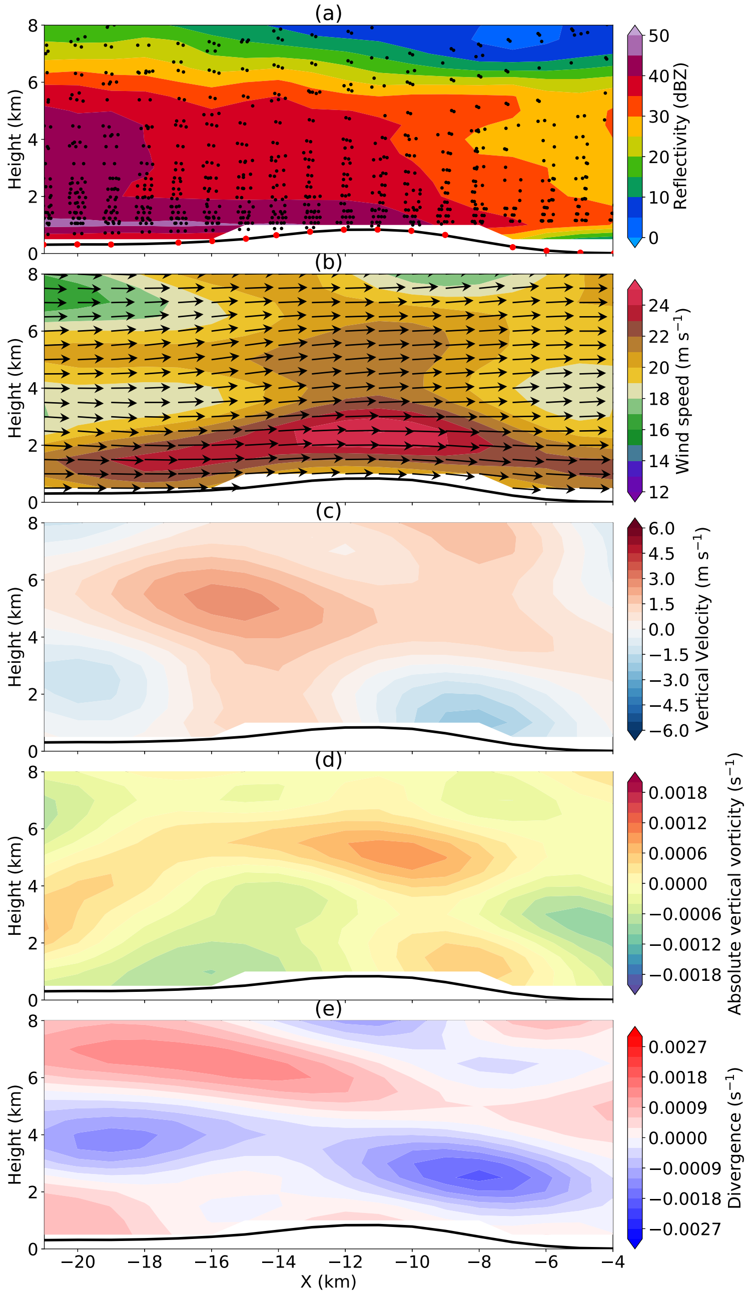

Figure 4.17: Vertical cross sections of (a) reflectivity, (b) wind speed, (c) vertical wind, (d) absolute vertical vorticity, and (e) divergence denoted by the white line in Fig. 4.16. The black dot denotes the Doppler radar observations, and the red dot denotes the pseudo observations created by the boundary condition. The black line denotes the topography. The wind vector in (b) denotes the wind direction and magnitude along the cross section.

sian recursive filter experiment show that increasing the Gaussian recursive filter can damp the noise and retain the features with a strong signal, but there is a trade-off of losing some detailed structure. In general, setting up smaller grid spacing than the data spacing with a larger filter length is recommended if the data coverage is complete and data points are sufficient. Our results are based on this one particular dual-Doppler geometry, so the exact numerical errors may be different in other cases. Caution must be taken when setting up the parameter for retrieving the optimal analysis and how to interpret the results. In future work, a sensitivity test of beam blockage effect due to complex terrain should also be considered. Additional observational case studies are also recommended to gain scientific insight in other regions and weather systems.

Chapter 5

Conclusions

Collecting observations and retrieving and identifying salient weather characteristics are essential to better understand the weather systems and improve forecasting. However, the state-of-the-art observational instruments and retrieving techniques are limited in their ability to reconstruct detailed kinematic and thermodynamic structures with high spatial and temporal resolution. TC intensity change caused by the inner-core dynamics is one of the most challenging prediction to make. More observations and a better understanding are required in order to improve the forecast model and parametrization schemes. On the other hand, even though weather systems over land are usually captured well by instruments and radar observations, there are limited multi-Doppler retrieval techniques designed for retrieving wind fields over complex terrain. This dissertation seeks to improve our understanding of dynamics of weather systems by using and improving radar retrieval techniques and a simple modeling approach.

In Chapter 2, polygonal eyewall asymmetries of Hurricane Michael (2018) during rapid intensification (RI) are analyzed from ground-based single Doppler radar. This work presents the first observational evidence of the evolving wind field of a polygonal eyewall during RI to Category 5 intensity by deducing the axisymmetric and asymmetric winds at 5-minute intervals using the generalized velocity track display technique (Jou et al. 2008; Cha and Bell 2021). Spectral time decomposition of the retrieved tangential wind structure shows quantitative evidence of low (1 - 4) azimuthal wavenumbers with propagation speeds that are consistent with linear wave theory on a radial vorticity gradient, suggesting the presence of rapidly-evolving vortex Rossby waves. Dual-Doppler winds from the airborne NOAA P-3 Hurricane Hunter provide further evidence of the three-dimensional vortex structure that supports growth of asymmetries during RI. Both reflectivity and tangential wind fields show polygonal structure and propagate at similar speeds, suggesting a close coupling of the dynamics and the convective organization during the intensification. The results highlight the value of coastal radar observations to investigate physical mechanisms of TC intensity and structure evolution, and will help to improve intensity forecasts in the future.

However, it remains unclear why the radar reflectivity we see in nature is coupled with the tangential wind, and how the close coupling impacts the TC intensification. To further investigate the question we see in nature but are unable to diagnose from observations due to limited observations, in Chapter 3, a simple modeling framework using a shallow water model to simulate the free atmosphere on top of an asymmetric slab boundary layer to simulate the frictional boundary layer. Two experiments are conducted:

1. One-way interaction: the pressure gradient force in the shallow water layer is enforced to the slab boundary layer, and the slab boundary layer cannot feed back to the free atmosphere.
2. Two-way interaction: same as experiment 1, but the boundary layer is allowed to feed back to the shallow water layer through a mass sink, which is a proxy for diabatic heating parameterized by the boundary layer vertical motion.

The one-way experiment confirms Kuo et al. (2016)'s results in which the SBL layer flow is organized by the shallow water layer and the boundary layer updraft is located at the major axis of the ellipse. This result is also consistent with our findings in Chapter 2 where the strong convection at vertices can depict a polygonal shape.

The two-way experiment further shows when the diabatic heating is continuously replenished by the boundary layer dynamics, the vortex in the free atmosphere can continue to intensify. Our model results also present cycles of appearance of wavenumber 2 and 4 asymmetries under the presence of a reversal sign of mean radial vorticity gradient, which results in oscillations of wavenumber 0 tangential wind intensification. The presence of asymmetries is supported by the PV ring structure with positive radial vorticity inside the eyewall and negative radial vorticity outside. The breakdown of the PV ring evolves into a PV monopole which further leads to a stronger intensification rate. The two-way experiment confirms Chapter 2's findings and is similar to Michael's evolution, which suggest that the presented modeling framework with two-way interactions could be a simple approach to study TC intensification under the presence of evolving asymmetries in the real atmosphere. Future work should conduct sensitivity tests, including different initial condition profiles, heating rate, fluid depth, and other parameter changes to further explore the findings from these two experiments.

In Chapter 4, we improve a multi-Doppler radar technique by implementing the impermeability of the surface and the topographic forcing. We test out the implementation by carrying out a OSSE experiments, and a series of sensitivity tests by using the CR-SIM output, including the constraint range for the boundary conditions, terrain map smoothness, vertical motion retrieval sensitivity to the assumptions of topographic forcing and mass continuity, and the grid spacing and Gaussian recursive filter setting.

Because of the unique configuration of our 3DVAR multi-Doppler technique, the Neumann and Dirichlet boundary condition can be treated as pseudo-observations. A strict pseudo-observation constraint on the Dirichlet boundary condition can lock the retrieved vertical velocity close to the terrain when the observational data points are sparse, whereas the Neumann boundary condition has less impact on the retrievals from our experiments. Terrain map with less steep averaged slope can provide a smooth retrieval with good representation of mesoscale features; whereas a terrain map with too steep slope can produce erroneous results due to unresolved sub-grid scale features. The algorithm assumptions of the mass continuity and topographic forcing are both important. The topographic forcing can lock the orographically-induced vertical motion close to the terrain, so a more accurate representation of terrain-induced vertical motion can be retrieved. The grid spacing and Gaussian recursive filter sensitivity experiment shows that increasing the Gaussian recursive filter can damp the noise and retain the representative features with strong signal, but can lose some detailed structures as a trade-off. Since our results are based on one particular dual-Doppler geometry and a selected small area, numerical errors may be different in other cases. Caution must be taken when selecting parameters in order to retrieve an optimal analysis with a proper representation of the scale of interest. A radar analysis using the new developed technique shows that the airflow of a TC rainband over complex terrain can be retrieved, and the flow structure is consistent with our current physical understanding.

Collectively, this dissertation advances the science by i) improving our understanding of TC inner-core dynamics by using a single Doppler radar retrieval technique with high temporal resolution, ii) using a simple model approach to find that the boundary layer dynamics are one of the key ingredients to support further intensification in an elliptical vortex, and iii) improving the state-of-art multi-Doppler radar retrieval technique to take orographic forcing and surface impermeability into account. The dynamics and processes unfolded by the radar observations can help with TC intensify forecast. The development of multi-Doppler radar retrieval technique can be a salient tool to better understand the mesoscale dynamics, which can further lead to improving QPF forecasts.

References

Bell, M. M., 2017: Extreme precipitation from tropical cyclones. *International Workshop on Monsoons VI.*

Bell, M. M., 2019: nsf-lrose/lrose-blaze: lrose-blaze-20190105. doi: 10.5281/zenodo.2532758.

Bell, M. M., M. Dixon, W.-C. Lee, B. Javornik, J. C. DeHart, and T.-Y. Cha, 2021: nsf-lrose/lrose-elle: lrose-elle stable final release 20210312 (lrose-elle-20210312). *Zenodo,* doi: 10.5281/zenodo.5523312.

Bell, M. M., and W.-C. Lee, 2012: Objective tropical cyclone center tracking using single-Doppler radar. *Journal of Applied Meteorology and Climatology,* **51 (5)**, 878–896, doi: 10.1175/JAMC-D-11-0167.1.

Bell, M. M., W.-C. Lee, C. A. Wolff, and H. Cai, 2013: A Solo-based automated quality control algorithm for airborne tail Doppler radar data. *J. Appl. Meteor. Climatol.,* **52 (11)**, 2509–2528, doi: 10.1175/JAMC-D-12-0283.1.

Bell, M. M., and M. T. Montgomery, 2008: Observed structure, evolution, and potential intensity of Category 5 Hurricane Isabel (2003) from 12 to 14 September. *Monthly Weather Review,* **136 (6)**, 2023–2046, doi: 10.1175/2007MWR1858.1.

Bell, M. M., M. T. Montgomery, and K. A. Emanuel, 2012a: Air–sea enthalpy and momentum exchange at major hurricane wind speeds observed during CBLAST. *Journal of the Atmospheric Sciences,* **69 (11)**, 3197–3222, doi: 10.1175/JAS-D-11-0276.1.

Bell, M. M., M. T. Montgomery, and K. A. Emanuel, 2012b: Air–Sea Enthalpy and Momentum Exchange at Major Hurricane Wind Speeds Observed during CBLAST. *Journal of the Atmospheric Sciences,* doi: 10.1175/JAS-D-11-0276.1.

Beven, J. L., R. Berg, and A. Hagen, 2019: Hurricane Michael (2018). *National Hurricane Center Tropical Cyclone Report*, 86.

Bousquet, O., and M. Chong, 1998: A multiple-Doppler synthesis and continuity adjustment technique (MUSCAT) to recover wind components from Doppler radar measurements. *Journal of Atmospheric and Oceanic Technology*, **15 (2)**, 343–359.

Cha, T.-Y., 2018: Eyewall replacement cycle of Hurricane Matthew (2016) observed by Doppler radars. *M. S. Thesis*, Colorado State University.

Cha, T.-Y., and M. M. Bell, 2021: Comparison of single-doppler and multiple-Doppler wind retrievals in Hurricane Matthew (2016). *Atmospheric Measurement Techniques*, **14 (5)**, 3523–3539, doi: 10.5194/amt-14-3523-2021, URL https://amt.copernicus.org/articles/14/3523/2021/.

Cha, T.-Y., M. M. Bell, W.-C. Lee, and A. J. DesRosiers, 2020: Polygonal eyewall asymmetries during the rapid intensification of hurricane michael (2018). *Geophysical Research Letters*, **47 (15)**, e2020GL087 919, doi: https://doi.org/10.1029/2020GL087919, URL https://agupubs.onlinelibrary.wiley.com/doi/abs/10.1029/2020GL087919, e2020GL087919 10.1029/2020GL087919, https://agupubs.onlinelibrary.wiley.com/doi/pdf/10.1029/2020GL087919.

Chen, Y., and M. K. Yau, 2001: Spiral bands in a simulated hurricane. Part I: Vortex rossby wave verification. *Journal of the Atmospheric Sciences*, **58 (15)**, 2128–2145, doi: 10.1175/1520-0469(2001)058<2128:SBIASH>2.0.CO;2.

Chien, F.-C., and H.-C. Kuo, 2011: On the extreme rainfall of typhoon Morakot (2009). *Journal of Geophysical Research: Atmospheres*, **116 (D5)**.

Chien, F.-C., Y.-C. Liu, and C.-S. Lee, 2008: Prediction of the behavior and strength of typhoons in Taiwan and its vicinity Prediction of the behavior and strength of typhoons in Taiwan and its vicinity, 1980. *Journal of the Meteorological Society of Japan. Ser. II*, **86 (1)**, 17–41.

Chong, c., M, and Coauthors, 2000: Real-time wind synthesis from Doppler radar observations during the Mesoscale Alpine Programme. *Bulletin of the American Meteorological Society*, **81 (12)**, 2953–2962.

Chong, M., and S. Cosma, 2000: A formulation of the continuity equation of MUSCAT for either flat or complex terrain. *Journal of Atmospheric and Oceanic Technology*, **17 (11)**, 1556–1565.

Colle, B. A., 2004: Sensitivity of orographic precipitation to changing ambient conditions and terrain geometries: An idealized modeling perspective. *Journal of the atmospheric sciences*, **61 (5)**, 588–606.

Collis, S., A. Protat, and K.-S. Chung, 2010: The effect of radial velocity gridding artifacts on variationally retrieved vertical velocities. *Journal of Atmospheric and Oceanic Technology*, **27 (7)**, 1239 – 1246, doi: 10.1175/2010JTECHA1402.1, URL https://journals.ametsoc.org/view/journals/atot/27/7/2010jtecha1402_1.xml.

Corbosiero, K. L., J. Molinari, A. R. Aiyyer, and M. L. Black, 2006: The structure and evolution of Hurricane Elena (1985). Part II: Convective asymmetries and evidence for Vortex Rossby Waves. *Monthly Weather Review*, **134 (11)**, 3073–3091, doi: 10.1175/MWR3250.1.

Davies-Jones, R. P., 1979: Dual-Doppler radar coverage area as a function of measurement accuracy and spatial resolution. *Journal of Applied Meteorology (1962-1982)*, 1229–1233.

DeHart, J. C., and R. A. Houze, 2017: Orographic modification of precipitation processes in Hurricane Karl (2010). *Monthly Weather Review*, **145 (10)**, 4171 – 4186, doi: 10.1175/MWR-D-17-0014.1, URL https://journals.ametsoc.org/view/journals/mwre/145/10/mwr-d-17-0014.1.xml.

DeMaria, M., M. Mainelli, L. K. Shay, J. A. Knaff, and J. Kaplan, 2005: Further improvements to the statistical hurricane intensity prediction scheme (SHIPS). *Weather and Forecasting*, **20 (4)**, 531–543, doi: 10.1175/WAF862.1.

Dennis, J. M., A. H. Baker, B. Dobbins, M. M. Bell, J. Sun, Y. Kim, and T.-Y. Cha, 2022: Enabling efficient execution of a variational data assimilation application. *The International Journal of High Performance Computing Applications*, 10943420221119801.

Durran, D. R., and P. N. Blossey, 2012: Implicit–explicit multistep methods for fast-wave–slow-wave problems. *Mon. Wea. Rev.*, **140 (4)**, 1307–1325, doi: 10.1175/MWR-D-11-00088.1.

Eliassen, E., 1951: Slow thermally or frictionally controlled meridional circulation in a circular vortex. *Astrophys. Nor.*, **5**, 19–60.

Foerster, A. M., M. M. Bell, P. A. Harr, and S. C. Jones, 2014: Observations of the eyewall structure of Typhoon Sinlaku (2008) during the transformation stage of extratropical transition. *Monthly Weather Review*, **142 (9)**, 3372 – 3392, doi: 10.1175/MWR-D-13-00313.1.

Friedrich, K., and M. Hagen, 2004: Evaluation of wind vectors measured by a bistatic Doppler radar network. *Journal of Atmospheric and Oceanic Technology*, **21 (12)**, 1840–1854.

Gamache, J. F., F. D. Marks, and F. Roux, 1995: Comparison of three airborne Doppler sampling techniques with airborne in situ wind observations in Hurricane Gustav (1990). *J. Atmos. Oceanic Technol.*, **12 (1)**, 171 – 181, doi: 10.1175/1520-0426(1995)012<0171:COTADS>2.0.CO;2.

Gao, J., M. Xue, K. Brewster, and K. K. Droegemeier, 2004: A three-dimensional variational data analysis method with recursive filter for Doppler radars. *Journal of Atmospheric and oceanic technology*, **21 (3)**, 457–469.

Gao, J., M. Xue, A. Shapiro, and K. K. Droegemeier, 1999: A variational method for the analysis of three-dimensional wind fields from two Doppler radars. *Monthly weather review*, **127 (9)**, 2128–2142.

Georgis, J., F. Roux, and P. Hildebrand, 2000: Observation of precipitating systems over complex orography with meteorological Doppler radars: A feasibility study. *Meteorology and Atmospheric Physics*, **72 (2)**, 185–202.

Guimond, S. R., G. M. Heymsfield, P. D. Reasor, and A. C. Didlake, 2016: The rapid intensification of hurricane karl (2010): New remote sensing observations of convective bursts from the global hawk platform. *J. Atmos. Sci.*, **73 (9)**, 3617 – 3639, doi: 10.1175/JAS-D-16-0026.1, URL https://journals.ametsoc.org/view/journals/atsc/73/9/jas-d-16-0026.1.xml.

Guinn, T. A., and W. H. Schubert, 1993: Hurricane spiral bands. *Journal of the Atmospheric Sciences*, **50 (20)**, 3380–3403, doi: 10.1175/1520-0469(1993)050<3380:HSB>2.0.CO;2.

Hendricks, E. A., B. D. McNoldy, and W. H. Schubert, 2012: Observed inner-core structural variability in Hurricane Dolly (2008). *Monthly Weather Review*, **140 (12)**, 4066–4077, doi: 10.1175/MWR-D-12-00018.1.

Hendricks, E. A., M. S. Peng, B. Fu, and T. Li, 2010: Quantifying environmental control on tropical cyclone intensity change. *Monthly Weather Review*, **138 (8)**, 3243–3271, doi: 10.1175/2010MWR3185.1.

Hendricks, E. A., W. H. Schubert, Y.-H. Chen, H.-C. Kuo, and M. S. Peng, 2014: Hurricane eyewall evolution in a forced shallow-water model. *Journal of the Atmospheric Sciences*, **71 (5)**, 1623–1643, doi: 10.1175/JAS-D-13-0303.1.

Hildebrand, P. H., and C. K. Mueller, 1985: Evaluation of meteorological airborne Doppler radar. Part I: Dual-Doppler analyses of air motions. *J. Atmos. Oceanic Technol.*, **2 (3)**, 362 – 380, doi: 10.1175/1520-0426(1985)002<0362:EOMADR>2.0.CO;2.

Hildebrand, P. H., C. A. Walther, C. L. Frush, J. Testud, and F. Baudin, 1994: The ELDORA/ASTRAIA airborne Doppler weather radar: goals, design, and first field tests. *Proceedings of the IEEE*, **82 (12)**, 1873–1890, doi: 10.1109/5.338076.

Hildebrand, P. H., and Coauthors, 1996: The ELDORA/ASTRAIA airborne Doppler weather radar: High-resolution observations from TOGA COARE. *Bulletin of the American Meteorological Society*, **77 (2)**, 213–232.

Houze, R. A., 2012: Orographic effects on precipitating clouds. *Reviews of Geophysics*, **50 (1)**, doi: https://doi.org/10.1029/2011RG000365, URL https://agupubs.onlinelibrary.wiley.com/doi/abs/10.1029/2011RG000365, https://agupubs.onlinelibrary.wiley.com/doi/pdf/10.1029/2011RG000365.

IPCC, 2021: Climate change 2021: The physical science basis. *The Intergovernmental Panel on Climate Change (IPCC)*, URL https://www.ipcc.ch/assessment-report/ar6/.

Itano, T., and M. Hosoya, 2013: Spectral analyses of the polygonal eye of Typhoon Sinlaku. *Monthly Weather Review*, **141 (3)**, 987–996, doi: 10.1175/MWR-D-12-00122.1.

Jou, B. J.-D., W.-C. Lee, S.-P. Liu, and Y.-C. Kao, 2008: Generalized VTD retrieval of atmospheric vortex kinematic structure. Part I: Formulation and error analysis. *Monthly Weather Review*, **136 (3)**, 995–1012, doi: 10.1175/2007MWR2116.1.

Kaplan, J., and M. DeMaria, 2003: Large-scale characteristics of rapidly intensifying tropical cyclones in the north Atlantic basin. *Weather and Forecasting*, **18 (6)**, 1093–1108, doi: 10.1175/1520-0434(2003)018<1093:LCORIT>2.0.CO;2.

Kepert, J., and Y. Wang, 2001: The dynamics of boundary layer jets within the tropical cyclone core. part ii: Nonlinear enhancement. *Journal of the Atmospheric Sciences*, **58 (17)**, 2485–2501, doi: 10.1175/1520-0469(2001)058<2485:TDOBLJ>2.0.CO;2.

Kepert, J. D., 2017: Time and space scales in the tropical cyclone boundary layer, and the location of the eyewall updraft. *J. Atmos. Sci.*, **74 (10)**, 3305–3323, doi: 10.1175/JAS-D-17-0077.1.

Kirshbaum, D. J., and D. R. Durran, 2005: Observations and modeling of banded orographic convection. *Journal of the atmospheric sciences*, **62 (5)**, 1463–1479.

Koch, S. E., M. desJardins, and P. J. Kocin, 1983: An interactive Barnes objective map analysis scheme for use with satellite and conventional data. *J. Appl. Meteor. Climatol.*, **22 (9)**, 1487 – 1503, doi: 10.1175/1520-0450(1983)022<1487:AIBOMA>2.0.CO;2.

Kossin, J. P., and M. D. Eastin, 2001: Two distinct regimes in the kinematic and thermodynamic structure of the hurricane eye and eyewall. *Journal of the Atmospheric Sciences*, **58 (9)**, 1079–1090, doi: 10.1175/1520-0469(2001)058<1079:TDRITK>2.0.CO;2.

Kossin, J. P., and W. H. Schubert, 2004: Mesovortices in hurricane Isabel. *Bull. Amer. Meteor. Soc.*, **85 (2)**, 151–153.

Kuo, H.-C., W.-Y. Cheng, Y.-T. Yang, E. A. Hendricks, and M. S. Peng, 2016: Deep convection in elliptical and polygonal eyewalls of tropical cyclones. *Journal of Geophysical Research: Atmospheres*, **121 (24)**, doi: 10.1002/2016JD025317.

Kuo, H.-C., R. Williams, and J.-H. Chen, 1999: A possible mechanism for the eye rotation of Typhoon Herb. *Journal of the Atmospheric Sciences*, **56 (11)**, 1659–1673, doi: 10.1175/1520-0469(1999)056<1659:APMFTE>2.0.CO;2.

Lamb, H., 1932: *Hydrodynamics*. Cambridge university press.

Lee, J.-D., and C.-C. Wu, 2018: The role of polygonal eyewalls in rapid intensification of typhoon Megi (2010). *Journal of the Atmospheric Sciences*, **75 (12)**, 4175–4199, doi: 10.1175/JAS-D-18-0100.1.

Lee, W.-C., and M. M. Bell, 2007: Rapid intensification, eyewall contraction, and breakdown of Hurricane Charley (2004) near landfall. *Geophysical Research Letters*, **34 (2)**, doi: 10.1029/2006GL027889.

Lee, W.-C., P. R. Harasti, M. M. Bell, B. J.-D. Jou, and M.-H. Chang, 2006: Doppler velocity signatures of idealized elliptical vortices. *TAO: Terrestrial, Atmospheric and Oceanic Sciences*, **17 (2)**, 429.

Lee, W.-C., B. J.-D. Jou, P.-L. Chang, and S.-M. Deng, 1999: Tropical cyclone kinematic structure retrieved from single-Doppler radar observations. Part I: Interpretation of Doppler velocity patterns and the GBVTD technique. *Monthly Weather Review*, **127 (10)**, 2419–2439, doi: 10.1175/1520-0493(1999)127<2419:TCKSRF>2.0.CO;2.

Lee, W.-C., and F. D. Marks, 2000: Tropical cyclone kinematic structure retrieved from single-Doppler radar observations. Part II: The GBVTD-simplex center finding algorithm. *Monthly Weather Review*, **128 (6)**, 1925–1936, doi: 10.1175/1520-0493(2000)128<1925:TCKSRF>2.0.CO;2.

Lewis, B. M., and H. F. Hawkins, 1982: Polygonal eye walls and rainbands in Hurricanes. *Bulletin of the American Meteorological Society*, **63 (11)**, 1294 – 1300, doi: 10.1175/1520-0477(1982)063<1294:PEWARI>2.0.CO;2, URL https://journals.ametsoc.org/view/journals/bams/63/11/1520-0477_1982_063_1294_pewari_2_0_co_2.xml.

Lin, Y.-L., S. Chiao, T.-A. Wang, M. L. Kaplan, and R. P. Weglarz, 2001: Some common ingredients for heavy orographic rainfall. *Weather and Forecasting*, **16 (6)**, 633 – 660, doi: 10.1175/1520-0434(2001)016<0633:SCIFHO>2.0.CO;2, URL https://journals.ametsoc.org/view/journals/wefo/16/6/1520-0434_2001_016_0633_scifho_2_0_co_2.xml.

Liou, Y.-C., S.-F. Chang, and J. Sun, 2012: An application of the immersed boundary method for recovering the three-dimensional wind fields over complex terrain using multiple-Doppler radar data. *Monthly weather review*, **140 (5)**, 1603–1619.

Liou, Y.-C., and Y.-J. Chang, 2009: A variational multiple-Doppler radar three-dimensional wind synthesis method and its impacts on thermodynamic retrieval. *Monthly weather review*, **137 (11)**, 3992–4010.

Liou, Y.-C., T.-C. Chen Wang, and P.-Y. Huang, 2016: The inland eyewall reintensification of Typhoon Fanapi (2010) documented from an observational perspective using multiple-Doppler radar and surface measurements. *Monthly Weather Review*, **144 (1)**, 241–261.

Lundquist, K. A., F. K. Chow, and J. K. Lundquist, 2010: An immersed boundary method for the weather research and forecasting model. *Monthly Weather Review*, **138 (3)**, 796–817.

Martinez, J., M. M. Bell, R. F. Rogers, and J. D. Doyle, 2019: Axisymmetric potential vorticity evolution of Hurricane Patricia (2015). *Journal of the Atmospheric Sciences*, **76 (7)**, 2043–2063, doi: 10.1175/JAS-D-18-0373.1.

Martinez, J., M. M. Bell, J. L. Vigh, and R. F. Rogers, 2017: Examining tropical cyclone structure and intensification with the FLIGHT+ dataset from 1999 to 2012. *Monthly Weather Review*, **145 (11)**, 4401–4421, doi: 10.1175/MWR-D-17-0011.1.

Matejka, T., and D. L. Bartels, 1998: The accuracy of vertical air velocities from Doppler Radar Data. *Monthly Weather Review*, **126 (1)**, 92 – 117, doi: 10.1175/1520-0493(1998)126<0092:TAOVAV>2.0.CO;2.

Menelaou, K., and M. Yau, 2014: On the role of asymmetric convective bursts to the problem of hurricane intensification: Radiation of Vortex Rossby waves and wave-mean flow interactions. *Journal of the Atmospheric Sciences*, **71 (6)**, 2057–2077, doi: 10.1175/JAS-D-13-0343.1.

Montgomery, M. T., and R. J. Kallenbach, 1997: A theory for vortex rossby-waves and its application to spiral bands and intensity changes in hurricanes. *Quart. J. Roy. Meteor. Soc.*, **123 (538)**, 435–465, doi: https://doi.org/10.1002/qj.49712353810.

Montgomery, M. T., and L. J. Shapiro, 1995: Generalized charney–stern and fjortoft theorems for rapidly rotating vortices. *Journal of the Atmospheric Sciences*, **52 (10)**, 1829–1833, doi: 10.1175/1520-0469(1995)052<1829:GCAFTF>2.0.CO;2.

Moon, Y., and D. S. Nolan, 2015: Spiral rainbands in a numerical simulation of Hurricane Bill (2009). Part II: Propagation of inner rainbands. *Journal of the Atmospheric Sciences*, **72 (1)**, 191–215, doi: 10.1175/JAS-D-14-0056.1.

Muramatsu, T., 1986: The structure of polygonal eye of a typhoon. *Journal of the Meteorological Society of Japan. Ser. II*, **64 (6)**, 913–921, doi: 10.2151/jmsj1965.64.6_913.

Nolan, D. S., and M. T. Montgomery, 2000: The algebraic growth of wavenumber one disturbances in hurricane-like vortices. *Journal of the Atmospheric Sciences*, **57 (21)**, 3514–3538, doi: 10.1175/1520-0469(2000)057<3514:TAGOWO>2.0.CO;2.

North, K. W., M. Oue, P. Kollias, S. E. Giangrande, S. M. Collis, and C. K. Potvin, 2017: Vertical air motion retrievals in deep convective clouds using the arm scanning radar network in oklahoma during mc3e. *Atmospheric Measurement Techniques*, **10 (8)**, 2785–2806, doi: 10.5194/amt-10-2785-2017, URL https://amt.copernicus.org/articles/10/2785/2017/.

Ooyama, K., 1969: Numerical simulation of the life cycle of tropical cyclones. *J. Atmos. Sci.*, **26 (1)**, 3 – 40, doi: 10.1175/1520-0469(1969)026<0003:NSOTLC>2.0.CO;2.

Ooyama, K. V., 1987: Scale-controlled objective analysis. *Mon. Wea. Rev.*, **115 (10)**, 2479 – 2506, doi: 10.1175/1520-0493(1987)115<2479:SCOA>2.0.CO;2.

Ooyama, K. V., 2002a: The cubic-spline transform method: Basic definitions and tests in a 1d single domain. *Mon. Wea. Rev.*, **130 (10)**, 2392–2415, doi: 10.1175/1520-0493(2002)130<2392:TCSTMB>2.0.CO;2.

Ooyama, K. V., 2002b: The cubic-spline transform method: Basic definitions and tests in a 1d single domain. *Mon. Wea. Rev.*, **130 (10)**, 2392 – 2415, doi: 10.1175/1520-0493(2002)130<2392:TCSTMB>2.0.CO;2.

Orszag, S. A., 1970: Transform method for the calculation of vector-coupled sums: Application to the spectral form of the vorticity equation. *J. Atmos. Sci.*, **27 (6)**, 890–895, doi: 10.1175/1520-0469(1970)027<0890:TMFTCO>2.0.CO;2.

Oue, M., P. Kollias, A. Shapiro, A. Tatarevic, and T. Matsui, 2019: Investigation of observational error sources in multi-Doppler-radar three-dimensional variational vertical air motion retrievals. *Atmospheric Measurement Techniques*, **12 (3)**, 1999–2018, doi: 10.5194/amt-12-1999-2019, URL https://amt.copernicus.org/articles/12/1999/2019/.

Oue, M., A. Tatarevic, P. Kollias, D. Wang, K. Yu, and A. M. Vogelmann, 2020: The cloud-resolving model Radar SIMulator (CR-SIM) version 3.3: description and applications of a virtual observatory. *Geoscientific Model Development*, **13 (4)**, 1975–1998, doi: 10.5194/gmd-13-1975-2020, URL https://gmd.copernicus.org/articles/13/1975/2020/.

Potvin, C. K., L. J. Wicker, and A. Shapiro, 2012: Assessing errors in variational Dual-Doppler wind syntheses of supercell thunderstorms observed by storm-scale mobile radars. *Journal of Atmospheric and Oceanic Technology*, **29 (8)**, 1009 – 1025, doi: 10.1175/JTECH-D-11-00177.1, URL https://journals.ametsoc.org/view/journals/atot/29/8/jtech-d-11-00177_1.xml.

Protat, A., and I. Zawadzki, 1999: A variational method for real-time retrieval of three-dimensional wind field from multiple-Doppler bistatic radar network data. *Journal of Atmospheric and Oceanic Technology*, **16 (4)**, 432–449.

Purser, R. J., W.-S. Wu, D. F. Parrish, and N. M. Roberts, 2003: Numerical aspects of the application of recursive filters to variational statistical analysis. Part I: Spatially Homogeneous and Isotropic Gaussian Covariances. *Monthly Weather Review*, **131 (8)**, 1524 – 1535, doi: 10.1175//1520-0493(2003)131<1524:NAOTAO>2.0.CO;2, URL https://journals.ametsoc.org/view/journals/mwre/131/8/_1520-0493_2003_131_1524_naotao_2.0.co_2.xml.

Ray, P. S., J. J. Stephens, and K. W. Johnson, 1979: Multiple-doppler radar network design. *Journal of Applied Meteorology and Climatology*, **18 (5)**, 706 – 710, doi: 10.1175/1520-0450(1979)018<0706:MDRND>2.0.CO;2, URL https://journals.ametsoc.org/view/journals/apme/18/5/1520-0450_1979_018_0706_mdrnd_2_0_co_2.xml.

Ray, P. S., C. L. Ziegler, W. Bumgarner, and R. J. Serafin, 1980: Single- and multiple-Doppler radar observations of tornadic storms. *Monthly Weather Review*, **108 (10)**, 1607–1625.

Reasor, P. D., M. T. Montgomery, F. D. Marks, and J. F. Gamache, 2000: Low-wavenumber structure and evolution of the hurricane inner core observed by airborne dual-Doppler radar. *Monthly Weather Review*, **128 (6)**, 1653–1680, doi: 10.1175/1520-0493(2000)128<1653:LWSAEO>2.0.CO;2.

Rozoff, C. M., J. P. Kossin, W. H. Schubert, and P. J. Mulero, 2009: Internal control of hurricane intensity variability: The dual nature of potential vorticity mixing. *Journal of the Atmospheric Sciences*, **66 (1)**, 133–147, doi: 10.1175/2008JAS2717.1.

Salmon, R., 2014: Analogous formulation of electrodynamics and two-dimensional fluid dynamics. *Journal of Fluid Mechanics*, **761**.

Schubert, W. H., and J. J. Hack, 1982: Inertial stability and tropical cyclone development. *Journal of the Atmospheric Sciences*, **39 (8)**, 1687–1697, doi: 10.1175/1520-0469(1982)039<1687:ISATCD>2.0.CO;2.

Schubert, W. H., M. T. Montgomery, R. K. Taft, T. A. Guinn, S. R. Fulton, J. P. Kossin, and J. P. Edwards, 1999: Polygonal eyewalls, asymmetric eye contraction, and potential vorticity mixing in hurricanes. *Journal of the Atmospheric Sciences*, **56 (9)**, 1197–1223, doi: 10.1175/1520-0469(1999)056<1197:PEAECA>2.0.CO;2.

Schubert, W. H., C. J. Slocum, and R. K. Taft, 2016: Forced, balanced model of tropical cyclone intensification. *Journal of the Meteorological Society of Japan. Ser. II*, **94 (2)**, 119–135, doi: 10.2151/jmsj.2016-007.

Shimada, U., M. Sawada, and H. Yamada, 2018: Doppler radar analysis of the rapid intensification of Typhoon Goni (2015) after Eyewall Replacement. *Journal of the Atmospheric Sciences*, **75 (1)**, 143–162, doi: 10.1175/JAS-D-17-0042.1.

Singh, J., and Coauthors, 2021: Effects of spatial resolution on WRF v3.8.1 simulated meteorology over the central Himalaya. *Geoscientific Model Development*, **14 (3)**, 1427–1443, doi: 10.5194/gmd-14-1427-2021, URL https://gmd.copernicus.org/articles/14/1427/2021/.

Skamarock, K. J. B. D. J. G. D. O. L. Z. B. J. . X. y., W. C., 2021: A description of the advanced research wrf model version 4.3. **(No. NCAR/TN-556+STR)**, doi: 10.5065/1dfh-6p97.

Skamarock, W. C., 2004: Evaluating mesoscale NWP models using kinetic energy spectra. *Monthly Weather Review*, **132 (12)**, 3019 – 3032, doi: 10.1175/MWR2830.1, URL https://journals.ametsoc.org/view/journals/mwre/132/12/mwr2830.1.xml.

Smith, R. A., and M. N. Rosenbluth, 1990: Algebraic instability of hollow electron columns and cylindrical vortices. *Phys. Rev. Lett.*, **64**, 649–652, doi: 10.1103/PhysRevLett.64.649.

Smith, R. B., and I. Barstad, 2004: A linear theory of orographic precipitation. *Journal of the Atmospheric Sciences*, **61 (12)**, 1377 – 1391, doi: 10.1175/1520-0469(2004)061<1377:ALTOOP>2.0.CO;2, URL https://journals.ametsoc.org/view/journals/atsc/61/12/1520-0469_2004_061_1377_altoop_2.0.co_2.xml.

Smith, R. K., M. T. Montgomery, and H. Bui, 2018: Axisymmetric balance dynamics of tropical cyclone intensification and its breakdown revisited. *J. Atmos. Sci.*, **75 (9)**, 3169–3189, doi: 10.1175/JAS-D-17-0179.1.

Spacesystems, N., and U. A. S. Team, 2019: ASTER Global Digital Elevation Model V003 [Data set]. NASA EOSDIS Land Processes DAAC. *Accessed 2022-10-24 from*, doi: https://doi.org/10.5067/ASTER/ASTGTM.003.

Steiner, M., 1991: A new relationship between mean Doppler velocity and differential reflectivity. *Journal of Atmospheric and Oceanic Technology*, **8 (3)**, 430 – 443, doi: 10.1175/1520-0426(1991)008<0430:ANRBMD>2.0.CO;2, URL https://journals.ametsoc.org/view/journals/atot/8/3/1520-0426_1991_008_0430_anrbmd_2_0_co_2.xml.

Terwey, W. D., and M. T. Montgomery, 2002: Wavenumber-2 and wavenumber-m Vortex Rossby Wave instabilities in a generalized three-region model. *Journal of the Atmospheric Sciences*, **59 (16)**, 2421–2427, doi: 10.1175/1520-0469(2002)059<2421:WAWMVR>2.0.CO;2.

Tseng, Y.-H., and J. H. Ferziger, 2003: A ghost-cell immersed boundary method for flow in complex geometry. *Journal of computational physics*, **192 (2)**, 593–623.

Tsujino, S., and H.-C. Kuo, 2020: Potential vorticity mixing and rapid intensification in the numerically simulated Supertyphoon Haiyan (2013). *Journal of the Atmospheric Sciences*, **77 (6)**, 2067 – 2090, doi: 10.1175/JAS-D-19-0219.1, URL https://journals.ametsoc.org/view/journals/atsc/77/6/JAS-D-19-0219.1.xml.

Williams, G. J., R. K. Taft, B. D. McNoldy, and W. H. Schubert, 2013: Shock-like structures in the tropical cyclone boundary layer. *J. Advances in Modeling Earth Systems*, **5 (2)**, 338–353, doi: https://doi.org/10.1002/jame.20028.

Williams Jr., G. J., 2015: The effects of vortex structure and vortex translation on the tropical cyclone boundary layer wind field. *Journal of Advances in Modeling Earth Systems*, **7 (1)**, 188–214, doi: https://doi.org/10.1002/2013MS000299.

Willoughby, H., 1979: Forced secondary circulations in hurricanes. *Journal of Geophysical Research: Oceans*, **84 (C6)**, 3173–3183.

Willoughby, H. E., and M. B. Chelmow, 1982: Objective determination of hurricane tracks from aircraft observations. *Monthly Weather Review*, **110 (9)**, 1298–1305, doi: 10.1175/1520-0493(1982)110<1298:ODOHTF>2.0.CO;2.

Wu, C.-C., 2013: Typhoon Morakot: Key findings from the Journal TAO for improving prediction of extreme rains at landfall. *Bulletin of the American Meteorological Society*, **94 (2)**, 155 – 160, doi: 10.1175/BAMS-D-11-00155.1, URL https://journals.ametsoc.org/view/journals/bams/94/2/bams-d-11-00155.1.xml.

Wu, C.-C., and Y.-H. Kuo, 1999: Typhoons affecting Taiwan: Current understanding and future challenges. *Bulletin of the American Meteorological Society*, **80 (1)**, 67–80.

Wu, C.-C., S.-N. Wu, H.-H. Wei, and S. F. Abarca, 2016: The role of convective heating in tropical cyclone eyewall ring evolution. *Journal of the Atmospheric Sciences*, **73 (1)**, 319–330, doi: 10.1175/JAS-D-15-0085.1.

Xu, W., E. J. Zipser, Y.-L. Chen, C. Liu, Y.-C. Liou, W.-C. Lee, and B. Jong-Dao Jou, 2012: An orography-associated extreme rainfall event during TiMREX: Initiation, storm evolution, and maintenance. *Monthly Weather Review*, **140 (8)**, 2555–2574.

Zipser, E. J., D. J. Cecil, C. Liu, S. W. Nesbitt, and D. P. Yorty, 2006: Where are the most intense thunderstorms on earth? *Bull. Amer. Meteor. Soc.*, **87 (8)**, 1057 – 1072, doi: 10.1175/BAMS-87-8-1057, URL https://journals.ametsoc.org/view/journals/bams/87/8/bams-87-8-1057.xml.

Appendix A: Supporting information for Chapter 2

This supporting information file details the power spectrum analysis, and derivation of azimuthal velocity of each wavenumber from the GVTD analysis. We convert the azimuthal velocity of each wavenumber from the observed frequency of the spectral analysis, and dealias the azimuthal velocity of higher wavenumbers ($m = 4$) due to the radar scanning.

The azimuthal velocity of a linear VRW propagating on a symmetric vorticity discontinuity in a Rankine vortex is:

$$c = V_{max}(1 - \frac{1}{m}) \tag{5.1}$$

where V_{max} is the maximum tangential speed of the mean flow and m is the tangential wavenumber (Lamb 1932; Guinn and Schubert 1993; Kuo et al. 1999). Equation 5.1 shows that higher wavenumbers for the polygonal eye propagate faster, whereas lower wavenumbers propagate slower. Several observational studies using reflectivity as a proxy to VRWs have shown that the azimuthal phase speeds of elliptical eyewall are reasonably consistent with the linearized wave theory (Kuo et al. 1999; Reasor et al. 2000; Corbosiero et al. 2006).

To track the propagation speed of the asymmetries objectively, asymmetric tangential winds and reflectivity from r = RMW - 3 km to r = RMW + 3 km were averaged (such as Fig. 2a), and the averaged data at the 90 degrees (north) with different time window were selected to perform a power spectrum analysis in the frequency domain (Fig. 4). The power spectrum analysis is not sensitive to which azimuth we select. The selected time frames of each wavenumber depends on when the asymmetries are enhanced (Figs. 2e-h), and a continuous period without any missing data. Data of wavenumber-1 is selected from 1130 to 1330 UTC, wavenumber-2 is from 1030 to 1230 UTC, wavenumber-3 is from 1130 to 1330 UTC, and wavenumber-4 is from 13 to 15 UTC. Linear trends in the time series were removed prior to spectral analysis to minimize the impact from spectral leakage to other wave numbers.

Since the radar observation is approximately every five minutes, the azimuthal frequency of high-order wavenumbers can be aliased by the Nyquist frequency of the radar scanning strategy. Figures 4a and b show that the maximum power of wavenumber-4 tangential wind and reflectivity are the closest to the Nyquist frequency, which suggests that the propagation speeds may be aliased by the time interval of radar scanning.

To estimate the "true" propagation speed of wavenumber-4, the azimuthal velocity was unfolded using the Nyquist velocity as the following:

$$V_m = 2\pi f_m \frac{r}{m} \tag{5.2}$$

$$N_m = 2\pi N_{radar} \frac{r}{m} \tag{5.3}$$

$$V_{unfolded} = 2 \times N_m - V_{folded} \tag{5.4}$$

where V_m is the azimuthal velocity of each wavenumber, f_m is the frequency of each wavenumber, r is the radius, N_m is the Nyquist velocity of each wavenumber, N_{radar} is the Nyquist frequency of the radar scanning as described above, and the $V_{unfolded}$ is the true azimuthal speed for the folded wavenumbers. For the radar data used in this study, N_{radar}= 0.5 / T = 0.00167 s^{-1}, where T is the observation period ($\approx$ 5 minutes). Equation 5.2 converts the observed frequency from the spectral analysis to linear velocity. For m = 4 and higher we assume that $V_m = V_{folded}$ as the radar scanning is not fast enough, so the true azimuthal velocities are derived using Eqs. 5.3 and 5.4.